

SINGLE LINE IMAGING METHOD (*SLIM*)
FOR
BIOCHEMICAL APPLICATIONS

DISSERTATION ZUR ERLANGUNG DES GRADES
„DOKTOR DER NATURWISSENSCHAFTEN“
IM PROMOTIONSFACH CHEMIE

AM FACHBEREICH CHEMIE, PHARMAZIE, GEOGRAPHIE UND GEOWISSENSCHAFTEN
DER JOHANNES GUTENBERG-UNIVERSITÄT MAINZ

Sirin Celiksoy

geb. am 03.01.1989 in Wiesbaden

Mainz, 2021

D77 - Dissertation Johannes Gutenberg-Universität Mainz

Dekan: [REDACTED]

1. Berichterstatter: [REDACTED]

2. Berichterstatter: [REDACTED]

Tag der mündlichen Prüfung: 15.07.2021

EIDESSTATTLICHE ERKLÄRUNG

Die vorliegende Arbeit wurde im Zeitraum von Dezember 2014 bis März 2021 in der ‚Nanaobiotechnology Group‘ von Prof. Dr. Carsten Sönnichsen am Institut für Physikalische Chemie der Johannes Gutenberg-Universität Mainz durchgeführt.

Ich versichere, dass ich die vorliegende Arbeit selbstständig und ohne fremde Hilfe verfasst, andere als die angegebenen Quellen nicht benutzt und die den Quellen wörtlich und inhaltlich entnommenen Stellen als solche kenntlich gemacht habe.

Ich versichere, dass ich diese Dissertation bisher weder im In- noch im Ausland (einem Beurteiler oder einer Beurteilerin) schriftlich oder in elektronischer Form als Prüfungsarbeit vorgelegt habe.

(Sirin Celiksoy)

ABSTRACT

Single-particle dark-field microscopy enables the study of molecular interactions, determining binding constants and measuring dynamic processes. However, the number of nanoparticles that can be detected simultaneously combined with high time resolution is still a requirement that limits the method's applicability in the presence of spatiotemporal heterogeneity of the sample under investigation. Therefore, I have developed a new approach to detect the change of the plasmon signal. Instead of employing the spectral information, I switched to use intensity changes at a fixed wavelength. The detection of intensities simplifies the setup, allows for time- and spatial resolution, and extends the range of sensors for dark-field microscopy since the method is independent of resonance phenomena. I have emphasized these advantages by obtaining previously inaccessible information on long time scales, visualizing dynamic processes of molecular interactions with plasmonic nanosensors, and made out-of-resonance dielectric nanoparticles accessible for dark-field microscopy.

I have shown that intensity changes are suited for measuring the adsorption of macromolecules on nanoparticles with the advantage of reducing the overall measurement time up to a factor of two. I also derived new quantities to describe the plasmon sensitivity in such an intensity scheme, which distinguishes between the various contributions: Rayleigh scattering, dielectric contrast, plasmon shift, and frequency-dependent plasmon bulk damping. The sensitivity parameters, intensity bulk sensitivity \mathcal{S}_I and intensity surface sensitivity \mathcal{S}_S , allow characterizing and optimizing the sensor's performance. Furthermore, I found that the basic description of the figure of merit (FOM) underestimates the nanoparticles' performance below the interband transition.

To highlight that plasmonic nanoparticles serve as label-free sensors for visualizing dynamic processes, I investigated the Min system, and I observed that on long time scales (24 hours) the wave pattern, the oscillation period and the synchronization of the wave highly depend on the membrane composition. Such data was previously not accessible because commonly used fluorescence labels are not photostable, thus, limiting the observation time.

In addition, the intensity-based readout allows utilizing out-of-resonance nanoparticles as sensing elements that have not been addressed so far. I showed in a systematic study that out-of-resonance nanoparticles are similar in their performance in comparison to the commonly used gold nanorods. This new class of sensors for dark-field microscopy has the advantage that the nanosensors can be made out of any transparent material, e.g. many oxides, lipid vesicles, or polymer beads, making studies of biological macromolecules, such as the formation of a protein corona, easier to access.

ZUSAMMENFASSUNG

Die Einzelpartikel-Dunkelfeldmikroskopie ermöglicht die Untersuchung molekularer Wechselwirkungen und die Messung dynamischer Prozesse. Allerdings stellt das synchrone Messen einer großen Anzahl von Nanopartikeln bei einer gleichzeitig hohen Zeitauflösung noch eine Herausforderung dar, welche die Anwendbarkeit der Methode für Proben mit räumlich-zeitlicher Heterogenität begrenzt. Daher habe ich in dieser Arbeit einen neuen Ansatz entwickelt, um die Veränderung des Plasmonensignals zu detektieren. Anstatt wie üblich die spektrale Information hierfür als Maß zu verwenden, bin ich dazu übergegangen, Intensitätsänderungen bei einer festen Wellenlänge zu nutzen. Die Detektion von Intensitäten vereinfacht den Messaufbau, ermöglicht eine zeitliche und räumliche Auflösung und erweitert die Bandbreite einsetzbarer Sensoren für die Dunkelfeldmikroskopie, da die Methode unabhängig von Resonanz-Phänomenen ist. Ich habe diese Vorteile hervorgehoben und bisher unzugängliche Informationen auf langen Zeitskalen erhalten, dynamische Prozesse mit plasmonischen Nanopartikeln abgebildet und nicht-resonante dielektrische Nanopartikel als Sensoren für die Dunkelfeldmikroskopie verwendet.

Ich habe gezeigt, dass sich Intensitätsänderungen, die durch die Adsorption von Makromolekülen verursacht werden, zur Messung von Plasmonenverschiebungen eignen mit dem Vorteil, dass die Messdauer um bis zu einem Faktor zwei reduziert werden kann. Ich habe auch neue Parameter zur Beschreibung der Plasmonensensitivität in einem solchen Intensitätsschema hergeleitet, die zwischen den verschiedenen Beiträgen unterscheiden: Rayleigh-Streuung, dielektrischer Kontrast, Plasmonenverschiebung und frequenzabhängige Plasmonendämpfung. Die Sensitivitätsgrößen, Intensitäts-Umgebungs-Empfindlichkeit S_1 und die Intensitäts-Oberflächen-Empfindlichkeit S_2 , erlauben es, die Leistung des Sensors zu charakterisieren und zu optimieren. Außerdem habe ich festgestellt, dass die grundlegende Beschreibung der Gütezahl (*engl.* figure of merit, FOM) die Leistung der Nanopartikel unterhalb des Interbandübergangs als zu gering bewertet.

Um zu verdeutlichen, dass plasmonische Nanopartikel als markierungsfreie Sensoren zur Visualisierung dynamischer Prozesse verwendet werden können, habe ich das Min-System untersucht und gezeigt, dass auf langen Zeitskalen (24 Stunden) das Wellenmuster, die Oszillationsperiode und die Synchronisation der Welle stark von der Membranzusammensetzung abhängen. Solche Daten waren bisher nicht zugänglich, weil die üblicherweise verwendeten Fluoreszenzmarker nicht photostabil sind und daher die Beobachtungszeit einschränken.

Darüber hinaus ermöglicht die intensitätsbasierte Auslesung die Verwendung von nicht-resonanten dielektrischen Nanopartikeln als neue und bisher ungenutzte Sensorelemente. Ich habe in einer systematischen Studie gezeigt, dass die Leistung dieser Nanosensoren mit jener der üblicherweise verwendeten Goldnanostäbchen vergleichbar ist. Diese neue Klasse von Sensoren für die Dunkelfeldmikroskopie hat den Vorteil, dass die Nanosensoren aus jedem transparenten Material hergestellt werden können, z.B. aus vielen Oxiden, Lipidvesikeln oder Polymerkügelchen, wodurch Untersuchungen von biologischen Makromolekülen, wie die Bildung einer Proteinkorona, leichter zugänglich werden.

SCIENTIFIC CONTRIBUTIONS

Parts of this thesis have been published in scientific journals:

Sirin Celiksoy, Weixiang Ye, Karl Wandner, Felix Schlapp, Katharina Kaefer, Rubén Ahijado-Guzmán and Carsten Sönnichsen. Plasmonic Nanosensors for the Label-Free Imaging of Dynamic Protein Patterns. *J. Phys. Chem. Lett.* **2020**, 12, 4554-4558.

Sirin Celiksoy, Weixiang Ye, Rubén Ahijado-Guzmán and Carsten Sönnichsen. Single Non-Resonant Dielectric Nanoparticles as Molecular Sensors. *ASC Sens.* **2021**, Article ASAP (Letter), DOI: 10.1021/acssensors.0c02629.

Sirin Celiksoy, Weixiang Ye, Karl Wandner, Katharina Kaefer and Carsten Sönnichsen. Intensity-Based Single Particle Plasmon Sensing. *Nano Lett.* **2021**, 21, 2053–2058.

Additional scientific publications (not presented in this thesis):

Santosh Kumar Meena, **Sirin Celiksoy**, Philipp Schäfer, Andreas Henkel, Carsten Sönnichsen and Marialore Sulpizi. The role of halide ions in the anisotropic growth of gold nanoparticles: a microscopic, atomistic perspective. *Phys. Chem. Chem. Phys.* **2016**, 18, 13246.

Gustavo Bodelón, Verónica Montes-García, Vanesa López-Puente, Eric H. Hill, Cyrille Hamon, Marta N. Sanz-Ortiz, Sergio Rodal-Cedeira, Celina Costas, **Sirin Celiksoy**, Ignacio Pérez-Juste, Leonardo Scarabelli, Andrea La Porta, Jorge Pérez-Juste, Isabel Pastoriza-Santos and Luis M. Liz-Marzán. Detection and imaging of quorum sensing in *Pseudomonas aeruginosa* biofilm communities by surface-enhanced resonance Raman scattering. *Nat. Mater.* **2016**, 15, 1203–1211.

Benjamin Foerster, Anneli Joplin, Katharina Kaefer, **Sirin Celiksoy**, Stephan Link, and Carsten Sönnichsen. Chemical Interface Damping Depends on Electrons Reaching the Surface. *ACS Nano* **2017**, 11, 2886–2893.

Weixiang Ye, Markus Götz, **Sirin Celiksoy**, Laura Tüting, Christoph Ratzke, Janak Prasad, Julia Ricken, Seraphine V. Wegner, Ruben Ahijado-Guzmán, Thorsten Hugel and Carsten Sönnichsen. Conformational Dynamics of a Single Protein Monitored for 24 h at Video Rate. *Nano Lett.* **2018**, 18, 6633–6637.

Weixiang Ye, **Sirin Celiksoy**, Arpad Jakab, Alena Khmelinskaia, Tamara Heermann, Ana Raso, Seraphine V. Wegner, Germán Rivas Petra Schwille, Rubén Ahijado-Guzmán and Carsten Sönnichsen. Plasmonic Nanosensors Reveal a Height Dependence of MinDE Protein Oscillations on Membrane Features. *J. Am. Chem. Soc.* **2018**, 140, 17901–17906.

Weixiang Ye, Katja Krüger, Ana Sanchez-Iglesias, Isabel García, Xiaoyu Jia, Johannes Sutter, **Sirin Celiksoy**, Benjamin Foerster, Luis M. Liz-Marzan, Rubén Ahijado-Guzmán and Carsten Sönnichsen. CTAB Stabilizes Silver on Gold Nanorods. *Chem. Mater.* **2020**, 32, 1650–1656.

Laureen Moreaud, Janak Prasad, **Sirin Celiksoy**, Sébastien Voillet, Agathe Urvoas, Marie Valerio-Lepiniec, Philippe Minard, Carsten Soennichsen, Erik Dujardin. A single particle sensing platform based on 2D gold nanocrystals coated with designable artificial repeat proteins (Conference Presentation). *Proc. SPIE 11255, Colloidal Nanoparticles for Biomedical Applications XV* **2020**, 112550D.

Katharina Kaefer, Katja Krüger, Felix Schlapp, Hüseyin Uzun, **Sirin Celiksoy**, Bastian Flietel, Axel Heimann, Thies Schroeder, Oliver Kempfski and Carsten Sönnichsen. Smart Tattoos' with Gold Nanosensors for Continuous Long-term Concentration Monitoring in the Body. *Nano Lett.* **2021** (in press).

CONTENT

I INTRODUCTION	1
1 State of the Art	3
Plasmonic Nanoparticles for Biosensing Applications.....	3
Overview.....	5
1.1 Bibliography	6
2 Can We Detect the Plasmon Shift <i>via</i> Intensity Readout?	9
Microscope Setup.....	9
How to determine the background intensity best?.....	12
How to reduce the use of memory space?.....	14
What is the optimal detection wavelength λ_D ?	17
It works.....	21
Comparison to Spectral Readout.....	23
Surface coverage changes measured with the intensity and spectral readout.	25
2.1 Bibliography	27
II PUBLICATIONS	29
3 Theoretical Background: Intensity-Based Single Particle Plasmon Sensing	31
3.1 Introduction	31
3.2 Results and Discussion	32
Measurement Principle.....	32
Previous work.....	32
Mathematical model for the intensity bulk sensitivity S_I	34
Verification of theory for SI with QSA and BEM simulations.	37
Experimental data follows trend predicted by mathematical models.....	38
3.3 Conclusion.....	39
3.4 Author Contributions	40
3.5 Acknowledgement.....	40
3.6 Bibliography	40
4 Application: Plasmonic Nanosensors for the Label-Free Imaging of Dynamic Protein Patterns	43
4.1 Introduction	43
4.2 Results and Discussion	44
Measurement Principle.....	44
Example time traces of Min oscillations.	45
Visualization of measured data.	47
Long observations.	48

4.3	Conclusion.....	49
4.4	Author Contributions	49
4.5	Acknowledgement.....	50
4.6	Bibliography	50
5	Beyond Plasmonics: Single Non-Resonance Dielectric Nanoparticles as Molecular Sensors	53
5.1	Introduction	53
5.2	Results and Discussion	54
	Measurement Principle.....	54
	Response to changes of the close vicinity.....	56
	Signal-to-noise ratio of silica and gold nanoparticles	58
	Sensing with silica and gold nanoparticles.	59
5.3	Conclusion.....	60
5.4	Author Contributions	61
5.5	Acknowledgement.....	61
5.6	Bibliography	61
III	SUMMARY.....	65
6	Summary	67
IV	APPENDIX	71
A	Can We Detect the Plasmon Shift <i>via</i> Intensity Readout?.....	73
A.1	Material and Methods	73
	Materials.	73
	Synthesis and characterization of gold nanorods.	73
	Functionalization of gold nanorods with Polyethylene glycol (PEG).....	75
	Functionalization of gold nanorods with Aptamer.	75
	Flow cell preparation and cleaning.....	75
	General procedure for the dark-field measurements.	76
	QSA simulation to validate the proof-of-concept study.	76
	Signal-to-noise ratio for Min waves utilizing the spectral and intensity readout method.	76
	Data evaluation.....	77
A.2	Supplementary Text	81
	What is the optimal detection wavelength of a single particle?	81
A.3	Bibliography	82
A.4	Copyright	82
B	Intensity-Based Single Particle Plasmon Sensing	85

B.1	Material and Methods	85
	Materials.	85
	Synthesis and characterization of gold nanorods.	85
	Experimental verification of the intensity surface sensitivity \mathcal{S}_I and the intensity bulk sensitivity \mathcal{S}_I	86
	QSA simulation.	87
	BEM simulation.	88
	Molecular sensing under ‘real’ conditions.....	88
B.2	Supplementary Text	89
	Influence of the glass substrate.....	89
	Derivation of plasmon bulk sensitivity \mathcal{S}_λ	90
	Derivation of intensity bulk sensitivity \mathcal{S}_I	91
	Derivation of intensity surface sensitivity \mathcal{S}_I	93
B.3	Additional Figures	94
B.4	Bibliography	95
B.5	Copyright.....	97
C	Plasmonic Nanosensors for the Label-Free Imaging of Dynamic Protein Patterns	99
C.1	Material and Methods.....	99
	Materials.	99
	Synthesis and characterization of gold nanorods.	99
	Protein purification.....	99
	Formation of supported lipid membranes.....	99
	Min system reconstitution.	100
	Microscope setup.	100
	Calculation of particle Temperature.	100
	Data processing.....	100
	Sound representation of the data.	101
	Visualization of the data.	101
C.2	Additional Figures	102
C.3	Additional Material.....	105
C.4	Bibliography.....	105
C.5	Copyright.....	106
D	Single Out-of-Resonant Dielectric Nanoparticles as Molecular Sensors 107	
D.1	Material and Methods	107
	Materials.	107
	Synthesis of gold nanorods.	107
	Characterization of gold nanorods and silica nanoparticles.....	108
	Intensity bulk sensitivity \mathcal{S}_I	109
	Intensity surface sensitivity \mathcal{S}_I	110
	Noise Level.	111
	Local dynamics of the MinDE protein system.	112
	Binding isotherm of the MinD-membrane interaction.....	113

Microscope setup	113
D.2 Supplementary Text	113
Derivation of intensity bulk sensitivity S_1 for dielectric nanoparticles.	113
Derivation of intensity surface sensitivity S_1 for dielectric nanoparticles.	116
D.3 Additional Figures	117
D.4 Bibliography	117
D.5 Copyright	119
ACKNOWLEDGEMENT	121
CURRICULUM VITAE.....	122

LIST OF FIGURES

Figure 1.1:	Plasmonic metal nanoparticles	4
Figure 1.2:	Plasmon sensing principle.	5
Figure 2.1:	Classical methods: ‘refinement’ and ‘spectral imaging’.....	10
Figure 2.2:	Single wavelength imaging method (SLIM)	11
Figure 2.3:	Comparison of background evaluation with and without smoothing	13
Figure 2.4:	Influence of image defocusing.....	14
Figure 2.5:	Measurement modes ‘Full resolution’ and ‘Mask method’	15
Figure 2.6:	Experimental problems.....	16
Figure 2.7:	Experimental investigation of the optimal detection wavelength.....	18
Figure 2.8:	Theoretical investigation of the optimal detection wavelength using the quasi-static approximation (QSA)	20
Figure 2.9:	Proof-of-concept study	22
Figure 2.10:	Intensity readout <i>vs</i> spectral readout - <i>NanoSPR</i>	24
Figure 2.11:	Intensity readout <i>vs</i> spectral readout - Min Waves.....	26
Figure 2.12:	Signal-to-noise (SNR) ratio	27
Figure 3.1:	Plasmon Principle.	33
Figure 3.2:	Mathematical model for the intensity bulk sensitivity S_I	36
Figure 3.3:	Volume dependency of the intensity bulk sensitivity S_I and the intensity surface sensitivity S_S	37
Figure 3.4:	Comparison of experimental data to our mathematical description for the intensity bulk sensitivity S_I and the intensity surface sensitivity S_S	39
Figure 4.1:	Nanoparticle-SPR (nanoSPR) sensing principle.....	45
Figure 4.2:	Time traces of Min coverage fluctuations at different locations.....	46
Figure 4.3:	Spatial reconstruction	47
Figure 4.4:	Long observation time possible.....	48
Figure 5.1:	Measurement principle.....	55
Figure 5.2:	Response to refractive index changes and adsorbate layers	57
Figure 5.3:	Signal-to-Noise Ratio	59
Figure 5.4:	Monitoring Min waves	60
Figure A.1:	TEM images and ensemble extinction spectra of gold nanosensors	74
Figure A.2:	Detrended signal of Min waves	77
Figure A.3:	Data evaluation.....	78
Figure A.4:	Calculation of the particle diameter.	79
Figure A.5:	Bad particles.....	80
Figure A.6:	Data analysis	81
Figure B.1.	Characterization of gold nanorods	86
Figure B.2:	Molecular sensing under ‘real’ conditions	89

Figure B.3:	Plasmon bulk sensitivity S_{λ}	90
Figure B.4:	Comparison of the bulk damping of gold nanoparticles to the overall intensity bulk sensitivity S_I	93
Figure B.5:	Optimal detection wavelength λ_D	94
Figure B.6:	Intensity bulk sensitivity S_I for other nanoparticle materials.....	95
Figure C.1:	Baseline correction and normalization.....	101
Figure C.2:	Oscillation period and signal amplitude of the MinDE coverage fluctuations.....	102
Figure C.3:	Example Min coverage fluctuations for different membrane compositions.....	103
Figure C.4:	Snapshots of the spatial patterns for different membrane compositions....	104
Figure C.5:	Evolution of the Min protein oscillation period for different membrane compositions.....	105
Figure D.1:	TEM images and ensemble extinction spectra of gold nanosensors	108
Figure D.2:	TEM images and ensemble extinction spectra of silica nanoparticles	109
Figure D.3:	Noise of silica and gold nanoparticles.	111
Figure D.4:	Signal amplitude, noise and oscillation period for MinDE protein oscillations.....	112
Figure D.5:	Binding isotherm for the MinD-membrane interaction obtained by using silica nanoparticles as sensors	113
Figure D.6:	Mathematical model for the intensity bulk sensitivity S_I and the intensity surface sensitivity S_s	117
Figure D.7:	Signal-to-Noise Ratio 5 nm adsorption layer.....	117

LIST OF TABLES

Table 2.1:	Overview of time resolution and number of particles for the ‘refinement’ method and the ‘spectral imaging’ method.....	10
Table 2.2:	Mean values, its distribution (<i>STD</i>) and the particle number (N_{part}) for different populations shown in Figure 2.6b.....	17
Table 2.3:	Statistics for biotin-streptavidin interaction	22
Table 2.4:	Experimental (Exp) and theoretical (Theo) values for ζ_{λ} and ζ_I	23
Table 2.5:	Number of measured particles and total measurement time for the first and second experiment (<i>Exp1</i> and <i>Exp2</i>) presented in Figure 2.10 of the spectral readout (<i>Refinement</i>) and the intensity readout (<i>Single Line</i>).....	25
Table 5. 1:	Comparison between experimental data and theoretical predictions (in gray) for ζ_I and ζ_I	58
Table A.1:	Details for gold nanorod synthesis.....	74
Table A.2:	Characterization of gold nanorods.....	75
Table B.1.	Details for gold nanorod synthesis.....	86
Table B.2.	Characterization of gold nanorods.....	86
Table B.3.	Input values to determine the theoretical intensity change presented in Figure B.3.	89
Table B.4:	Summary of definitions and results for plasmon sensitivities.....	94
Table D.1:	Details for gold nanorod synthesis.....	108
Table D.2:	Input values used for theoretical calculations of ζ_I and ζ_I of silica nanoparticles.....	110
Table D.3:	Input values used for theoretical calculations of ζ_I and ζ_I of gold nanoparticles.....	110

PART I

INTRODUCTION

INTRODUCTION

Plasmonic Nanoparticles for Biosensing Applications. During the last decades, plasmonic metal nanoparticles, especially gold and silver nanoparticles, have gained increasing importance for biochemical or biomedical applications.¹⁻² Advantageous are those nanoparticles due to chemical stability combined with easy surface modification and strong light absorption and scattering capabilities leading to remarkably bright colors (Figure 1 left panel).³ These optical properties are based on the ability of metal nanoparticles to generate particle plasmons upon illumination with light.⁴⁻⁵ In this process, the conduction band electrons (electron gas) move in the opposite direction of the incident light's electromagnetic field, whereas the positive atomic core is responsible for generating a restoring force to form a harmonic oscillation at a defined resonance wavelength (Figure 1.1 right panel). This resonance wavelength depends (among other things) on the shape, size, material, and the nanoparticle's close vicinity.⁶⁻⁷ The shift in resonance wavelength in response to changes in the nearby surrounding is the key aspect why plasmonic nanoparticles find widespread application in sensing.⁸⁻¹⁰ Gold is the preferred material for most applications because it combines chemical stability with small internal damping and nanorods the preferred shape due to the higher polarizability than more compact structures combined with relatively simple fabrication.¹¹⁻¹² Overall, plasmonic nanosensors have great advantages: Their optical signal is long-term stable, in contrast to fluorescence labels, which suffer from photobleaching or photo blinking.¹³ Furthermore, the variability of accessible surface modifications allows investigating a broad range of receptor-analyte systems.¹⁴⁻¹⁵

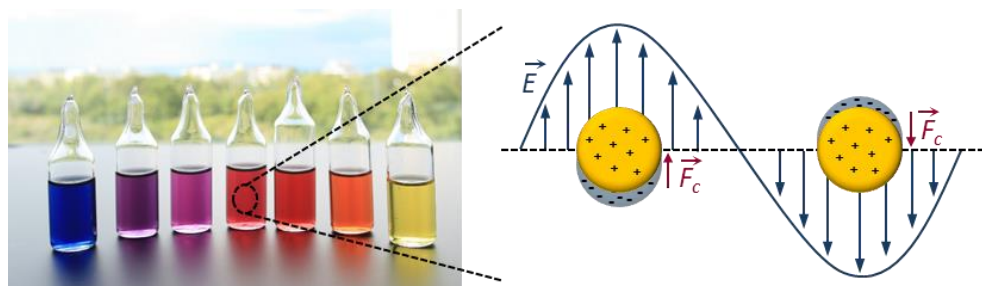


Figure 1.1. Plasmonic metal nanoparticles. Upon illumination with light the conduction band electrons of metal nanoparticles move in the opposite direction of the incident light's electromagnetic field whereas the positively lattice ions generate a restoring force to form a causing a collective oscillation at specific frequency or color, where the absorption and scattering is highest. The image in the left panel was taken by Carsten Sönnichsen and used with permission from the Nanobiotechnology Group.

Besides the fact that plasmonic nanoparticles act as transducers to convert changes in the surrounding refractive index into an optically readable signal, they are used as labels in immunoassays¹⁶⁻¹⁷ or cell imaging¹⁸.

The Nanobiotechnology Group has investigated the use of single plasmonic nanoparticles as sensors for their local environment and developed a multiplexed sensing approach called NanoSPR (Surface Plasmon Resonance) in 2014.¹⁹ The NanoSPR technique allows determining the strength of biomolecular interactions statically or dynamically. The team around Ahijado-Guzmán showed that plasmonic nanoparticles are applicable as a tool to determine the binding affinities between many macromolecular partners simultaneously.¹⁹ They have developed a general functionalization strategy to link the nanoparticle to a given protein using the interaction between nitrilotriacetic acid (NTA) and histidine residues (His-tag). In protein biochemistry, it is common practice to purify proteins via a His-tag resulting in a library of physiologically relevant proteins being already available for investigation. NanoSPR is beneficial because the sensor's dimension reduces the required sample volume. Furthermore, NanoSPR provides build-in statistics without the need to repeat the experiments. In 2012, Ament et al.²⁰ proved that plasmonic nanoparticles are suitable to monitor the dynamic evolution of a single protein binding event (adsorption and desorption) on the millisecond time scale. With their result, they build the basis to use NanoSPR to study fundamental phenomena on the molecular level to understand biological processes and thermodynamics of small systems.

Generally, the readout method relies on measuring the light scattering spectrum of single plasmonic nanoparticles in a dark-field optical microscope.²¹ The Nanobiotechnology Group's available microscopes use two different measurement methods, referred to internally as 'refinement' and 'spectral imaging'.²²⁻²⁴ The 'refinement' method has a fast time resolution in the millisecond range but can only measure one particle at a time, whereas the 'spectral imaging' method measures many nanoparticles in parallel, but with a time resolution only in the second range. Therefore, it was not possible with the existing setups to study time-resolved (below the second region) processes on

many particles simultaneously, for example, to visualize protein patterns, which require a temporally and spatially resolved setup. However, time-resolved single particle studies with high statistics play an important role in protein science if one thinks about variation in the dynamics (nonergodicity) caused by slight differences in the secondary or tertiary structure of the proteins.²⁵⁻²⁶

My work's goal was to develop a microscope setup combining both, high time resolution and high statistics. The approach to achieve this was to move away from the 'classical' plasmon detection scheme. Usually, the signal caused by changes in the particle's close surrounding (Δn) is readout spectroscopically by determining the shift in resonance position ($\Delta\lambda_{\text{res}}$). Something that has not raised much attention in literature so far is, that if the plasmon spectrum shifts the particle's scattering intensity increases (ΔI) as well (Figure 1.2). I explored this feature and developed a new readout method utilizing intensity changes to report on the particle's close vicinity, which I called Single Line Imaging Method (SLIM). The main question during my work was whether it is possible to detect the intensity change occurring with a shift of the particle's scattering spectrum because general noise sources could also influence the particle's scattering intensity. Furthermore, I focused on the following main challenges and questions arising during the development of SLIM:

- ❖ In darkfield microscopy, the measured scattering intensity is composed of the particle's scattering intensity and the entire image's background intensity. Since the background cannot be determined independently from the particle signal, a reliable and robust method was needed raising the question: How to determine the background intensity best?
- ❖ One advantage of SLIM is the possibility to acquire images with high-speed to address time resolved applications. Handling the large amounts of data then becomes a critical point for such high-speed measurements raising the question: How to reduce the use of memory space?
- ❖ An essential aspect for the intensity-based detection is the choice of illumination wavelength. One would like to set the detection wavelength so that the intensity change is largest after analyte binding, which proposes the question: What is the optimal detection wavelength?

I have emphasized the method's advantages, such as simplicity, spatiotemporal resolution and the independence of resonance phenomena in different projects. I showed that plasmonic nanoparticles could visualize protein patterns and obtain previously inaccessible information on long-time scales (24 hours). Furthermore, SLIM allows introducing new sensing elements based on out-of-resonance dielectric material for dark-field microscopy.

Overview. The thesis is structured as follows: In the next chapter (**Chapter 2**), I show how to develop a microscope setup operating in the intensity readout mode and discuss the challenges. Using a model system, I demonstrate the feasibility of the method and elaborate its performance. I address the direct

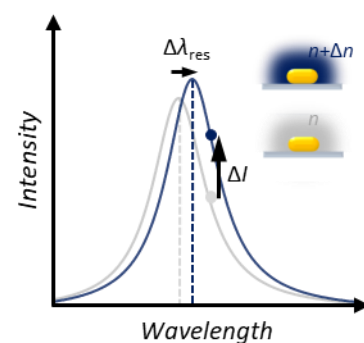


Figure 1.2: Plasmon sensing principle.

comparison to the conventional detection method and the advantages and disadvantages of SLIM.

In **Chapter 3**, I derive mathematical models to describe the plasmon sensitivity in intensity-based detection. I go into detail how the sensitivity is affected by the material and shape of the plasmonic sensor and I validate the mathematical description using both simulations within the quasi-static approximation and experiments.

I highlight the advantages of SLIM in **Chapter 4** and **Chapter 5**. As a model system to show the applicability of plasmonic nanosensors combined with the intensity-based setup to visualize protein patterns, I chose the Min system. It is known that the Min proteins attach to and detach from a lipid membrane periodically and that the membrane composition highly influences this behavior. I exploit the possibility to observe systems for an entire day with the setup to study the temporal dependence of the wave pattern, the oscillation period and the long-range synchronization of the wave. Additionally, I introduce a new class of out-of-resonance dielectric nanosensors to study molecular interactions. I systematically compare their sensing performance with the one of gold nanorods and support the result with theoretical calculations.

The summary in **Chapter 6** is followed by an **Appendix** with supporting information to the main chapters, such as materials and methods and additional data.

1.1 Bibliography

1. Saha, K.; Agasti, S. S.; Kim, C.; Li, X.; Rotello, V. M. Gold Nanoparticles in Chemical and Biological Sensing. *Chem. Rev.* **2012**, *112*, 2739-2779.
2. Sun, J.; Xianyu, Y.; Jiang, X. Point-of-care biochemical assays using gold nanoparticle-implemented microfluidics. *Chem. Soc. Rev.* **2014**, *43*, 6239-6253.
3. Amendola, V.; Pilot, R.; Frasconi, M.; Maragò, O. M.; Iatì, M. A. Surface plasmon resonance in gold nanoparticles: a review. *J. Phys. Cond. Matt.* **2017**, *29*, 203002.
4. Mie, G. Beiträge zur Optik trüber Medien, speziell kolloidaler Metallösungen. *Ann. Phy.* **1908**, *330*, 377-445.
5. Craig F. Bohren, D. R. H. *Absorption and Scattering of Light by Small Particles*. Wiley-VCH Weinheim, **1998**.
6. Mayer, K. M.; Hafner, J. H. Localized Surface Plasmon Resonance Sensors. *Chem. Rev.* **2011**, *111*, 3828-3857.
7. Lee, K.-S.; El-Sayed, M. A. Gold and Silver Nanoparticles in Sensing and Imaging: Sensitivity of Plasmon Response to Size, Shape, and Metal Composition. *J. Phys. Chem. B* **2006**, *110*, 19220-19225.
8. Becker, J. Plasmons as Sensors. PhD, Johannes Gutenberg-Universität Mainz, **2010**.

9. Anker, J. N.; Hall, W. P.; Lyandres, O.; Shah, N. C.; Zhao, J.; Van Duyne, R. P. Biosensing with plasmonic nanosensors. *Nat. Mater.* **2008**, *7*, 442-453.
10. Howes, P. D.; Chandrawati, R.; Stevens, M. M. Colloidal nanoparticles as advanced biological sensors. *Science* **2014**, *346*, 1247390.
11. Sönnichsen, C.; Franzl, T.; Wilk, T.; von Plessen, G.; Feldmann, J.; Wilson, O.; Mulvaney, P. Drastic Reduction of Plasmon Damping in Gold Nanorods. *Phys. Rev. Lett.* **2002**, *88*, 077402.
12. Pérez-Juste, J.; Pastoriza-Santos, I.; Liz-Marzán, L. M.; Mulvaney, P. Gold nanorods: Synthesis, characterization and applications. *Coord. Chem. Rev.* **2005**, *249*, 1870-1901.
13. Ye, W.; Götz, M.; Celiksoy, S.; Tütting, L.; Ratzke, C.; Prasad, J.; Ricken, J.; Wegner, S. V.; Ahijado-Guzmán, R.; Hugel, T.; Sönnichsen, C. Conformational Dynamics of a Single Protein Monitored for 24 h at Video Rate. *Nano Letters* **2018**, *18*, 6633-6637.
14. Sperling, R. A.; Parak, W. J. Surface modification, functionalization and bioconjugation of colloidal inorganic nanoparticles. *Phil. Trans. Roy. Soc.* **2010**, *368*, 1333-1383.
15. Daniel, M.-C.; Astruc, D. Gold Nanoparticles: Assembly, Supramolecular Chemistry, Quantum-Size-Related Properties, and Applications toward Biology, Catalysis, and Nanotechnology. *Chem. Rev.* **2004**, *104*, 293-346.
16. Yguerabide, J.; Yguerabide, E. E. Light-Scattering Submicroscopic Particles as Highly Fluorescent Analogs and Their Use as Tracer Labels in Clinical and Biological Applications: I. Theory. *Anal. Biochem.* **1998**, *262*, 137-156.
17. Cordeiro, M.; Ferreira Carlos, F.; Pedrosa, P.; Lopez, A.; Baptista, P. V. Gold Nanoparticles for Diagnostics: Advances towards Points of Care. *Diagnostics (Basel)* **2016**, *6*, 43.
18. Xu, X.-H. N.; Brownlow, W. J.; Kyriacou, S. V.; Wan, Q.; Viola, J. J. Real-Time Probing of Membrane Transport in Living Microbial Cells Using Single Nanoparticle Optics and Living Cell Imaging. *Biochem.* **2004**, *43*, 10400-10413.
19. Ahijado-Guzmán, R.; Prasad, J.; Rosman, C.; Henkel, A.; Tome, L.; Schneider, D.; Rivas, G.; Sönnichsen, C. Plasmonic Nanosensors for Simultaneous Quantification of Multiple Protein-Protein Binding Affinities. *Nano Lett.* **2014**, *14*, 5528-5532.
20. Ament, I.; Prasad, J.; Henkel, A.; Schmachtel, S.; Sönnichsen, C. Single Unlabeled Protein Detection on Individual Plasmonic Nanoparticles. *Nano Lett.* **2012**, *12*, 1092-1095.
21. Gao, P. F.; Lei, G.; Huang, C. Z., Dark-Field Microscopy: Recent Advances in Accurate Analysis and Emerging Applications. *Anal. Chem.* **2021** (in press).

22. Ye, W. Automated Spectral Imaging Plasmonspectroscopy for Unraveling Molecular Dynamics. PhD Thesis, Johannes Gutenberg-Universität, Mainz, **2018**.
23. Henkel, A. Rod-shaped Plasmonic Sensors. PhD Thesis, Johannes Gutenberg-Universität, Mainz, **2012**.
24. Wulf, V. Dark-field Spectroscopy on Single Plasmonic Gold Nanorods - New Methods. PhD Thesis, Johannes Gutenberg-Universität, Mainz, **2016**.
25. Hu, X.; Hong, L.; Dean Smith, M.; Neusius, T.; Cheng, X.; Smith, Jeremy C. The dynamics of single protein molecules is non-equilibrium and self-similar over thirteen decades in time. *Nat. Phys.* **2016**, *12*, 171-174.
26. Wennmalm, S.; Edman, L.; Rigler, R. Non-ergodic behaviour in conformational transitions of single DNA molecules. *Chem. Phys.* **1999**, *247*, 61-67.

2

CAN WE DETECT THE PLASMON SHIFT *VIA* INTENSITY READOUT?

Single particle dark-field spectroscopy of noble metal nanoparticles exploits the property of plasmonic nanoparticles to be sensitive to their close surrounding. As soon as the particles' immediate vicinity changes, the plasmon resonance shifts.¹⁻² Simultaneously, a change in overall intensity occurs, which has not received as much attention in the literature until now. In this chapter, I want to show how the scattering intensity can be used as a measuring method with certain advantages over the 'classical' spectroscopy readout. I will go into detail about the new measurement setup and the measurement principle. Then, I present a proof-of-concept study using a model system and evaluate the new method's performance. Finally, I will compare the intensity-based readout method and the 'classical' plasmon shift detection method.

Microscope Setup. This section will address the question: what does it take to measure the plasmon shift in intensity mode?

Before answering the question, I will briefly discuss the 'classical' method of measuring single particle plasmon spectra using an optical wide-field microscope with darkfield illumination.³ Generally, the contrast necessary to see the light scattered by individual nanoparticles is achieved with a dark-field condenser. It creates a hollow cone illumination so that the objective collects only the scattered light from the nanoparticle sample being examined. Without this component, the small amount of scattered light would be superimposed onto an extensive bright background, which would make it very difficult to identify the nanoparticles. Figure 2.1 shows a sketch of the light path in the dark-field condenser most commonly used, the 'ultra-condenser'. The existing optical microscopes in the *Nanobiotechnology Group* use two different measurement

methods to resolve the light scattered from single plasmonic nanoparticles spectrally. We refer to them internally as 'refinement' and 'spectral imaging'. In the 'refinement' method, the scattered light of one particle at a time is passed to a spectrograph by using a piezo scanning stage, which moves the particles' image directly in the center of the entrance slit of a spectrometer (Figure 2.1a).

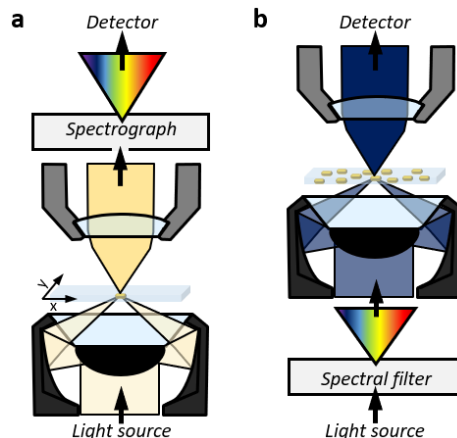


Figure 2.1: Classical methods: 'refinement' and 'spectral imaging'. **a)** Schematic of the 'refinement' method. The illumination light (bright orange) is focused on the nanoparticle sample utilizing a dark-field condenser (black). Only the light scattered by a single nanoparticle (orange) is collected by an objective (grey) and is passed to a spectrograph. A x/y-piezo-stage places the nanoparticle in the image center. **b)** Schematic of the 'spectral imaging' method. The illumination light passes a spectral filter before entering the condenser (black) and being focused on the nanoparticle sample. The scattered light of all nanoparticles (dark blue) in the field of view is collected simultaneously by the objective (grey).

The term 'refinement' comes from the fact that *refining* the position in all three dimensions is very important to get reproducible spectra. In contrast, the 'spectral imaging' method allows for detecting all nanoparticles in the field of view at once. The method's principle is to simultaneously collect all the nanoparticles' scattering intensity at different illumination wavelengths using a spectral filter in the illumination pathway (Figure 2.1b). Both methods have been extensively described in the literature.^{4,6} Here, I want to mention only the time resolution and statistics of both systems. (Table 2.1). The refinement method can measure spectra in the millisecond range, but it can only measure one particle and not several in parallel. In contrast, the spectral imaging method fulfills the statistic requirements, but the time resolution is in the second range.

Table 2.1: Overview of time resolution and number of particles for the 'refinement' method and the 'spectral imaging' method.

Method	Time resolution	Number of particles
Refinement ⁵	up to 0.00008 s	1
Spectral imaging ⁶	0.5 s to 30 s	about 3300

However, for some applications, such as detecting protein dynamics, there is a demand to have a high time resolution and a sufficient number of particles investigated simultaneously. Therefore, my work's goal was to combine the

advantages of both methods. In other words, I wanted to build a microscope setup, which measures the highest possible number of particles with a time resolution in the millisecond range.

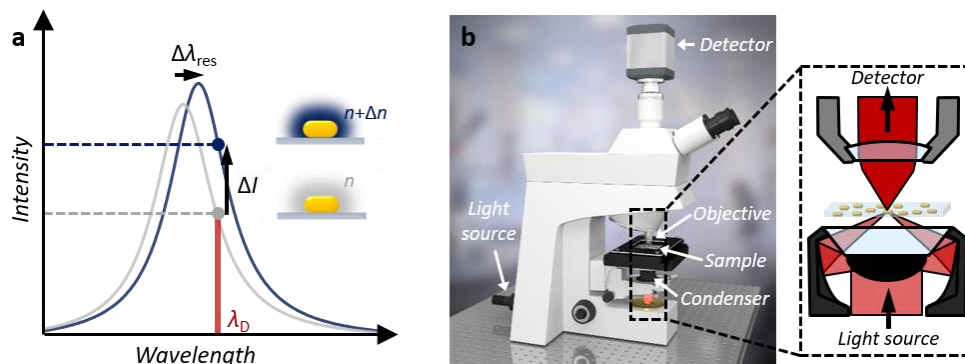


Figure 2.2: Single wavelength imaging method (SLIM). **a)** Single nanoparticle scattering spectra before (gray line) and after (dark blue line) the refractive index around the nanoparticle changes by Δn (insets). The plasmon resonance wavelength shifts by $\Delta\lambda_{res}$, and the intensity increases by ΔI at the detection wavelength λ_D (red bar). **b)** Schematics of an upright darkfield microscope setup. The inset (dashed box) depicts the light pathway of the setup. The illumination light enters a darkfield condenser from beneath. The darkfield condenser directs the light (dark red) to such oblique angles that the objective collects only light scattered by the nanoparticles (gray). The microscope image was prepared by Felix Schlapp and used with his permission.

A solution for this request was to move away from the ‘classical’ detection scheme. Instead of recording the whole particle spectrum and using the nanoparticles’ spectral information ($\Delta\lambda_{res}$) as a measure, I used the scattering intensity change ΔI at one wavelength*, the so-called detection wavelength λ_D (Figure 2.2a). In principle, this shift in detection mode seems trivial: replacing the white light illumination with a narrow band LED and capturing the resulting images directly with a fast camera without using a spectrometer. However, the intensity-based readout method had some challenges that I have addressed during my work and explain more in the next sections.

For all experiments, I used a homebuilt dark-field microscope setup with narrowband illumination operating in the intensity mode. The microscope is constituted of a few parts, listed below and illustrated in Figure 2.2b:

- Light source: Mounted light-emitting diodes (LED) from Thorlabs with wavelengths centered at 660 nm (M660L3) and 735 nm (M735L3)
- Condenser: Zeiss Ultracondenser 1.2/1.4 (0.75-1.0), $a=1.1-1.3$ mm
- Sample: Microfluidic flow cell⁷
- Objective: Plan-Apochromat 40x / 1.3 objective
- Detector: Scientific CMOS camera (Hamamatsu orca flash V4.0)

I used a self-written MATLAB[®]-based software, intern referred to ‘Nanocenter.SL’ for the automated data acquisition and data analysis (cf. Appendix A.1). Karl Wandner has helped with many technical and software aspects and programmed parts of the analysis and control software. The setup configuration

*In this context, one wavelength means a narrowband illumination using a light emitting diode (LED).

*The microscope setup has an additional magnification of 1.25x in the light path.

allows to record the complete field of view ($266\ \mu\text{m} \times 266\ \mu\text{m}$)* with a temporal resolution in the millisecond regime and for a long time (\approx day). The software can operate in two different measurement modes, either the ‘full resolution’ or the ‘mask method’. In the full resolution mode, the acquired images are stored on the hard disc and evaluated afterwards to determine the particle’s scattering intensities. Whereas in the mask method concept the evaluation is done during the measurement to reduce the memory space. Only the particle scattering intensity values are stored on the hard disc. This concept was implemented into the software for measurements of long observation times with a high temporal resolution (cf. section ‘How can we solve the memory space?’)

How to determine the background intensity best? The scattering intensity of plasmonic nanoparticles is not much higher than the diffuse background intensity present in the entire image, even if great care is taken to create ‘dark-field’ illumination. The reason is often out-of-focus scattering centers, for example from impurities in the immersion oil. This diffuse background needs to be subtracted from the image to give an accurate value for the particle’s scattering intensity. The background cannot be measured independently from the particles and it is not uniform throughout the image, which makes a correct background subtraction not trivial. Together with Karl Wandner, we have tested several different methods, two of which I want to describe below: the ‘ring’ method and the ‘image open’ method. The most important issue for long measurements is defocusing – it is important to test the data evaluation method for its robustness with regards to defocusing. It turns out that the ring method suffers from a weak robustness against defocusing. Before we compare both methods, I first want to describe how the ‘image open’ method works and how we optimized it with regards to image noise.

In image processing, the basic operations ‘erosion’ and ‘dilation’ are standardized methods.⁸ The method’s principle is that a structural element (in our case a disk) of a given size (disk diameter) moves along each image pixel. Then, the smallest/largest value within this disk around the pixel is assigned to the pixel for erosion/dilation, respectively. With this method, features with sizes below the disk size are removed. The problem is that image noise leads to an overall reduction in intensity because a pixel, which happens to have (randomly) low intensity, ‘spreads’ this value to all neighboring pixels. We have overcome this problem by smoothing the image before applying the ‘image open’ method. Since the resulting background image showed artificial segment structures, we applied a second smoothing afterwards to improve the results further. We use the Matlab[®] function ‘imopen’ for the erosion and dilation process and ‘imfilter’ for the smoothing.

Figure 2.3a shows the raw image taken at the single line setup without particles in the field of view (left) and evaluated with two approaches to generate the background image, without smoothing (middle) and with smoothing (right). As described above, the overall image intensity is reduced from its original value due to the image noise - the larger the disk size, the stronger this effect (Figure 2.3b, magenta lines). We repeated this process with the same image taken

at lower exposure times, which increases image noise, and the effect increased, as expected. When we apply the smoothing, the overall intensity is stable, as it should be, regardless of the disk size of the ‘image open’ process (Figure 2.3b blue lines). Moreover, there is no significant difference between the three exposure times, indicating that the new procedure with smoothing is far better suited to determine the particles' background intensity.

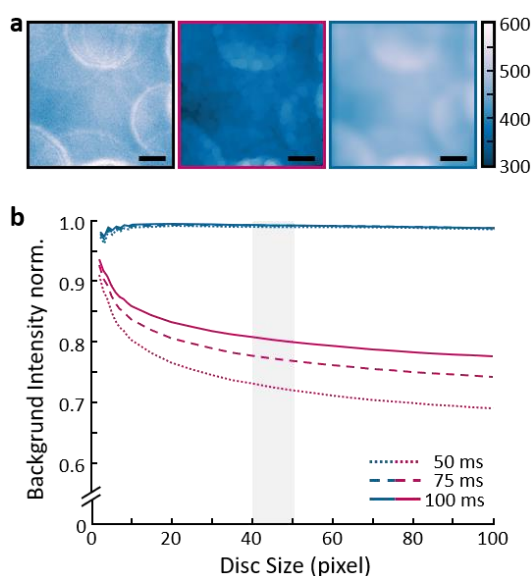


Figure 2.3: Comparison of background evaluation with and without smoothing **a)** Visualization of the raw image (left panel), image background using the pure ‘image open’ process (middle panel) and with smoothing (right panel), recorded at 75 ms exposure time in the single line setup. The big circles are scattering centers (dust) from the upper level of the flow cell. The scalebar corresponds to 50 μm . **b)** The average background intensity as a function of disc size for the pure ‘image open’ process (in magenta) and with smoothing (in blue). All values are normalized to the value of the raw image. The gray area marks the regime we used in a typical experiment.

An alternative method to determine the particle background without image processing by the image open method is to use the average value of a ring of pixels around the particles (black ring) as background (Figure 2.4a). Even though this looks like a fast and easy method at first, we found that it is not stable against defocusing, which is a common problem in long measurements.

An example experiment shows the direct comparison of both methods, the ‘image open’ (Figure 2.4b) or using the ‘ring’ (Figure 2.4a), regarding stability. For this, we first captured a (focused) image of plasmonic nanoparticles on a substrate. In a normal experiment, we would determine the scattering intensities of all particles within the field of view, each corrected for background scattering, as a starting point. Here, we now only collect the background intensity $\Delta I_{B_{\text{rel}}}$ of each particle, calculated using both methods, to test how it evolves over time. We then, still in the focused state, performed a ‘repeat’ measurement (I) without any changes to determine the measurement accuracy or repeatability. Figure 2.4c and 2.4d show the results, which are, as expected, scattered around zero within a standard deviation of less than 1%. Then we defocused the image, determined

the signal (II), and moved back to the focal plane and measured again (III). The results of the background intensity change (II-III) are presented in Figure 2.Xc and 2d. The image-based background determination is more robust against focus changes, as expected, and the mean value stays constant. Whereas, for the ring-based evaluation, an increase of the particles' background intensity occurs (on average) because the defocused particle's scatter into the background pixel areas.

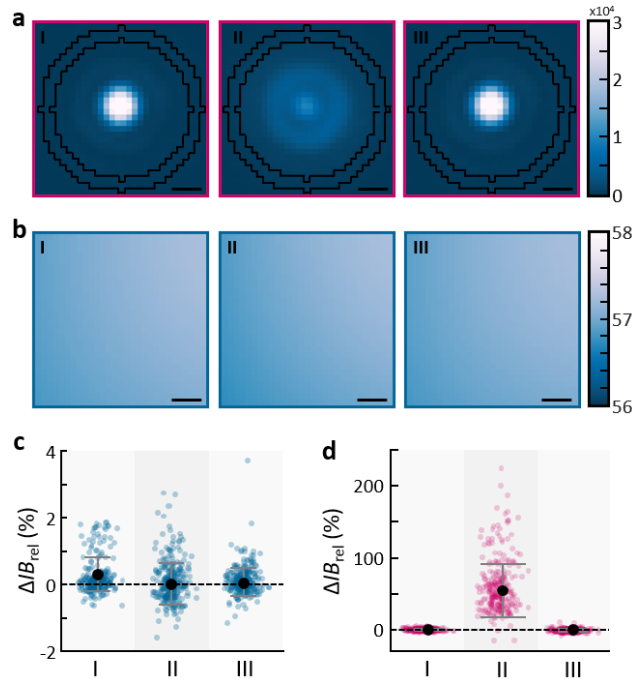


Figure 2.4: Influence of image defocusing. **a)** Image of a single nanoparticle to visualize the background area (black circle) we used to calculate its background intensity in focus (I), out of focus (II) and back in focus plane (III). The scale bar is 5 pixels. **b)** Image background region of a single particle without defocusing the image (I), defocusing the image (II) and going back to the focused situation (III). Scale bar corresponds to 5 pixels. **c)** Relative background intensity shift ΔIB_{rel} for the three focus planes (I-III) using the image background method. The blue dots represent single particle data and the black dots the mean value. The error bars depict the standard deviation. **d)** Relative background intensity shift ΔIB_{rel} for the three focus planes (I-III) utilizing the 'ring' method. The magenta dots represent single particle data and the black dots the mean value. The error bars depict the standard deviation.

In conclusion, we found that the 'image-open' method with smoothing provides a background correction that is robust against pixel noise and focusing problems.

How to reduce the use of memory space? One advantage of the single line imaging method (SLIM) is the speed of the measurement, which allows to study time-dependent processes with high temporal resolution. Handling the large amounts of data then becomes the central challenge for such high-speed measurements. In the most basic case, SLIM involves taking series of images one after the other (see Figure 2.5a), effectively a video, and storing them on the hard disk. The scattering intensities of each particle in the field of view are extracted afterwards. We use a fast camera, which is able to capture full frame

(2048x2048 pixel) images in the millisecond range. The image needs a memory allocation of about 8 MB, which restricts the measurement time for a time resolution of 10 ms to about 45 minutes considering our computers internal memory of 250 GB. Streaming to hard disk would extend this range but turned out to be difficult to implement reliably and the data handling of the resulting terra bytes of data becomes difficult. Each image data contains very little information compared to its size. To give an example: A typical image contains in the order of 1000 nanoparticles. These particles use about 10% of the pixels, the rest is (more or less black) background. Just saving the ‘interesting areas’ would already reduce the memory by 90%. However, at the end, the pixels used by one particle are integrated, resulting in about 1000 numbers. Even if those numbers use a more memory consuming data format than the original image data, the memory use is about a factor 1000 less than the 8MB per image. It is therefore clear that a data reduction would offer a strong advantage. The challenge is to find a data reduction method that is fast enough to keep up with the image generation, at about 100Hz.

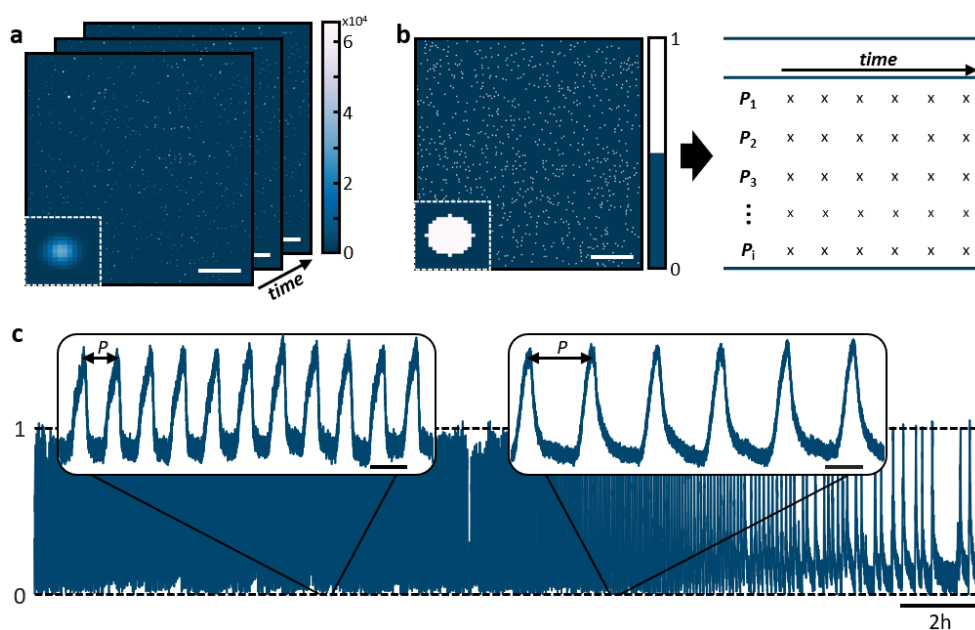


Figure 2.5: Measurement modes ‘Full resolution’ and ‘Mask method’. **a)** Field of view showing the scattering light of hundreds of nanoparticles (scalebar 50 μm). Such images are recorded repeatably and saved on the hard disk. **b)** Field of view showing the template we used for the ‘mask’ method. Only pixels assign to values of 1 are calculated and saved in a matrix (right panel). **c)** The normalized scattering intensity of a single gold nanoparticle as a function of time (blue solid line). We measured the protein coverage fluctuations with 30 ms time resolution for 24 hours. The insets show the oscillation behavior for 20 min intervals at 7.5 hours and 15 hours, respectively. The oscillation period P clearly changes over the observation time.

As a solution to overcome this problem, I have implemented a mode, called ‘mask method’, in the software together with Karl Wandner. The principle behind the mask method is not to save the whole image as usual, but to generate a map with the particle positions at the beginning of the measurement (Figure

2.5b, left panel). The map serves during the further measurement as a template to calculate the particles' scattering intensity directly and thus, to store only the intensity matrix (Figure 2.5b, right panel). I will explain the advantage of the new measurement mode in more detail by means of a calculation example. Figure 2.5c shows a time series of a single particle, which I recorded as part of the project 'Plasmonic nanosensors for the label-free imaging of dynamic protein patterns' presented in Chapter 4. In this project, the aim was to graphically display surface fluctuations using plasmonic nanosensors over several hours and to exploit the capability of single-wavelength detection to be spatial and temporal resolved. The time series was measured with 30 ms time resolution for 24 hours (2.880.000 data points). The full video would use up a storage space of about 22 TB. With the mask method we implemented, the measurement allocates 22 GB for 1000 nanoparticles in the field of view, which the computer was easily able to hold in the memory. Note: The real data contains some additional meta data, for example the particle positions. On the other hand, Matlab[®] compresses the data internally, so that the real storage is around 20-30% lower as calculated. The actual file size for the example mentioned above is therefore 16 GB instead of 22 GB. Without the mask method, we would have been limited in our ability to conduct studies over such a long period of time and encounter previously inaccessible information about protein behavior on such time scales.

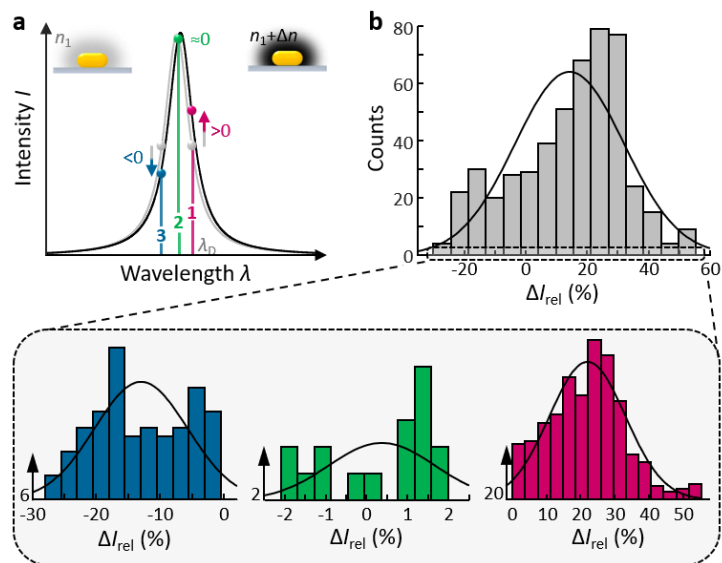


Figure 2.6: Experimental problems. a) Schematic of a single particle scattering spectrum before (grey) and after (black) the ambient refractive index change by Δn . The intensity change is dependent on the illumination wavelengths position λ_D marked with the numbers 1-3. If the detection wavelength is smaller than the resonance wavelength ($\lambda_D < \lambda_{res}$), the intensity shifts to negative values (blue), if it is about to equal, there is no signal change (green), and if the detection wavelength is higher ($\lambda_D > \lambda_{res}$), an intensity increase results. b) Histogram of the relative intensity change ΔI_{rel} measured after the adsorption of streptavidin to biotinylated polyethylene glycol coated gold nanorods. The inset depicts the histograms of the three cases mentioned in panel a) color-coded respectively. The black lines are the best fits of a Gaussian function to the data.

What is the optimal detection wavelength λ_D ? An essential aspect in detecting the plasmon shift by intensity readout is the choice of the detection wavelength λ_D . One would like to choose a detection wavelength with the largest relative change in intensity ΔI_{rel} after analyte binding. If one ignores the overall increase in intensity after analyte binding, then there is a simple relationship between ΔI_{rel} and the intensity profile $I(\lambda)$. If this intensity profile is shifted slightly by $\Delta\lambda_{\text{res}}$, we get $\Delta I_{\text{rel}}/\Delta\lambda = (dI/d\lambda)/I$. In other words, the intensity change is largest if the detection wavelength is at the position of the largest slope, i.e., the maximum of $(dI/d\lambda)/I$. For a single nanoparticle, the derivation of λ_D is therefore straightforward. Assuming a Lorentz-function, which is generally used to describe a nanoparticle spectrum, the optimal detection wavelength is at $\lambda_D = \lambda_{\text{res}} \pm \Gamma/2$, with λ_{res} the particle's resonance wavelength and Γ the particle's line width (see Appendix A.2 for derivation). A complication is that 'real' particle samples have a size distribution ($PDI \approx 1.2$), which leads to a resonance wavelength distribution. Therefore, a common detection wavelength cannot be ideal for each particle and the relationship mentioned above is not applicable for a given distribution.

Table 2.2: Mean values, its distribution (*STD*) and the particle number (N_{Part}) for different populations shown in Figure 2.6b.

	ΔI_{rel} (%)	N_{Part}
Group 1	22.0 ± 11.1	107
Group 2	0.37 ± 1.30	17
Group 3	-13.0 ± 7.2	389
All	14.3 ± 17.7	499

I will highlight the problems occurring in such a 'real' experiment in intensity mode in more detail by showing a typical binding experiment result. In this experiment, I investigated the interaction between the protein streptavidin and the molecule biotin. The adsorption of streptavidin to biotinPEG-coated gold nanorods increases the particles' local refractive index causing a redshift in their resonance wavelengths. Therefore, ideally, the intensity of all nanoparticles should increase. However, since not all nanoparticles have the same resonance wavelength, the intensity change depends on the detection wavelength's exact location relative to the resonance wavelength (see Figure 2.6a). In other words: If the detection wavelength is smaller than the resonance wavelength of the particle ($\lambda_D < \lambda_{\text{res}}$, blue), the intensity decreases ($\Delta I_{\text{rel}} < 0$), if the detection wavelength is equal to the resonance wavelength ($\lambda_D \approx \lambda_{\text{res}}$, green), a minimal change is observed ($\Delta I_{\text{rel}} \approx 0$), and if it is larger ($\lambda_D > \lambda_{\text{res}}$, magenta), the intensity increases ($\Delta I_{\text{rel}} > 0$). Consequently, an intensity distribution consisting of values less than zero and greater than zero is obtained (see Figure 2.6b). The different populations were plotted separately for better visualization (Figure 2.6b, inset), and their mean values were determined (see Table 2.2). Comparing the mean value of the positive shifting particles ($22.0\% \pm 11.1\%$) to the overall mean value of the sample ($14.3\% \pm 17.7\%$), we observe that it is decreased by 35% and the standard deviation increased by 59% due to the proportion of negative shifting

particle intensities (21%). Thus, this lower mean value combined with a higher standard deviation reduces the measurement accuracy.

I questioned whether it is possible to compensate for this disadvantage of real samples by choosing the detection wavelength somewhat more red-shifted by an additional amount depending on the particle resonance wavelength distribution. To address this issue, I conducted an experimental approach and a theoretical approach. The experimental approach uses three different nanoparticle samples with different mean resonance wavelengths resulting in various distances to the detection wavelength ($\Delta\lambda_D$), as shown in Figure 2.7a. I measured the signal strength for the interaction between the protein streptavidin and the molecule biotin utilizing all three particle batches. I determined the relative change in all particles' scattering intensity without changing the particles' environment (*repeat*) and after incubation with streptavidin (*SA*).

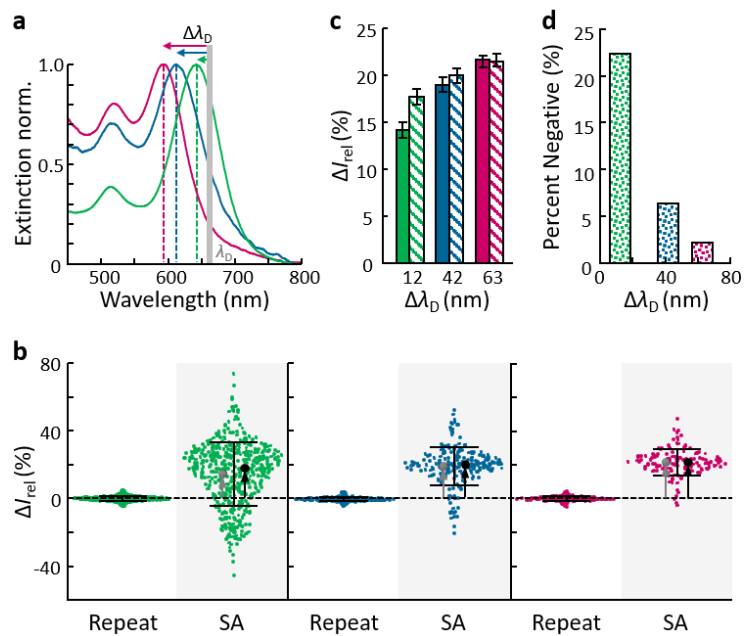


Figure 2.7: Experimental investigation of the optimal detection wavelength. **a)** Normalized ensemble extinction spectra of gold nanosensor coated with biotinylated polyethely glycol (biotin-PEG) batch 1 (magenta line) with a resonance wavelength λ_{res} of 592.5 nm, batch 2 (blue line) with a resonance wavelength λ_{res} of 612.8 nm and batch 3 (green line) with a resonance wavelength λ_{res} of 641.7 nm. The arrows illustrate the distance increase $\Delta\lambda_D$ between detection wavelength λ_D and mean resonance wavelength λ_{res} . **b)** The relative intensity change ΔI_{rel} recorded for hundreds of single gold nanorods (colored dots) without changing the nanoparticles surrounding (*repeat*) and caused by the adsorption of streptavidin (*SA*) for three different nanosensor batches. The single particle data is distributed on the x-axis with respect to its frequency. The gray dots depict the mean and the black dots the median of 505, 220 and 139 nanoparticles for batch 1, 2 and 3, respectively, and the error bars are the standard deviation. **c)** The relative intensity change ΔI_{rel} determined from the data in panel b) for the three nanosensor batches plotted against the distance $\Delta\lambda_D$. The filled bars correspond to the mean value and the patterned bars to the median of all the nanosensors. **d)** Percentage of particles shifting negative after the adsorption of streptavidin as a function of the distance $\Delta\lambda_D$ color coded with respect to panel b).

*I have accounted for the substrate effect and corrected the ensemble resonance wavelength (λ_w) shown in panel a) with the following relation known from literature⁹:
 $\lambda_s = 1.025 \cdot \lambda_w - 10$ nm
 with λ_s being the particle's resonance wavelength on the substrate.

Out of the single particle data, I calculated the mean value (gray dot) and the median (black dot) for each sample (Figure 2.7b). The repeat measurement is a measure for the measurement noise (standard deviation) and is below 1.5% for all three particle samples (Figure 2.7b). The data points for the streptavidin binding (SA) show a larger distribution the smaller the distance $\Delta\lambda_D$ becomes, accompanied by the increasing number of negative shifting particles. Figure 2.7c shows the quantitative numbers for the mean and median signal for the particle samples 1-3. We observe that the mean and median value approaches each other the bigger the distance gets, which is a sign of less asymmetry of the distribution. Since the median is more stable than the mean value concerning the signal asymmetry, we can conclude that it is the more robust and reliable value for the intensity-based readout method. Another critical factor to consider is the number of nanoparticles shifting negative even so the plasmon resonance red-shifts due to the streptavidin binding. As expected, the highest proportion of nanoparticles with intensity changes lower than zero results for sample 1 with 22%, followed by sample 2 with 6% and then sample 3 with only 2% (Figure 2.7d). If we now take the average value and the proportion of negative shifting nanoparticles as a criterion, we can conclude that sample 3 (in magenta) provides the best result and that a greater distance between the detection wavelength and the mean resonance wavelength is favorable.

However, from this experiment, we cannot say precisely, how large this distance should be for a given resonance wavelength distribution within the sample. To find this relationship, one would need to systematically vary both the mean resonance wavelength and its distribution, which would require a large (and unrealistic) amount of nanoparticle samples. Instead, I decided to study this relationship theoretically using simulated spectra. I calculated particle spectra for gold nanorods embedded in water ($n=1.33$) and a material with a slightly higher refractive index ($n=1.331$) by solving Maxwell's equations within the quasi-static approximation (QSA).¹⁰ In order to simulate real 'samples', I repeated this calculation for $N = 10000$ nanorods (ellipsoids) with different sizes. For this, I kept the gold nanorods' diameter ($D=10$ nm) constant but used an individual aspect ratio (AR) for each nanorod that was randomly distributed around a mean value of $AR=2.4$. For each of these artificial 'samples', the distribution (Db) of the aspect ratio increased from 0% to 20% around the mean value in 2.5% steps, resulting in 9 'samples'. The resonance wavelength depends, to a good approximation, linearly on the aspect ratio, which means that the resulting resonance wavelength distributions of the 9 'samples' varied between 0% and 12% around the mean value of 620 nm (Figure 2.8a). I refer to this resonance wavelength distributions as the QI (for quality index with 0% referring to a perfectly monodisperse sample). From the simulated particle spectra, I computed the relative intensity change for all wavelengths. Within one sample, I can thus determine the mean and median signal for every potential detection wavelength $\Delta\lambda_D$. The results are shown in Figure 2.8b and 2.8c for all 9 'samples' as a function of distance ($\Delta\lambda_D$). For a better comparison, I have normalized the data to the maximum signal of the ideal sample (0% distribution). The maximum

and thus the optimal detection wavelength moves to the right for larger particle distributions. In addition, the average signal decreases, which reflects the fact that with more inhomogeneous samples, an increasing number of particles are ‘measured’ at wavelength far from the optimal detection wavelength. As expected, for very inhomogeneous samples, i.e., broad distribution of the resonance wavelength, the choice of illumination wavelength becomes increasingly arbitrary.

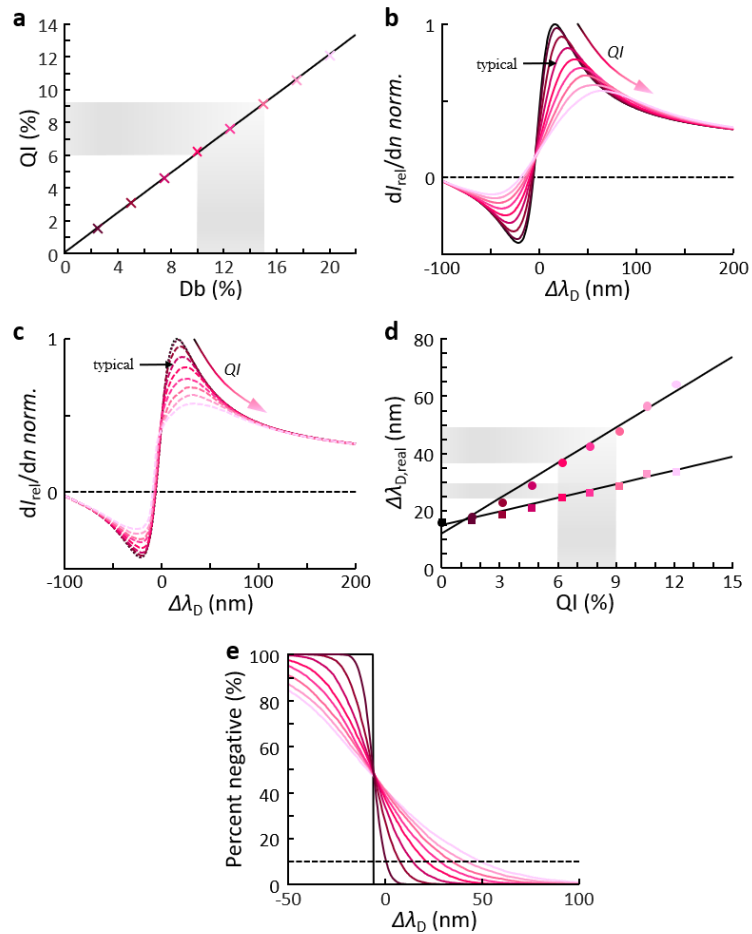


Figure 2.8: Theoretical investigation of the optimal detection wavelength using the quasi-static approximation (QSA). **a**) Dependency between the distribution of the aspect ratio (Db) and the distribution in resonance wavelength, I used as a quality index (QI). **b**) Mean intensity change (dI_{rel}/dn) as a function of distance ($\Delta\lambda_D$) for increasing sample inhomogeneity (QI , colored arrow). Normalized to the optimal signal of the ideal case ($QI = 0\%$). **c**) Median intensity change (dI_{rel}/dn) as a function of distance ($\Delta\lambda_D$) for increasing sample inhomogeneity (QI , colored arrow). Normalized to the optimal signal of the ideal case ($QI = 0\%$). **d**) From the data in panel b) and panel c) the optimal distance for each distribution (dots for the mean and squares for the median color-coded respectively) is determined and plotted against the quality index. The black line shows the best fit of a linear function. The grey area illustrates the region experimental data fits in. The inset depicts the dependency between the distribution of the aspect ratio (Db) and the distribution in resonance wavelength, I used as a quality index (QI). **e**) Percentage of particles shifting negative after the particles surrounding changed by Δn as a function of the distance $\Delta\lambda_D$ color coded with respect to sample inhomogeneity.

If we choose the detection wavelength $\lambda_D = \lambda_{res} + \Delta\lambda_{D,real}$ at the maximum of the mean signal or the median signal, we find a linear relationship to the sample quality QI (Figure 2.8d) as follows: $\Delta\lambda_{D,real} = 411 \frac{\text{nm}}{\%} \cdot QI + 12 \text{ nm}$ and $\Delta\lambda_{D,real} = 160 \frac{\text{nm}}{\%} \cdot QI + 15 \text{ nm}$ for both values, respectively. Again, we can observe that the median is more robust against the asymmetry of the signal distribution causing optimal detection wavelengths for real sample distributions closer to the ideal case. Those relationships help to identify the optimal detection wavelength for given particle distributions. In circumstances, where it is difficult to identify individual particles, such as nanoparticle arrays, one has to choose the detection in accordance and use the equation with the mean value. The gray area marks a typical particle distribution range for nanorod samples prepared in our group.¹¹

Note: In the above study, we optimized the relative intensity change – without considering signal-to-noise ratio (S/N). In other words, we assume an intensity independent noise. In reality, the scattering intensity of single nanoparticles is very small, which means that (especially for fast measurements), the absolute intensity may become an important aspect to consider as well. In many cases, noise (σ) of the relative intensity decreases with the scattering intensity I as: $\sigma \sim I^{-1/2}$. The absolute particle intensity decreases with distance ($\Delta\lambda_D$), which would make a detection wavelength closer to the resonance wavelength more favorable. In such cases, the exact balance between this noise effect and the above-mentioned particle inhomogeneity effect relies on many specific setup parameters.

It works. To demonstrate that the intensity-based method is suitable for analyte detection, I chose the interaction between the protein streptavidin and the molecule biotin as a test system. I set up the experiment to examine responsive and non-responsive gold nanorods simultaneously within the same experiment. For such an experiment, two batches of particles, ‘responsive’ and ‘reference’, were prepared from the same stock of gold nanorods. The responsive particles were reacted (‘functionalized’) with polyethylene glycol (PEG) molecules that contained the ‘biotin’ motive on one end that is known to bind strongly to the protein streptavidin. The reference particles received a coating of PEG without the biotin motive. Both types of particles were deposited on the bottom of a microscope flow cell. The trick is to record the positions of all the particles deposited from the first batch before flowing the second batch in. In this way, one knows exactly which group of particle belongs to which batch, even though both are randomly deposited on the same substrate. With this approach, I wanted to ensure that the signal change to the responsive particles was caused by a specific interaction and not by interfering sources, e.g., mechanical instabilities of the setup as mentioned above or non-specific interaction of the proteins with the nanoparticles. The reference group serves as an indicator of this and should show no signal change after the addition of the analyte. I determined the change in scattering intensity of all particles in the field of view without changing the particles surrounding (*repeat*) and after the incubation with

streptavidin (*SA*). The repeat measurement gives an indication of the repeatability of the and noise in the measurement. We see some changes for the data of individual particles, up to 10% changes in relative intensity, but these changes are random, and the mean value (black bars) remains at 0%. This distribution of individual particles but constant mean value validates the need for statistics in single particle sensing. After the addition of streptavidin, the intensity of the responsive gold nanorods increases by an average of 20%, whereas the intensity of the non-responsive reference nanoparticles shows no signal change on average (Figure 3a, right panel). Even though the reference particles show, on average, no signal change, the distribution of signals within this group increases substantially from the repeat measurement, which indicates that the process of flowing an analyte through the flow cell causes some random changes, which manifest as an increased noise level. I have speculated that these changes might be due to changes in orientation of the particles induced by the flow, which could, combined with a slight polarization anisotropy of my setup, lead to the observed effect. Up to know, this is, however, an unproven hypothesis. Another aspect could be the unspecific interaction with streptavidin. In fact, there seems to be a random effect caused by flowing in liquids into the flow cell, which is much larger than the measurement noise from the setup itself (which was measured in the ‘repeat’ measurement).

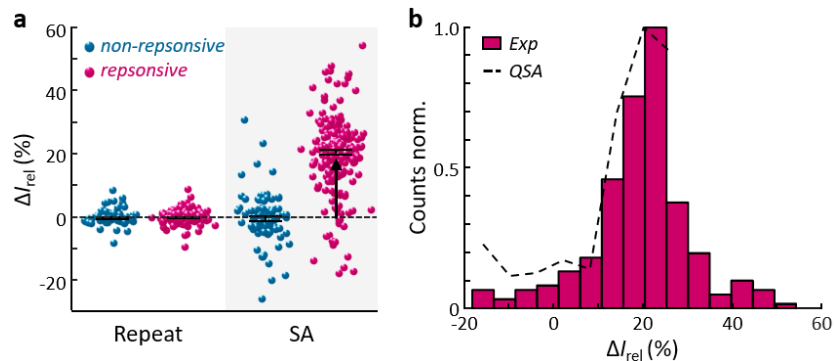


Figure 2.9: Proof-of-concept study. **a)** Relative intensity change ΔI_{rel} for responsive (magenta dots) and non-responsive (blue dots) gold nanorods without changing the surrounding (*repeat*) or caused by the adsorption of the protein streptavidin (*SA*, gray area). **b)** Histogram showing the experimentally determined distribution of the relative intensity change ΔI_{rel} for the streptavidin binding of responsive nanosensors shown in panel a). The dashed line depicts the signal change expected for a nanoparticle distribution calculated within the quasi-static approximation (QSA).

Table 2.3. Statistics for biotin-streptavidin interaction.

	Median	Error
<i>Exp</i>	20.5 %	0.8* %
<i>QSA</i>	20.1 %	3.0# %

*Standard error of the mean

#The error is estimated as 15% from the uncertainties of the input values.

The responsive particles show a mean shift of about 20%, which is clearly significant. To test if the observed intensity increase is in the theoretically expected range, I compared the experiment results with electrostatic calculations. For this purpose, I simulated scattering spectra of individual nanoparticles within the quasi-static approximation (QSA) and determined the intensity change at the detection wavelength for the particle distribution (see Appendix A.1). The simulated distribution shows on average an intensity increase of 20.2 % which agrees perfectly with the experimental data (Figure 2.9b)

and Table 2.3). Deviations between experimental data and simulated data at the borders might be caused by the fact that too bright (saturated pixel) or too weak (lower than three times the mean background intensity) particle intensities are excluded during the analysis of the data. In addition, the large distribution of results within the reference group indicates an increased experimental noise (see above for a possible explanation), which would be expected to be on top of the theoretically expected distribution caused by the particles resonance wavelength distribution.

Considering that the non-responsive nanoparticles show no mean signal change, whereas the responsive nanoparticles increase on average as predicted by electrostatic calculations, I can conclude that the intensity-based sensing method is applicable for detecting the plasmon shifts induced by analyte binding. Furthermore, this experiment shows that for an accurate determination of analyte binding, statistical data from several particles is necessary. Here, a distribution around the mean of 11.6% was observed. If a given analyte would be expected to induce a signal of 20.5%, a reliable detection (2σ) would require that $20.5\% > 1.6\% (2 \cdot (11.6\% / \sqrt{220}))$. For example, we could detect signals as small as 0.2% with $N=10000$ nanoparticles. A significant increase of the accuracy of this method would require a better understanding of the source of the noise.

Comparison to Spectral Readout. Finally, I would like to discuss the advantages and disadvantages of the two readout methods, intensity and spectra, by comparing their performance in three concrete examples: First, I determined the *surface sensitivities*, second, I performed a typical *NanoSPR* experiment to obtain binding constants and third measured the response to *surface coverage changes* over time.

To determine the surface sensitivity* using the two measurement modes, I utilized the well-known layer-by-layer (*LbL*) assembly method.¹²⁻¹⁴ First, I deposited nanoparticles on the glass bottom of a microfluidic flow cell and then recorded the signal change, either spectral shift $\Delta\lambda$ or intensity shift $\Delta I_{rel}^{\#}$, towards increasing layers. Figure 2.10a shows the result as a function of the layer thickness change Δl . For small layer changes, both signals show a linear behavior as expected. From the linear regression to the experimental data, a resonance wavelength surface sensitivity \mathcal{S}_λ of 1.8 ± 0.1 nm/nm and an intensity surface sensitivity \mathcal{S}_I of 9.9 ± 0.5 %/nm, result. Furthermore, I compared the experimental values to theoretical calculations using the mathematical models described in Chapter 3. Experimental values and theoretical calculations agree reasonably well (see Table 2.4).

*A parameter to describe the performance of single nanosensors to changes at the surface.

^{\#}The intensity change ΔI has been normalized to the initial intensity I_0 .

Table 2.4. Experimental (*Exp*) and theoretical (*Theo*) values for \mathcal{S}_λ and \mathcal{S}_I .

	\mathcal{S}_λ (nm/nm)	\mathcal{S}_I (%/nm)
<i>Exp</i>	$3.0 \pm 0.2^*$	$16.5 \pm 0.8^*$
<i>Theo</i>	$2.5 \pm 0.4^\#$	$22.8 \pm 3.4^\#$

The experimental values were adjusted for the substrate effect of 60 %.

*Standard deviation of the fit

^{\#}The error is estimated as 15% from the uncertainties of the input values.

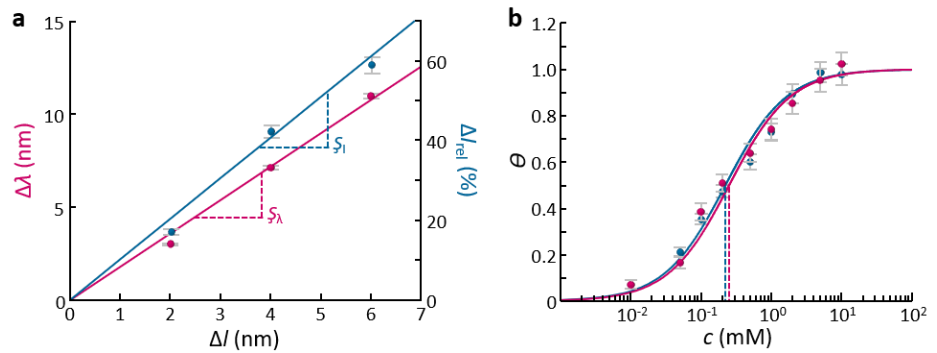


Figure 2.10: Intensity readout vs spectral readout - NanoSPR. **a)** The average signal of 113 nanorods measured in the spectral readout mode (in magenta) and 306 nanorods measured in the intensity mode (in blue) towards the adsorption of polyelectrolyte bilayers Δl . The colored dots depict the median and the error bars are the standard error of the mean. **b)** Binding of the interaction between the analyte kanamycin and the aptamer-coated nanorods. The magenta dots depict the average coverage Θ of 71 nanorods for different kanamycin concentration c recorded with the spectral readout and the blue dots the average of 631 nanorods measured using the intensity readout method. The error bars are the standard error of the mean. The dissociation constants K_D of $0.25 \text{ mM} \pm 0.05 \text{ mM}$ and $0.22 \text{ mM} \pm 0.05 \text{ mM}$ (dashed lines) are determined from the best fit of a Langmuir equation (magenta and blue lines) to the experimental data.

An essential difference between recording spectral changes or intensity changes is the overall measurement time t_m needed for one experiment. The overall time for the experiment in the intensity readout mode is the exposure time t_{exp} and the system's incubation time t_i , i.e., the time between measurements where the layers form. In contrast, the overall measurement time utilizing the spectral readout requires to account for the waiting time t_w , needed to move the particle under the slit entrance because only one nanoparticle at a time is measurable. Table 2.5 shows a summary of the values. With the intensity-based detection method, I could measure six times more nanoparticles and still have a time saving of $\approx 100\%$ for this experiment. Unfortunately, the higher number of nanoparticles does not increase the measurement accuracy (standard error of the mean). The reason is the higher signal distribution in the intensity sensing scheme due to the nanoparticles' size distribution and thus not having the optimal detection wavelength for all nanosensors in the field of view. However, both experiments result in approximately the same final relative accuracy in the surface sensitivity parameter. In both cases, the error is about 18 to 20 times smaller than the corresponding surface sensitivity, in other words, the relative error is about 5%.

All in all, I can conclude that both modes are equally suitable to determine surface sensitivities with a slight advantage of the intensity mode due to the time saving aspect. The time saving aspect becomes larger if more measurements are performed with smaller waiting time between the measurements. In the final example below of a continuous measurement, this difference becomes very large.

Table 2.5: Number of measured particles and total measurement time for the first and second experiment (*Exp1* and *Exp2*) presented in Figure 2.10 of the spectral readout (*Refinement*) and the intensity readout (*Single Line*).

Method		N_{Part}	N_{Runs}	t_{exp} (ms)	t_i (s)	t_w (s)	t_m (min)
Refinement	<i>Exp 1</i>	113	5	300 [*]	300	203 [#]	≈ 50
	<i>Exp 2</i>	71	10	250 [§]	900	91 [#]	≈ 171
Single Line	<i>Exp 1</i>	631	5	50	300	-	≈ 25
	<i>Exp 2</i>	306	10	250	900	-	≈ 150

^{*}3 Acquisitions; [§]2 Acquisitions; [#]Waiting time of 1 run for all nanoparticles

The binding affinity, also known as the equilibrium dissociation constant K_D , is a parameter to describe the strength of bimolecular interactions (analyte-ligand interaction). In 2014 Ahijado-Guzmán et al. showed that plasmonic gold nanoparticles are suitable to determine K_D values.¹⁵ Since I have already shown that the intensity readout allows to detect the adsorbates' binding, I wanted to explore whether a concentration-dependent evaluation is possible. As a model system, I decided to investigate the interaction of the analyte kanamycin to aptamer-coated gold nanorods. This interaction system has been established in the Nanobiotechnology group and characterized in detail by Katharina Kaefer as a part of her doctoral thesis.¹⁶ To obtain the binding constant, the nanosensors were exposed to solutions with increasing kanamycin concentration (0.02 mM to 10 mM), and the signal ($\Delta\lambda$ or ΔI_{rel}) was recorded for each concentration after reaching the equilibrium (≈ 10 min). For a better comparison, I normalized both measurements to the maximum coverage. Figure 2.10b shows the average particle coverage (θ) as a function of kanamycin concentration (c). Both binding isotherms (magenta and blue lines) show the same trend. From the best fit of a Langmuir equation* to the experimental data, I determined K_D values of $0.25 \text{ mM} \pm 0.05 \text{ mM}$ and $0.22 \text{ mM} \pm 0.05 \text{ mM}$ for the spectral and intensity-based detection, respectively, which are in good agreement with the literature value of 0.4 mM .¹⁶ Again, I have compared the total measurement time needed for this type of experiment. The calculated results are presented in Table 2.5. I could measure four times more nanoparticles and have a time saving of $\approx 15\%$.

In summary, the intensity-based detection is equally well suited to determine quantitative parameters with the advantage of being faster and measuring more particles at the same time with a simpler setup. The time saving is partly offset by a larger noise which requires more statistics for the same accuracy of the mean.

Surface coverage changes measured with the intensity and spectral readout. In 2016, Lambertz et al. showed that plasmonic nanosensors are suitable to detect reversible dynamic processes with high time resolution.¹⁷ They investigated the pattern-forming MinDE protein system from *Escherichia coli*. Figure 2.11a shows an example time trace of those surface coverage fluctuations (blue dots) measured with a time resolution of 250 ms. Through their work, they were able to obtain previously inaccessible information. They had the hypothesis that the Min oscillation takes place on a static protein layer. However, the

*Langmuir equation: $\theta(c) = \frac{c}{c+K_D}$
with the coverage θ , the analyte concentration c and the dissociation constant K_D , which is the ligand concentration occupying half coverage.

microscope setup at that time was limited technically to study this aspect further. Weixiang Ye improved the microscope setup, allowing us to investigate over a thousand nanosensors simultaneously with a temporal resolution of 1.5 s. In 2018 he had proven together with co-workers (including myself) the hypothesis of Lambertz et al. and found that the spatial location of the dynamic attachment process depends on the membrane composition. The advantage of the new setup to measure more nanoparticles at once came at the expense of time resolution, limiting the applicability for faster dynamic processes.

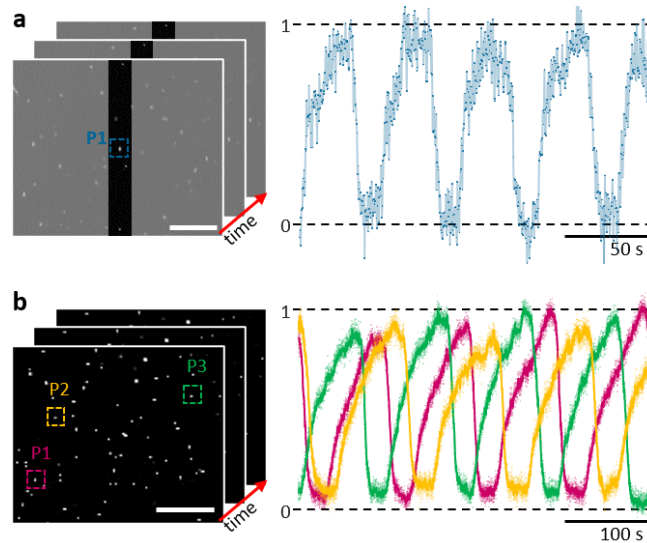


Figure 2.11: Intensity readout vs spectral readout - Min Waves. **a)** A small part of the field of view showing a nanoparticle placed in the center of the slit (scale bar 20 μm) and recorded over time. The right panel shows the normalized signal of one nanoparticle for 200 s with a time resolution of 250 ms (blue dots). The transparent blue line is a guide to the eye. The data of the right panel has been recorded by Christina Lambertz and adapted with permission from reference 17 Figure 2b. **b)** A small part of the field of view showing many single nanoparticles (scalebar 20 μm) recorded repeatably over time. The right panel depicts the normalized signal of three different nanoparticles for a time span of 400 s. The dots represent the original data measured with a time resolution of 30 ms and the lines are the trend averaged over 8 points to mimic the time resolution of the spectral readout method. The figure is adapted with permission (see Chapter 4).

The intensity-based detection method combines both benefits (statistics and time resolution in the millisecond regime). Therefore, I revisited the system to obtain spatially and temporally resolved information and observe the Min waves over one day with videos (see Chapter 4). Figure 2.11b shows a small section of such a time series measured with a time resolution of 30 ms. The direct comparison of both time series shows that the intensity-based measurement method shows less noise, especially when 8 data points are averaged to mimic the time resolution in panel a) of 250 ms. To investigate this aspect quantitatively, I determined the signal-to-noise (*SNR*) ratio of those time trajectories (Figure 2.12). As the signal, I chose the Min waves oscillation amplitude, and as the noise, I used the short-term noise by filtering the oscillation out with a frequency filter of 0.1 Hz and determining the standard

deviation of the remaining signal (cf. Appendix A.1). The results clearly show an advantage of the intensity-based readout over the spectral readout. The SNR is at least three times higher. Comparing again the overall measurement time of both methods, intensity and spectral, the intensity readout method is 487 times better because within one experiment we collect the information of many particles in parallel. To achieve the same with the spectral detection one has to measure 487 nanoparticles after each other resulting in a total measurement time of about 27 hours.

In conclusion, measuring the intensity change and not the spectral change allows investigating a higher number of particles in parallel with a time resolution in the millisecond regime.

2.1 Bibliography

1. Anker, J. N.; Hall, W. P.; Lyandres, O.; Shah, N. C.; Zhao, J.; Van Duyne, R. P. Biosensing with Plasmonic Nanosensors. *Nature Materials* **2008**, *7* (6), 442-453.
2. Mayer, K. M.; Hafner, J. H. Localized Surface Plasmon Resonance Sensors. *Chemical Reviews* **2011**, *111*, 3828-3857.
3. Gao, P. F.; Lei, G.; Huang, C. Z. Dark-Field Microscopy: Recent Advances in Accurate Analysis and Emerging Applications. *Analytical Chemistry* **2021**.
4. Henkel, A. Rod-shaped Plasmoni Sensors. PhD Thesis, Johannes Gutenberg-Universität, Mainz, **2012**.
5. Wulf, V. Dark-field Spectroscopy on Single Plasmonic Gold Nanorods - New Methods. PhD Thesis, Johannes Gutenberg-Universität, Mainz, **2016**.
6. Ye, W. Automated Spectral Imaging Plasmonspectroscopy for Unraveling Molecular Dynamics. PhD Thesis, Johannes Gutenberg-Universität, Mainz, **2018**.
7. Rosman, C. Biological Applications of Plasmonic Metal Nanoparticles. PhD Thesis, Johannes Gutenberg-Universität, Mainz, **2013**.
8. Soille, P. Morphologische Bildverarbeitung: Grundlagen, Methoden, Anwendungen, Ed. Springer Berlin Heidelberg: Berlin, Heidelberg, **1998**.
9. Becker, J. Plasmons as Sensors. PhD, Johannes Gutenberg-Universität Mainz, **2010**.
10. Gans, R. Über die Form ultramikroskopischer Goldteilchen. *Annalen der Physik* **1912**, *342* (5), 881-900.
11. Ye, W.; Celiksoy, S.; Jakab, A.; Khmelinskaia, A.; Heermann, T.; Raso, A.; Wegner, S. V.; Rivas, G.; Schwille, P.; Ahijado-Guzmán, R.; Sönnichsen, C. Plasmonic Nanosensors Reveal a Height Dependence of MinDE Protein Oscillations on Membrane Features. *J. Am. Chem. Soc.* **2018**, *140*, 17901-17906.

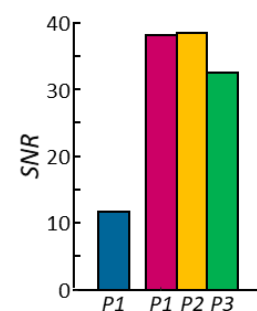


Figure 2.12: Signal-to-noise (SNR) ratio for the particles presented in Figure 2.11 colored respectively.

12. Au - Hoang, T. B.; Au - Huang, J.; Au - Mikkelsen, M. H., Colloidal Synthesis of Nanopatch Antennas for Applications in Plasmonics and Nanophotonics. *JoVE* **2016**, *111*, e53876.
13. Kedem, O.; Tesler, A. B.; Vaskevich, A.; Rubinstein, I. Sensitivity and Optimization of Localized Surface Plasmon Resonance Transducers. *ACS Nano* **2011**, *5*, 748-760.
14. Tian, L.; Chen, E.; Gandra, N.; Abbas, A.; Singamaneni, S. Gold Nanorods as Plasmonic Nanotransducers: Distance-Dependent Refractive Index Sensitivity. *Langmuir* **2012**, *28*, 17435-17442.
15. Ahijado-Guzmán, R.; Prasad, J.; Rosman, C.; Henkel, A.; Tome, L.; Schneider, D.; Rivas, G.; Sönnichsen, C. Plasmonic Nanosensors for Simultaneous Quantification of Multiple Protein–Protein Binding Affinities. *Nano Letters* **2014**, *14*, 5528-5532.
16. Kaefer, K. Plasmonic Gold Nanoparticles as Implantable Medical Sensors. PhD Thesis, Johannes Gutenberg-Universität, Mainz, **2018**.
17. Lambertz, C.; Martos, A.; Henkel, A.; Neiser, A.; Kliesch, T.-T.; Janshoff, A.; Schwille, P.; Sönnichsen, C. Single Particle Plasmon Sensors as Label-Free Technique to Monitor MinDE Protein Wave Propagation on Membranes. *Nano Lett.* **2016**, *16*, 3540-3544.

PART II

PUBLICATIONS

THEORETICAL BACKGROUND

Intensity-Based Single Particle Plasmon Sensing

Sirin Celiksoy, Weixiang Ye, Karl Wandner, Katharina Kaefer and Carsten Sönnichsen

A version of this chapter is published in Nano Letters.

Plasmon sensors respond to local changes of their surrounding environment with a shift in their resonance wavelength. This response is usually detected by measuring light scattering spectra to determine the resonance wavelength. However, single wavelength detection has become increasingly important because it simplifies the setup, increases speed, and improves statistics. Therefore, we investigated theoretically how the sensitivity toward such single wavelength scattering intensity changes depend on the material and shape of the plasmonic sensor. Surprisingly, simple equations describe this intensity sensitivity very accurately and allow us to distinguish the various contributions: Rayleigh scattering, dielectric contrast, plasmon shift, and frequency-dependent plasmon bulk damping. We find very good agreement of theoretical predictions and experimental data obtained by single particle spectroscopy.

3.1 Introduction

Monitoring the light scattered from single plasmonic nanoparticles has become a common technique to observe the binding of unlabeled macromolecules, for example to characterize protein-protein interaction strength or for the multiplexed detection of unknown analytes.¹⁻² Such plasmonic nanosensing applications have recently shifted towards single wavelength detection³⁻⁷, where the change in plasmon resonance position is monitored at a fixed wavelength

resulting in increased speed and simplified setup, and making parallelization easier. However, we noticed that the usual description of plasmonic sensitivity to the binding of macromolecule layers is incomplete when applied to such intensity monitoring schemes. We have therefore revisited this problem and derived surprisingly simple equations that accurately describe the changes in plasmonic light scattering efficiency at a fixed wavelength upon binding of analytes. The derivation is based on Clausius-Mossotti's fundamental light scattering equation which uses the complex susceptibilities of the particle material as input.⁸ We use our theory to identify the various contributions to the light scattering change that are induced by analyte binding: Rayleigh scattering, dielectric contrast, plasmon shift and frequency-dependent plasmon bulk damping. Applying the theory to gold nanorods with different aspect ratio and volume, we show theoretically and experimentally how the plasmonic sensitivity depends on the nanoparticle's dimensions. Our findings provide a conceptual foundation for the 'figure of merit' (FOM), a measure which is used in the literature to characterize and compare plasmonic nanoparticles.⁹⁻¹¹ Furthermore, we demonstrate a path to describe the performance of optical nanosensors without plasmon resonances. Our description offers a framework to analyze and optimize sensors for a given range of situations, for example for differently sized analytes and receptors.

3.2 Results and Discussion

Measurement Principle. In a typical single particle plasmon sensing experiment to detect the binding of an analyte (NanoSPR)¹², particles are immobilized on a transparent substrate and imaged in a dark-field microscope. At and around the plasmon resonance wavelength λ_{res} , the light scattering efficiency is strongly enhanced. This plasmon resonance wavelength λ_{res} shifts by $\Delta\lambda_{\text{res}}$ upon changes in the dielectric environment of the nanoparticles (Figure 3.1) and therefore reports on the adsorption and desorption of macromolecules (usually to receptor molecules permanently bound to the nanoparticle). Alternatively, it is also possible to measure scattering intensity changes ΔI at a given wavelength (the detection wavelength λ_{D} , cf. Figure 3.1). Indeed, plasmon shifts are much more robust against experimental problems than scattering intensity changes. Such difficulties can also result from defocusing, drift, changes of the illumination light intensity, or changes in background scattering due to impurities in the sample, dust, or aggregates of the analyte. However, single wavelength detection is becoming increasingly popular due to the much greater detection speed and the simplicity of the setup.³⁻⁵ We expect that this trend will continue, especially for commercial instruments that rely on single particle light scattering.

Previous work. In our previous work¹³, we have already envisioned this trend towards single wavelength detection. We theoretically investigated changes to the light scattering efficiency of gold nanorods after the binding of an adsorbate layer with thickness l . In that work, we defined a 'figure of merit' for layers

FOM_{layer}^{*} by $\text{FOM}_{\text{layer}}^* = \frac{dI_{\text{rel}}}{dl}$ (where, dI_{rel} is the relative scattering intensity change $dI_{\text{rel}} = \frac{dI}{I_0}$ induced by a small change of adsorbate layer thickness dl). Since $\text{FOM}_{\text{layer}}^*$ decreases with increasing distance from the surface, we used the value at the surface ($\lim_{l \rightarrow 0}$) as a parameter to compare different particles. We now name this quantity the ‘intensity surface sensitivity’ \mathcal{S}_I (‘S cedilla’, pronounced *sh* as in shoe). \mathcal{S}_I describes how sensitive the system is to a layer thickness change at the particle’s surface (formal definition is $\mathcal{S}_I = \lim_{l \rightarrow 0} \frac{dI_{\text{rel}}}{dl}$; we refer to \mathcal{S}_I internally as the ‘Şirin index’ after its inventor). We can also define an equivalent resonance wavelength surface sensitivity \mathcal{S}_λ , if we consider the ‘signal’ as a resonance wavelength shift $\Delta\lambda_{\text{res}}$ (as used in the traditional single particle plasmon sensing or ‘NanoSPR’ schema). This resonance wavelength surface sensitivity \mathcal{S}_λ is then given by $\mathcal{S}_\lambda = \lim_{l \rightarrow 0} \frac{d\lambda_{\text{res}}}{dl}$.

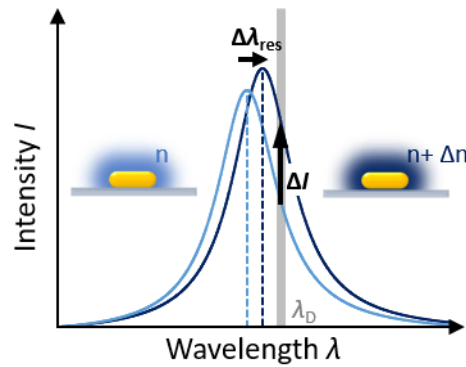


Figure 3.1: Plasmon Principle. Sketch of the scattering intensity I of a gold nanorod as a function of wavelength λ (blue line). When the refractive index in the vicinity of the nanoparticle changes by Δn (insets), the plasmon resonance shifts to a larger wavelength by $\Delta\lambda_{\text{res}}$ (dark blue line) causing an increase in the scattering intensity ΔI (black arrow) at the detection wavelength λ_D (gray bar).

The ‘sensitivity’ measure commonly used to describe, characterize, and compare plasmonic nanosensors, is the resonance wavelength refractive index sensitivity $\mathcal{S}_\lambda = \frac{d\lambda_{\text{res}}}{dn}$ (note the missing cedilla!). The equivalent intensity refractive index sensitivity is defined as $\mathcal{S}_I = \frac{dI_{\text{rel}}}{dn}$. These refractive index sensitivities (also referred to as bulk sensitivities¹⁰) are easily measured by recording the particles’ response in several media with slightly different refractive indices. Thus, \mathcal{S}_λ has become the dominant quantity to compare plasmonic sensors.¹⁴⁻¹⁵ However, the bulk sensitivities \mathcal{S}_λ and \mathcal{S}_I do not account for the fact that the response of plasmonic particles to environmental changes is distance-dependent. Generally, a refractive index change in a layer near the particle’s surface induces larger changes than the same refractive index change in a layer further away from the particle.¹⁶ In good approximation, the response $\Delta\lambda_{\text{res}}$ induced by an adsorbate layer with thickness l decreases exponentially with distance from the nanoparticle according to¹⁷⁻¹⁸

$$\Delta\lambda_{\text{res}} = S_{\lambda}\Delta n \left(1 - e^{-\frac{l}{d_s}}\right) \quad (1)$$

*Sometimes, the sensing distance is described by the decay length of the plasmonic electric field l_D ¹⁷. Since the plasmon sensitivity is proportional to the square of the electric field, $d_s = l_D/2$.

Here, the sensing distance d_s^* is the characteristic length scale at which a refractive index change influences the plasmonic resonance. We have previously found¹⁸ that the sensing distance for gold nanorods is, in good approximation, proportional to the ‘effective radius’ $V^{1/3}$ with $d_s \approx 0.37V^{1/3}$. Essentially, the sensing distance is related to the strength of the electric fields of the plasmon.¹⁹ From equation (1), we can relate ζ_{λ} (i.e. the plasmon resonance wavelength change $\Delta\lambda_{\text{res}}$ induced by a small layer dl) to the resonance wavelength refractive index sensitivity S_{λ} by

$$(2) \quad \zeta_{\lambda} = \lim_{l \rightarrow 0} \frac{d\lambda_{\text{res}}}{dl} = \frac{S_{\lambda}\Delta n}{d_s}$$

As we can see from equation (2), $\zeta_{\lambda}^{\dagger}$ is proportional to the ratio of S_{λ} and d_s , which *a posteriori* justifies the use of S_{λ} for the comparison of plasmonic nanoparticles for cases where d_s stays constant.

†Jiaqi Li *et al.*²⁰ found a similar result by looking at a quantity they termed ‘surface sensitivity’ ($\partial^2\lambda_{\text{res}}/\partial l \partial n$).

They used a double differential to capture the effect of both refractive index sensitivity and layer thickness. We choose to keep both types of sensitivity separate because this allows us to use the surface sensitivity in other circumstances where the refractive index sensitivity is difficult to define – as for example for sensing with dielectric nanoparticles.

More interesting than the resonance wavelength surface sensitivity ζ_{λ} is the intensity surface sensitivity ζ_I . This quantity describes the signal change expected from the adsorption of a small layer at a given wavelength. The advantage of ζ_I compared to ζ_{λ} that it is also defined for non-resonant nanoparticles, where no ‘resonance wavelength’ can be determined. In another publication²¹, we explored the response of spherical dielectric nanoparticles (e.g. silica nanoparticles) to adsorbate layers and found the relationship $\zeta_I = \frac{6}{r}$. The ζ_I value for plasmonic particles is more complex and depends, among other things, on wavelength. Since an equation equivalent to equation (1) also holds true for intensities, the intensity surface sensitivity ζ_I is related to the intensity bulk sensitivity S_I by

$$(3) \quad \zeta_I = \frac{S_I\Delta n}{d_s}$$

Up to now, we have defined four different types of sensitivities, the intensity surface sensitivity ζ_I , the resonance wavelength surface sensitivity ζ_{λ} , the resonance wavelength bulk sensitivity S_{λ} and the intensity bulk sensitivity S_I - the definitions are summarized in Table B4 in the supporting information.

Mathematical model for the intensity bulk sensitivity S_I . To estimate S_I for plasmonic nanoparticles, it is useful to separate two effects that make up the overall intensity change at the detection wavelength: Firstly, a shift of the resonance wavelength ($S_{I_{\text{shift}}}$) and secondly, an overall intensity increase of the plasmon resonance peak maximum ($S_{I_{\text{max}}}$): $S_I = S_{I_{\text{shift}}} + S_{I_{\text{max}}}$ (cf. Figure 3.2a). Both terms are affected by changes in resonance linewidth Γ . However, the dominant factor is the change of the resonance wavelength, and therefore we first ignore the change in overall intensity and resonance linewidth. With these simplifications, it is easy to show that the optimal detection wavelength λ_D is near the inflection point of the plasmon resonance peak and given by: $\lambda_D = \lambda_{\text{res}} + \frac{\Gamma}{2}$

(see Appendix Figure B.5). A shift of the resonance peak by $\Delta\lambda_{\text{res}}$ induces an intensity change ΔI_{rel} at the detection wavelength λ_{D} proportional to the slope $\frac{dI_{\text{rel}}}{dn}$ at this point. In the Appendix we derive that at $\lambda_{\text{D}} = \lambda_{\text{res}} + \frac{\Gamma}{2}$, the relative intensity change is $\Delta I_{\text{rel}} = \frac{2}{\Gamma} \Delta\lambda_{\text{res}}$. With this relationship, we can compute this part of the 'intensity bulk sensitivity' S_{I} as: $S_{\text{I}_{\text{shift}}} \approx \frac{2S_{\lambda}}{\Gamma}$. Interestingly, this relationship is very close to the 'figure of merit' $FOM = \frac{(\Delta\lambda_{\text{res}}/\Delta n)}{\Gamma} = \frac{S_{\lambda}}{\Gamma}$ that is often used to characterize plasmonic nanosensors and was defined *at hoc* a long time ago.⁹⁻¹¹ This similarity justifies why FOM describes a large part of the plasmonic nanosensor performance.

A small correction arises from the change in linewidth $\frac{d\Gamma}{dn}$ associated with a refractive index change. We present in the Appendix, that this correction leads to a contribution of $\frac{S_{\lambda}}{\Gamma} \frac{d\Gamma}{d\lambda_{\text{res}}}$ resulting in an overall equation: $S_{\text{I}_{\text{shift}}} = \frac{2S_{\lambda}}{\Gamma} + \frac{S_{\lambda}}{\Gamma} \frac{d\Gamma}{d\lambda_{\text{res}}}$. The pink line in Figure 3.2b shows this quantity as a function of resonance wavelength for gold nanorods. Until now, we have ignored the overall scattering intensity increase of the plasmon resonance resulting from a refractive index change, which is described by $S_{\text{I}_{\text{max}}}$. To calculate

$S_{\text{I}_{\text{max}}}$, we use $I_{\text{max}} = \text{const} \cdot \left. \frac{n^8}{\lambda_{\text{res}}^4 \cdot \varepsilon_2^2} \right|_{\lambda_{\text{res}}}$.²²

The resulting equation is $S_{\text{I}_{\text{max}}} = \frac{8}{n} + \frac{-4S_{\lambda}}{\lambda_{\text{res}}} + \frac{-2S_{\lambda}}{\varepsilon_2} \frac{d\varepsilon_2}{d\lambda_{\text{res}}}$ (cf. Appendix Chapter B for details) with n being the medium's refractive index and ε_2 the imaginary part of the particle's dielectric function.

To verify the mathematical description for both terms, $S_{\text{I}_{\text{shift}}}$ and $S_{\text{I}_{\text{max}}}$, we calculated plasmon spectra for small gold nanorods of different aspect ratio embedded in water ($n = 1.33$) and a slightly higher refractive index material ($n = 1.331$) by solving the Maxwell-equations within the quasi-static approximation.¹³ From those simulated spectra, we extracted λ_{res} , Γ and calculated S_{λ} . These values allow us to compare the values for $S_{\text{I}_{\text{shift}}}$ and $S_{\text{I}_{\text{max}}}$ that are directly calculated from the spectra (Figure 3.2b, points) with those from the equations above (Figure 3.2b, lines). It is evident from Figure 3.2 that the equations predict the results very accurately. For larger wavelengths (above 700 nm), the contribution from intensity changes $S_{\text{I}_{\text{max}}}$ becomes very small and $S_{\text{I}_{\text{shift}}}$ is almost constant at around 25/RIU. Below 700 nm, the $S_{\text{I}_{\text{shift}}}$ contribution gradually increases, whereas $S_{\text{I}_{\text{max}}}$ lies around 6/RIU, which is more or less constant until $\lambda_{\text{res}} = 650$ nm, before it starts to rapidly decrease to values between 0/RIU and 1/RIU. It is therefore possible to distinguish two different regions (marked I and II in Figure 3.2b) depending on which of the two terms dominates, with a broad transition region in between. The most relevant region for sensing is the near-infrared area above 700 nm (region II), where, for many technical reasons, most plasmonic nanosensors operate.

When combining both terms into an overall expression for the intensity bulk sensitivity S_I , we can see that $\frac{S_\lambda}{\Gamma} \frac{d\Gamma}{d\lambda_{\text{res}}}$ and $\frac{S_\lambda}{\epsilon_2} \frac{d\epsilon_2}{d\lambda_{\text{res}}}$ are almost identical on the scale of the complete equation (Appendix Figure B.4). Since these expressions exist in both terms, the overall equation is simplified to

$$(4) \quad S_I = S_{I_{\text{shift}}} + S_{I_{\text{max}}} = \frac{2S_\lambda}{\Gamma} + \frac{8}{n} - \frac{4S_\lambda}{\lambda_{\text{res}}} - \frac{S_\lambda}{\epsilon_2} \frac{d\epsilon_2}{d\lambda_{\text{res}}}$$

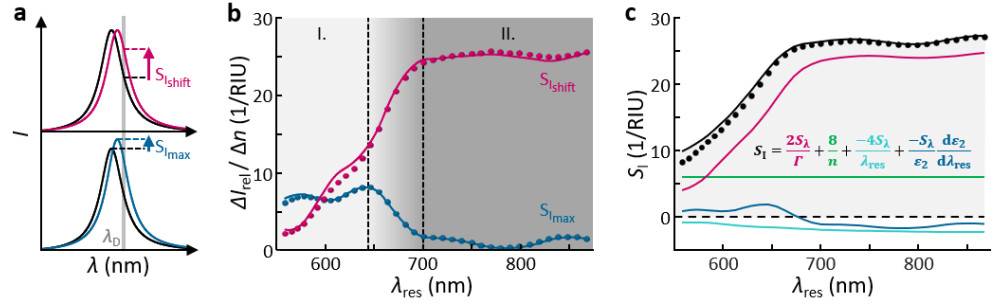


Figure 3.2: Mathematical model for the intensity bulk sensitivity S_I . **a)** Schematics of the scattering spectra before (black lines) and after (pink and blue lines) the nanoparticle's local refractive index changes. The overall intensity change at the detection wavelength λ_D (gray bar) is comprised of two effects: the shift of the resonance wavelength ($S_{I_{\text{shift}}}$, pink arrow, upper panel) and an overall intensity increase of the plasmon resonance peak maximum I_{max} ($S_{I_{\text{max}}}$, blue arrow, lower panel). **b)** Trend of $S_{I_{\text{shift}}}$ (in pink) and $S_{I_{\text{max}}}$ (in blue) as a function of resonance wavelength λ_{res} . The lines represent the theoretically expected behavior for both parameters and the data points are values simulated using the quasi-static approximation (QSA). The grey backgrounds differentiate two areas where either the $S_{I_{\text{shift}}}$ (in dark grey) dominates or $S_{I_{\text{max}}}$ (light grey) contributes approximately equally to the overall equation of S_I . **c)** Different contributions of the intensity bulk sensitivity S_I (black line) as a function of resonance wavelength λ_{res} . The terms are assigned as plasmon shift (pink line), dielectric contrast (green line), Rayleigh scattering (cyan line) and frequency-dependent plasmon damping (blue line). The inset shows the equation for S_I , color coded with the same colors as the lines. The data points (black dots) are values of S_I simulated using QSA.

Figure 3.2c depicts that this equation (black line) accurately describes the simulated spectra (black dots). We represent the four contributions to the overall value of S_I in the above equation using separate lines and name them as plasmon shift (pink), dielectric contrast (green), Rayleigh scattering (cyan), and frequency-dependent plasmon damping (blue). The plasmon shift term $\frac{2S_\lambda}{\Gamma}$ dominates, especially at larger wavelengths. The contrast term adds a constant value of around $6/\text{RIU}$ (in water) whereas the remaining contributions give only very small (negative) corrections, particularly in the near-infrared region, which reduce the influence of the contrast term even more. Therefore, it is quite reasonable to use $S_I \approx \frac{2S_\lambda}{\Gamma}$ for gold nanorods with resonances above 700 nm (which means for nanorods with an aspect ratio above 3).[§] However, this simplification is clearly wrong for gold nanospheres, where the strong contribution from interband damping (d-electrons) leads to a dominant contribution from the change in maximum intensity ($S_{I_{\text{max}}}$). We also tested

[§]Since $S_I \approx \frac{2S_\lambda}{\Gamma}$ is, except for a factor 2, identical to the old 'figure of merit', this older parameter for the characterization and comparison of plasmonic structures substantially underestimated the performance of gold nanospheres for intensity-based sensing.

equation (4) for other materials, specifically silver, aluminum and copper. Again, the values from simulations within the quasi-static approximation agree well with the prediction from equation (4) and the plasmon shift term $\frac{2S_\lambda}{r}$ dominates (cf. Appendix Figure B.6).

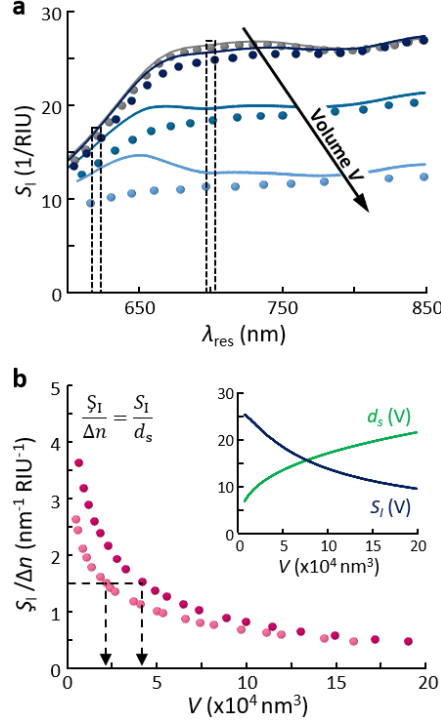


Figure 3.3: Volume dependency of the intensity bulk sensitivity S_I and the intensity surface sensitivity S_s . **a)** Intensity bulk sensitivity S_I as function of resonance wavelength λ_{res} calculated with our mathematical model (lines) and simulated data using the quasi-static approximation (QSA, grey dots) and the boundary-element-method (BEM) for increasing volumes (black arrow) mimicking small ($V = 1 \cdot 10^4 \text{ nm}^3$, dark blue dots), medium ($V = 5 \cdot 10^4 \text{ nm}^3$, blue dots) and big sized particles ($V = 15 \cdot 10^4 \text{ nm}^3$, light blue dots). Black dashed boxes mark the data used for Figure 3.3b. **b)** Intensity surface sensitivity S_s (normalized to the bulk refractive index change Δn) as a function of volume V for two different resonance wavelengths $\lambda_{res} = 620 \text{ nm}$ (light pink dots) and $\lambda_{res} = 700 \text{ nm}$ (pink dots) – implying a different aspect ratio for the nanorods in both series. The dashed lines show that gold nanorods with different volume ($V = 2.2 \cdot 10^4 \text{ nm}^3$ or $V = 4.2 \cdot 10^4 \text{ nm}^3$) can have the same normalized Sirin Index of $1.5 \text{ nm}^{-1} \text{RIU}^{-1}$ depending on their resonance wavelength (aspect ratio). The inset shows both components, S_I and d_s , of the intensity surface sensitivity S_s as a function of the volume V at $\lambda_{res} = 700 \text{ nm}$.

Verification of theory for SI with QSA and BEM simulations. So far, we have treated the nanoparticles as being very small compared to the light wavelength (quasi-static approximation). We know that for particles with diameters above 10 nm, this approximation starts to break down, and experimental spectra disagree with those calculations. To check if equation (4) still works for larger nanoparticles, we tested it with the spectra of larger gold nanorods simulated with the boundary-element-method (BEM)²³. Again, we extracted λ_{res} , I and S_λ from those simulated spectra. Figure 3.3a shows the

intensity bulk sensitivity S_I calculated directly from the spectra (points) compared to the result of equation (4) (lines). Generally, S_I decreases for bigger particles and depends less on the wavelength, presumably because radiation damping increases. Equation (4) describes the intensity bulk sensitivity S_I reasonably well for small particles and also for larger particles that are in the near-infrared wavelength range (above 700 nm). Coming back to the intensity surface sensitivity ζ_I we investigated, how it is influenced by particle volume at a fixed wavelength. Figure 3b represents the downward trend of ζ_I with increasing volume. Both components of ζ_I , S_I and ds are volume-dependent (cf. inset), and contribute about equally to the observed trend in ζ_I . Comparing the intensity surface sensitivity at two different wavelengths, 620 nm (light pink dots) and 700 nm (pink dots), we observe a large difference for smaller particles (left side of Figure 3b) that becomes smaller for larger particles (right side of Figure 3b). For instance, the same normalized ζ_I of $1.5 \text{ nm}^{-1} \text{ RIU}^{-1}$ (marked as dashed line) is achieved for particles of smaller volume ($2.2 \cdot 10^4 \text{ nm}^3$ at $\lambda_{\text{res}} = 620 \text{ nm}$, which corresponds to a particle of $25.4 \text{ nm} \times 50.8 \text{ nm}$) and higher volume ($4.2 \cdot 10^4 \text{ nm}^3$ at $\lambda_{\text{res}} = 700 \text{ nm}$, which means a particle of $28.7 \text{ nm} \times 74.6 \text{ nm}$). A normalized ζ_I of $1.5 \text{ nm}^{-1} \text{ RIU}^{-1}$ describes an increase in relative scattering intensity of 18 % at the optimal detection wavelength λ_D for a nanoparticle in water ($n = 1.33$) and for a 1 nm layer with a refractive index of $n_{\text{layer}} = 1.45$. We chose these values to mimic the adsorption of a small protein. Our measurement instruments are able to detect relative intensity changes of 1% reliably on single particles. This shows the potential of the method to detect sub-nm layers and single proteins.

Experimental data follows trend predicted by mathematical models. To test the equations, we compare their predictions with experiments on particles immobilized on a glass substrate. We accounted for the glass substrate, which reduces the accessible surface to about 60% (Appendix Figure B.3b) and adjusted the experimental data accordingly. Figure 3.4a shows experimental values of individual nanosensors (colored transparent dots) for the intensity bulk sensitivity S_I compared to the theoretical expectation (gray area). The gray area corresponds to the values for nanoparticles with volumes within one standard deviation of the mean. The experimental points lie within this expected area, especially if we calculate the mean of the experimental values for the three particle batches used in this work (colored dots). To measure the absolute values of the ζ_I , it is necessary to add a layer with known thickness and refractive index on top of bare nanoparticles. We were able to observe the predicted trend of decreasing ζ_I with increasing particle volume (Figure 3.4b) by using the mean of individual particle measurements. In this analysis, we used particle specific detection wavelengths for a closer match between theory and experiment. However, our equations predict equally well the experimental outcome when using a common detection wavelength (Figure B2), which would be the situation in a real device. It is also possible to use the equation to predict the response of an ensemble of particles (Figure B2), simplifying the device even more by eliminating the need for single particle microscopy. The measurements show the

validity of the theoretical description we developed to describe intensity-based plasmon detection.

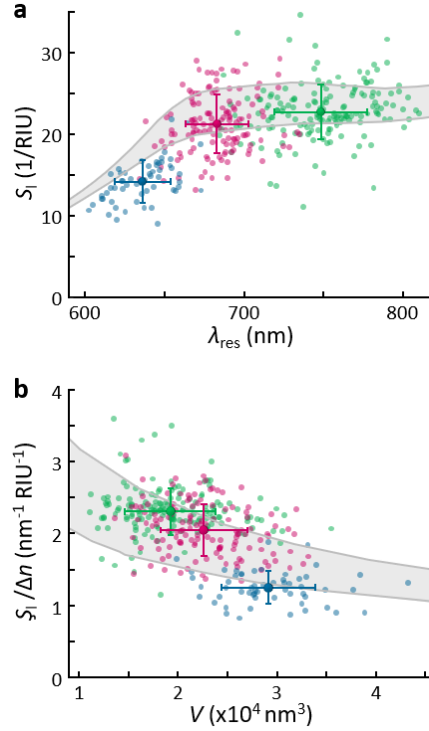


Figure 3.4: Comparison of experimental data to our mathematical description for the intensity bulk sensitivity S_I and the intensity surface sensitivity S_I . **a)** Intensity bulk sensitivity S_I of single gold nanorods (blue, pink and green transparent dots) as a function of resonance wavelength λ_{res} . The gray shaded area shows the predictions of the quasi-static approximation (QSA) for small sized particles (upper grey line) and data obtained with the boundary element method (BEM) for particles with an average volume of $V = 3.4 \cdot 10^4 \text{ nm}^3$ (lower grey line). The colored data points represent the mean for S_I and λ_{res} of the three gold nanorod batches respectively, and the error bars represent the standard deviations. **b)** Intensity surface sensitivity S_I (normalized to the bulk refractive index change Δn) of single gold nanorods (blue, pink and green transparent dots) as a function of particle volume V . The gray shaded area indicates the results of BEM simulations for particles with an average resonance wavelength of $\lambda_{res} = 619 \text{ nm}$ (lower grey line) and $\lambda_{res} = 777 \text{ nm}$ (upper grey line). The colored data points depict the mean for S_I and V of the three gold nanorod batches respectively, and the error bars show the standard deviations. Note: The experimental data is adjusted for the fact that only 60% of the nanoparticles sensing volume is available.

3.3 Conclusion

We suggest that the intensity bulk sensitivity S_I and especially the intensity surface sensitivity S_I are very useful parameters when choosing particles for plasmon sensors that complement the ‘traditional’ plasmonic sensitivity parameter S_λ (the resonance wavelength refractive index sensitivity). For gold nanoparticles, we have shown that S_I is highest for those nanoparticles with plasmon resonances above 700 nm and is approximately given by $S_I \approx \frac{2S_\lambda}{r}$ at these wavelengths. This value resembles the ‘figure of merit’ (*FOM*) that has

been used to compare plasmonic structures. Furthermore, we found that S_1 decreases for increasing particle volume, emphasizing the advantage of using the smallest particles possible. A major benefit of the parameters S_1 and \mathcal{S}_1 is that they can be used to compare different nanosensors: plasmonic nanosensors of different materials and shapes, as well as non-plasmonic nanosensors such as dielectric nanoparticles.

3.4 Author Contributions

S.C., W.Y. and C.S. initiated and designed the research. S.C. and W.Y. derived the mathematical models under the guidance of C.S.. S.C., W.Y. and K.W. performed the experiments and interpreted the data. W.Y. simulated the data using the boundary element method (BEM) and S.C. the data using the quasi-static approximation (QSA). K.K. provided gold nanorods and helped to interpret the data. The manuscript text was written by S.C. and C.S.. S.C. prepared all figures.

3.5 Acknowledgement

This work was financially supported by the ERC Grant 259640 (“*SingleSense*”). W.Y. was funded by the Graduate School of Excellence Materials Science in Mainz (GSC 266). Eva Wächtersbach helped with experiments. We thank Rubén Ahijado-Guzmán and Qian Du for fruitful discussions. We thank Felix Schlapp for technical assistance with the table of content (TOC) figure.

3.6 Bibliography

1. Anker, J. N.; Hall, W. P.; Lyandres, O.; Shah, N. C.; Zhao, J.; Van Duyne, R. P. Biosensing with Plasmonic Nanosensors. *Nat.Mater.* **2008**, *7*, 442-453.
2. Mayer, K. M.; Hafner, J. H. Localized Surface Plasmon Resonance Sensors. *Chem. Rev.* **2011**, *111*, 3828-3857.
3. Baaske, M. D.; Neu, P. S.; Orrit, M. Label-Free Plasmonic Detection of Untethered Nanometer-Sized Brownian Particles. *ACS Nano* **2020**, *14*, 14212-14218.
4. Celiksoy, S.; Ye, W.; Wandner, K.; Schlapp, F.; Kaefer, K.; Ahijado-Guzmán, R.; Sönnichsen, C. Plasmonic Nanosensors for the Label-Free Imaging of Dynamic Protein Patterns. *J. Phys. Chem. Lett.* **2020**, *11*, 4554-4558.
5. Beuwer, M. A.; Prins, M. W. J.; Zijlstra, P. Stochastic Protein Interactions Monitored by Hundreds of Single-Molecule Plasmonic Biosensors. *Nano Lett.* **2015**, *15*, 3507-3511.
6. Visser, E. W. A.; Horáček, M.; Zijlstra, P., Plasmon Rulers as a Probe for Real-Time Microsecond Conformational Dynamics of Single Molecules. *Nano Lett.* **2018**, *18*, 7927-7934.
7. Zijlstra, P.; Paulo, P. M. R.; Orrit, M. Optical Detection of Single Non-Absorbing Molecules Using the Surface Plasmon Resonance of a Gold Nanorod. *Nat. Nanotechnol.* **2012**, *7*, 379-382.

8. Gans, R. Über die Form ultramikroskopischer Goldteilchen. *Annalen der Physik* **1912**, *342*, 881-900.
9. Sherry, L. J.; Chang, S.-H.; Schatz, G. C.; Van Duyne, R. P.; Wiley, B. J.; Xia, Y. Localized Surface Plasmon Resonance Spectroscopy of Single Silver Nanocubes. *Nano Lett.* **2005**, *5*, 2034-2038.
10. Otte, M. A.; Sepúlveda, B.; Ni, W.; Juste, J. P.; Liz-Marzán, L. M.; Lechuga, L. M. Identification of the Optimal Spectral Region for Plasmonic and Nanoplasmonic Sensing. *ACS Nano* **2010**, *4*, 349-357.
11. Li, J.; Ye, J.; Chen, C.; Hermans, L.; Verellen, N.; Ryken, J.; Jans, H.; Van Roy, W.; Moshchalkov, V. V.; Lagae, L.; Van Dorpe, P. Biosensing Using Diffractively Coupled Plasmonic Crystals: the Figure of Merit Revisited. *Adv. Opt. Mater.* **2015**, *3*, 176-181.
12. Ahijado-Guzmán, R.; Prasad, J.; Rosman, C.; Henkel, A.; Tome, L.; Schneider, D.; Rivas, G.; Sönnichsen, C., Plasmonic Nanosensors for Simultaneous Quantification of Multiple Protein-Protein Binding Affinities. *Nano Lett.* **2014**, *14*, 5528-5532.
13. Becker, J.; Trügler, A.; Jakab, A.; Hohenester, U.; Sönnichsen, C. The Optimal Aspect Ratio of Gold Nanorods for Plasmonic Bio-sensing. *Plasmonics* **2010**, *5*, 161-167.
14. Chen, H.; Kou, X.; Yang, Z.; Ni, W.; Wang, J. Shape- and Size-Dependent Refractive Index Sensitivity of Gold Nanoparticles. *Langmuir* **2008**, *24* (10), 5233-5237.
15. Khan, A. U.; Zhao, S.; Liu, G. Key Parameter Controlling the Sensitivity of Plasmonic Metal Nanoparticles: Aspect Ratio. *J. Phys. Chem. C* **2016**, *120*, 19353-19364.
16. Nusz, G. J.; Curry, A. C.; Marinakos, S. M.; Wax, A.; Chilkoti, A. Rational Selection of Gold Nanorod Geometry for Label-Free Plasmonic Biosensors. *ACS Nano* **2009**, *3*, 795-806.
17. Malinsky, M. D.; Kelly, K. L.; Schatz, G. C.; Van Duyne, R. P. Chain Length Dependence and Sensing Capabilities of the Localized Surface Plasmon Resonance of Silver Nanoparticles Chemically Modified with Alkanethiol Self-Assembled Monolayers. *J. Am. Chem. Soc.* **2001**, *123*, 1471-1482.
18. Ye, W.; Celiksoy, S.; Jakab, A.; Khmelinskaia, A.; Heermann, T.; Raso, A.; Wegner, S. V.; Rivas, G.; Schwille, P.; Ahijado-Guzmán, R.; Sönnichsen, C. Plasmonic Nanosensors Reveal a Height Dependence of MinDE Protein Oscillations on Membrane Features. *J. Am. Chem. Soc.* **2018**, *140*, 17901-17906.
19. Yang, J.; Giessen, H.; Lalanne, P. Simple Analytical Expression for the Peak-Frequency Shifts of Plasmonic Resonances for Sensing. *Nano Lett.* **2015**, *15*, 3439-3444.
20. Li, J. Q.; Ye, J.; Chen, C.; Li, Y.; Verellen, N.; Moshchalkov, V. V.; Lagae, L.; Van Dorpe, P. Revisiting the Surface Sensitivity of Nanoplasmonic Biosensors. *ACS Photonics* **2015**, *2*, 425-431.

21. Celiksoy, S.; Ye, W.; Ahijado-Guzmán, R.; Sönnichsen, C. Single Out-of-Resonance Dielectric Nanoparticles as Molecular Sensors. *Nano Lett.* **2021**, DOI: 10.1021/acssensors.0c02629.
22. Foerster, B.; Rutten, J.; Pham, H.; Link, S.; Sönnichsen, C. Particle Plasmons as Dipole Antennas: State Representation of Relative Observables. *J. Phys. Chem. C* **2018**, *122*, 19116-19123.
23. Hohenester, U.; Trügler, A. MNPBEM – A Matlab toolbox for the simulation of plasmonic nanoparticles. *Comput. Phys. Comm.* **2012**, *183*, 370-381.

Plasmonic Nanosensors for the Label-Free Imaging of Dynamic Protein Patterns

Sirin Celiksoy, Weixiang Ye, Karl Wandner, Felix Schlapp, Katharina Kaefer, Rubén Ahijado-Guzmán* and Carsten Sönnichsen*

*Corresponding Authors

A version of this chapter is published in Journal of Physical Chemistry Letters.

We introduce a new approach to monitor the dynamics and spatial patterns of biological molecular assemblies. Our molecular imaging method relies on plasmonic gold nanoparticles as point-like detectors and requires no labeling of the molecules. We show spatial resolution of up to 5 μm and 30 ms temporal resolution, which is comparable to wide-field fluorescence microscopy, while requiring only readily available gold nanoparticles and a dark-field optical microscope. We demonstrate the method on MinDE proteins attaching to and detaching from lipid membranes of different composition for 24 hours. We foresee our new imaging method as an indispensable tool in advanced molecular biology and biophysics labs around the world.

4.1 Introduction

Living organisms use dynamic self-assembly processes to create structures on microscopic and macroscopic levels.¹⁻³ To follow the dynamics of such molecular interactions in real-time, biophysicists usually rely on fluorescent dyes chemically attached to the molecules of interest.^{4,5} More recently, high-speed atomic force microscopy (HS-AFM) has developed into a highly accurate but somewhat invasive alternative.^{6,7} For both methods, much care has to be taken

to mitigate the distortion caused to the molecular system under investigation.⁸⁻¹¹ A method to study the dynamics of cellular processes without the need for labeling is surface plasmon resonance imaging (SPRi) combined with electrochemical impedance spectroscopy (EIS).¹² Plasmonic nanoparticles (nanoSPR) are an alternative to all those methods that also require no labeling and exhibit a very small and easily tunable sensing depth allowing to resolve molecular interactions more accurately in comparison to SPRi with a sensing depth in the order of hundred nanometers. We demonstrate this concept using membrane-coated plasmonic gold nanorods as point-like sensors to record surface coverage fluctuations generated by a dynamic membrane-protein interaction. We monitor hundreds of plasmonic nanosensors in parallel with 30 ms temporal resolution to generate real-time and real-space movies of the protein waves.

We demonstrate that this imaging nanoparticle-SPR method ('i-nSPR') is not only able to resolve local protein coverage changes but also to report on their spatiotemporal correlation. Imaging with plasmonic nanoparticles permits to measure the interaction indefinitely without having to worry about bleaching. Our novel i-nSPR method could be combined with the determination of binding constants and molecular distances^{13,14} and requires only plasmonic nanoparticles and a standard optical wide-field microscope. Nanoparticle-SPR (nanoSPR) uses plasmonic nanoparticles, usually gold nanorods, as sensing elements.¹³ Such plasmonic particles have a strong light scattering and absorption maximum at the plasmon resonance. The resonance position is influenced by the dielectric environment in the nanoparticle's close proximity and changes upon binding and desorption of macromolecules. Plasmonic nanoparticles have been used for the detection of protein interactions on membranes and shown to reach single-molecule resolution.¹⁵⁻¹⁸ Here, we extend nanoSPR considerably by monitoring hundreds of plasmonic nanoparticles on the flowcell's surface in parallel in an optical microscope under dark-field illumination. In contrast to previous studies, we use the position of every single nanoparticle to reconstruct an image of the observed molecular interaction pattern.

4.2 Results and Discussion

Measurement Principle. The basis for detecting changes in single-particle plasmon resonances is a dark-field microscope. Figure 4.1a illustrates the light-pathway of such a dark-field microscope (see Appendix Chapter C for details on the nanoparticles, the microscope setup and a discussion about particle heating). Due to the large scattering cross-section near the plasmon resonance, gold nanorods appear as red spots on a dark background when illuminated with white light (Figure 4.1b) in such dark-field configuration. In most of the cases, plasmon sensing relies on measuring the spectral shift of the plasmon resonance as an indicator for changes in the dielectric environment. Here, we simplify these measurements to achieve enough statistics for analyzing spatial-temporal correlations by looking only for the intensity at a single wavelength (detection wavelength λ_D).^{17,20} By analyzing the nanoparticles' relative scattering intensity

changes $\Delta I_{\text{rel}} = \Delta I / I_0$ at this detection wavelength, we are able to see changes in the dielectric environment near the corresponding nanoparticle (Figure 4.1c).

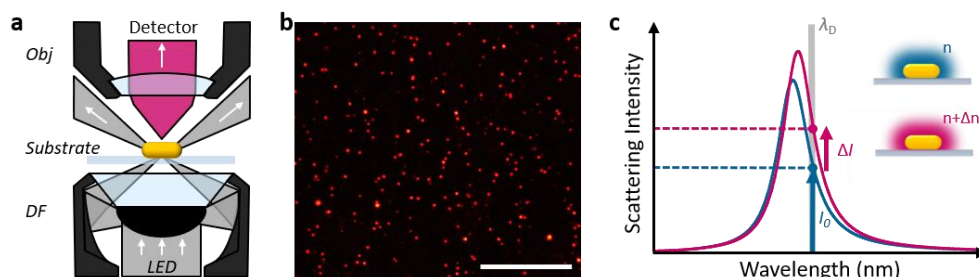


Figure 4.1: Nanoparticle-SPR (nanoSPR) sensing principle. **a)** Schematics of the light pathway in the upright dark-field microscope. The light emitted by a halogen lamp or a LED is focused on the sample (light gray) under oblique angles through a dark-field condenser (*DF*). Only light scattered from plasmonic nanoparticles (pink) enters the objective (*Obj*) and is directed to a detector. **b)** Real-color dark-field image of randomly deposited gold nanorods under white light illumination (scalebar 100 μm). Each nanorod appears as a small red dot due to the strongly enhanced resonant light scattering at the plasmon resonance. **c)** The scattering intensity (blue line) shows a broad peak with a characteristic maximum at the plasmon resonance wavelength. When the refractive index around the nanoparticle changes by Δn (insets), the plasmon shifts to larger wavelengths (pink line). At the detection wavelength λ_D , the scattering intensity increases by ΔI (dashed lines). We use the relative intensity change $\Delta I_{\text{rel}} = \Delta I / I_0$ to monitor refractive index changes Δn .

Example time traces of Min oscillations. We aim here to investigate this single wavelength intensity monitoring concept for detecting spatial and temporal variations of protein coverage at many nanosensors within the field of view. As a model system, we chose the ‘Min’ protein system that is known to periodically attach to and detach from a lipid membrane. This oscillation happens on the minute timescale with spatial patterns in the 10-100 μm regime, the ‘Min waves’.²¹ A simple model to describe the Min oscillations mechanism is the four-step cycle schematically depicted in Figure 4.2a, where initially MinD proteins attach to the membrane (I), recruiting MinE proteins (II) that eventually detach together with MinE (III). Bulk diffusion, membrane diffusion, and cooperative binding effects lead to the synchronization of this cycle in adjacent areas resulting in the spontaneous formation of spatial patterns that travel as waves over the surface.^{1,21} The local changes in MinDE coverage on top of the membrane affects the plasmonic nanosensors underneath, inducing variations of the relative scattering intensity ΔI_{rel} . We have used plasmonic nanosensors before to unravel the exact binding mode within the Min dynamics.¹⁴

However, we just recently have had enough dynamic range to accurately map the spatiotemporal evolution of the plasmon resonance position to a specific location on the substrate. To verify our imaging concept, we first immobilized gold nanorods on the bottom of our microfluidic flow chamber. Figure 4.2b shows a section of the field of view of the particles, illuminated in dark-field configuration with a light emitting diode (LED) at a single wavelength (detection wavelength λ_D). To reconstitute the protein-membrane system after the

nanoparticle deposition, we spread a supported lipid bilayer on our sensors (cf. Appendix Chapter C). After membrane deposition, we incubated with the proteins MinD and MinE in the appropriate buffer and waited for the spatially correlated oscillation to form. We recorded these oscillations for 24 hours in the complete field of view with 30 ms temporal resolution by following the elastic light scattering intensity of all particles.

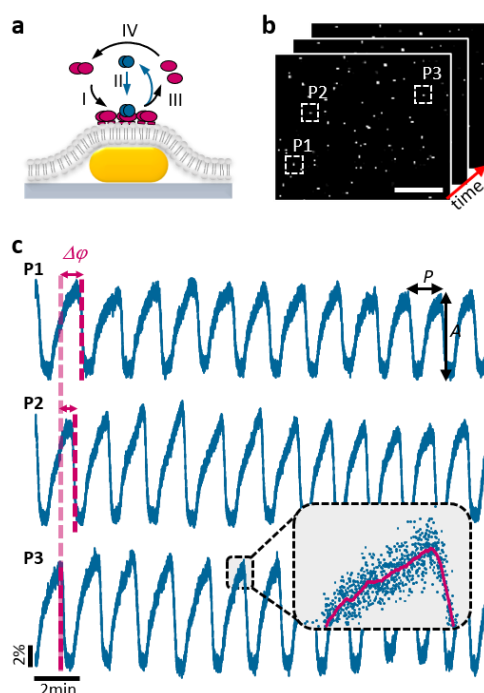


Figure 4.2: Time traces of Min coverage fluctuations at different locations. **a)** Schematic representation of the protein oscillations on top of the gold nanosensors. In step I, the protein MinD (pink) attaches to the lipid membrane. MinE (blue) is then recruited by membrane areas rich in MinD (step II). During step III, both proteins detach from the lipid membrane and MinD is released. Step IV involves the recycling of the proteins to start the cycle again. **b)** A small part of the field of view showing some nanoparticles' light scattering (scalebar 20 μm). Such images are recorded repeatedly to extract the intensity of each particle as a function of time. **c)** Traces of the relative intensity variation for three different nanoparticles as a function of time (inset depicts zoom-in, blue dots represent the original data recorded every 30 ms, the red line is the trend averaged over 100 points). From these time traces, we determine the fluctuation amplitude A , the period P , and the phase $\Delta\phi$ (pink dashed lines). This phase $\Delta\phi$ depends on the spatial location of the particle.

The time-traces for the scattering intensity of each particle show the regular oscillatory wave-pattern characteristic for Min waves. We present a 20-minute section of those time-traces in Figure 4.2c for three representative particles (out of several hundred). To compare different time-traces, we extract the period P , phase $\Delta\phi$, and oscillation amplitude A over a timespan covering a few oscillations (cf. Appendix Chapter C for details). Whereas the periods P vary by less than 5% between nanoparticles (Appendix Figure C.2a), their phase $\Delta\phi$ is clearly different and depends on the spatial location of the particle. The oscillation amplitude A is slightly different from particle to particle, which is

mainly caused by the large distribution of the individual plasmon resonance wavelengths of the particles (Appendix Figure C.2b). For the following analysis of spatial variations, we therefore normalized each nanoparticle's time-trace to values between 0 and 1 and refer to these data as *normalized intensity*. The normalized intensity is proportional to the surface coverage of Min proteins at the location of the nanoparticle.

Visualization of measured data. To see how the normalized intensity and the oscillation phase vary with nanoparticle position within the field of view, we first looked at an image where we color-coded the normalized intensity for each particle (Figure 4.3a). Due to the random distribution of the nanoparticle sensors and their sparse density, the visual impression of the pattern is not ideal. However, when we interpolate the data using a two-dimensional bilinear regression, we obtain a realistic image of the molecular interactions (Figure 4.3b) that resembles closely the patterns observed before on fluorescently labeled proteins.²¹ Repeating this procedure for every point in time, we acquire a movie of the protein coverage. In this movie (see the downloading link in the Appendix Chapter C), we clearly see ‘protein waves’ travelling over the surface with a spatial wavelength in the order of 50 μm . Figure 4.3c and Figure 4.3d depict snapshots from this movie at times T shifted by half a period ($P/2$) and one period P relative to the snapshot in Figure 4.3b. As expected, the pattern in Figure 4.3d is identical to Figure 4.3b and the image in Figure 4.3c is exactly inverted.

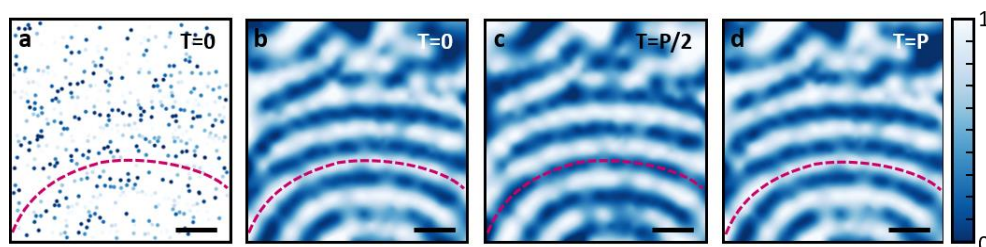


Figure 4.3: Spatial reconstruction. **a)** The normalized intensity of hundreds of single nanoparticles shown color-coded (scale on the right) for one moment in time. This normalized intensity is proportional to the protein's surface-density. **b)** By interpolating between points, we reconstitute an image of the protein coverage at this point in time ($T=0$). **c)** At $T=P/2$, half a period P later, the pattern has reversed: previously low protein density areas are now at high coverage (dashed pink line) and vice versa. **d)** Half a period later, the original distribution of coverage has recovered. The scalebar is 50 μm in all images.

Currently, we can measure up to 3000 nanoparticles in our field of view (266 x 266 μm), providing an average interparticle distance of around 5 μm . In principle, we could improve the number of particles using regular nanoparticle arrays. However, the need to optically separate particles limit the lateral resolution of i-nSPR to values close to confocal fluorescence microscopy. The depth resolution of i-nSPR is very high, in the order of a few nanometers, which is useful for providing insights into the vertical arrangement geometry of molecular assemblies.¹⁴ The time resolution of i-nSPR is mostly determined by the speed of the camera, which is at least as good as wide field-fluorescence

microscopy – with somewhat higher light intensities. Compared to high-speed AFM,^{6,7} i-nSPR provides less spatial resolution but is able to visualize much larger areas with comparatively little technical effort.

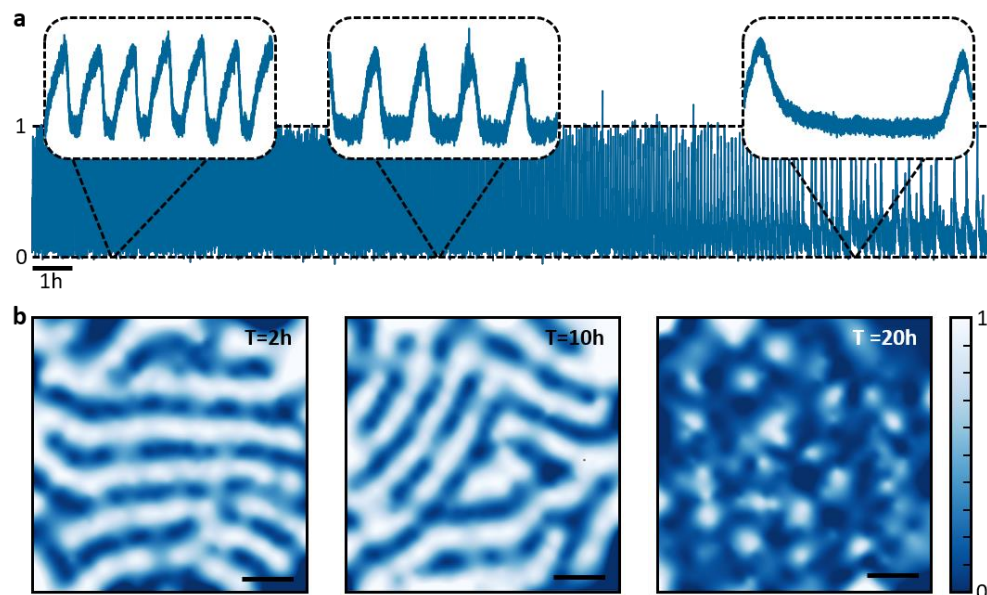


Figure 4.4. Long observation time possible. a) The normalized scattering intensity of a single gold nanoparticle as a function of time (blue solid line). We measured the protein coverage fluctuations with a temporal resolution of 30 ms for 24 hours. The insets show the oscillation behavior for 10 min intervals at 2 hours, 10 hours and 20 hours, respectively. The oscillation period clearly changes over time. b) Snap shots of the spatial patterns at the three different time intervals corresponding to the insets in panel a (scalebar 50 μm) showing a loss in spatial coherence at later times.

Long observations. Besides the simplicity and the lack of a need to fluorescently label the molecule of interest, a main benefit of i-nSPR is the unlimited observation time. In contrast to fluorescent dyes, the plasmonic nanoparticles (gold nanorods) are photostable for an indefinite period of time.^{20,22,23} The experimental challenges mainly comprise handling large datasets and ensuring setup stability. To test the potential for such long-term observations, we measured the Min dynamics for 24 hours with 30 ms time resolution. Figure 4.4a shows the time-trace for a single nanosensor, where drift has been removed for clarity (cf. Appendix Figure C.1). Interestingly, the oscillation behavior changes dramatically over time (Figure 4.4a insets). The period between oscillations increases and the waveform changes from a zig-zag pattern to sparsely spaced blips. Another way to observe these trends is by listening to the characteristic chirp such a dataset produces when converted to a soundwave (see the downloading link in the Appendix Chapter C).

When we look at the spatial pattern as a function of time (Figure 4.4b), we observe a clear transition from regular waves in the beginning, over a more irregular wave-pattern to a loss of spatial coherence at later times. This loss of coherence is a clear sign of a transition from a correlated to a chaotic oscillation pattern that was predicted theoretically.²⁴ Surprisingly, these changes of

oscillation period, waveform and patterns seem to be a characteristic feature of the membrane composition. Our original experiment was recorded on a supported lipid membrane constructed from *E. coli* polar extract. When we performed similar experiments on artificial membranes containing cardiolipin, which is known to influence the degree of MinD adhesion to membranes,¹⁴ the periods were slower at the beginning and showed a more rectangular wave-pattern (see Appendix Figure C.3, C.4 and C.5). An artificial membrane containing no cardiolipin shows even different behavior with a more or less constant period. We initially thought that the slow changes in period in the first experiment were caused by a depletion of ATP, but this seems to be inconsistent with the last observation on the membrane lacking cardiolipin, where the period remained stable. Our hypothesis is that Min waves might organize the lipid membranes towards spatially separated areas of different lipid composition. Although there are previous hints towards such a mechanism,²⁵⁻²⁷ it is very difficult to proof this hypothesis from a limited parameter study given the highly interconnected nature of the Min protein system.

4.3 Conclusion

We can already conclude, however, that the i-nSPR technique is a powerful tool to study the spatial dynamics of interacting macromolecules without the need to label one of the interaction partners. The spatial resolution is in the order of a few micrometers, the temporal-resolution in the tens of ms regime. The method relies on simple intensity monitoring of plasmonic nanoparticles illuminated with an LED light source in a conventional dark-field optical light microscope in transmission mode. Besides the simplicity of the setup and the lack of a need for molecular labeling steps, a strong advantage is the indefinite stability of the plasmonic sensors. This stability allows to follow the interactions for extended periods of time, in our case over 24 hours. The lack of a need to label the molecules is not only saving time and effort but also helps to avoid measurement artifacts caused by changing binding affinities or diffusion rates. An additional advantage of nanoSPR is the very small sensing depth in the tens of nanometers range, which is well adapted to molecular dimensions and allows to resolve molecular interactions more accurately. We have shown here how i-nSPR is able to measure MinDE oscillations on top of different types of supported lipid bilayers. These observations already show interesting and previously inaccessible features such as a slow transition from periodic to chaotic behavior. It is straight-forward to combine i-nSPR with non-imaging nanoSPR to obtain binding constants^{13,19} and molecular distances,^{20,28,29} which makes i-nSPR a versatile technique for biophysical studies of macromolecular interactions.

4.4 Author Contributions

S.C. initiated and designed the research under the guidance of R. A-G. and C.S.. S.C. developed the measurement setup and the analysis software. S.C. performed and evaluated the experiments. W.Y and K.K helped to interpret the data. K.W.

was involved in the setup development and generated the movies. S.C. created the audio files. F.S. was involved in the software development. The manuscript text was written by S.C., R. A-G and C.S.. S.C. prepared all figures.

4.5 Acknowledgement

The purified Min proteins were provided by the group of Petra Schwille. We thank Jacob Halatek for insightful discussions on the Min dynamics and its transitions from regular to chaotic behavior. Eva Wächtersbach provided technical assistance. Kaspar König initiated the sound representation of our data.

4.6 Bibliography

1. Ramm, B.; Heermann, T.; Schwille, P. The E. coli MinCDE System in the Regulation of Protein Patterns and Gradients. *Cell. Mol. Life Sci.* **2019**, *76*, 4245-4273.
2. Frey, E.; Halatek, J.; Kretschmer, S.; Schwille, P. Protein Pattern Formation. arXiv:1801.01365v2.
3. Thalmeier, D.; Halatek, J.; Frey, E. Geometry-induced Protein Pattern Formation. *Proc. Natl. Acad. Sci. USA.* **2016**, *113*, 548-553.
4. Moerner, W. E. Single-Molecule Spectroscopy, Imaging, and Photocontrol: Foundation for Super-Resolution Microscopy (Nobel Lecture). *Angew. Chem. Int. Ed.* **2015**, *54*, 8067-8093.
5. Yao, Z.; Carballido-López, R. Fluorescence Imaging for Bacterial Cell Biology: From Localization to Dynamics, From Ensembles to Single Molecules. *Ann. Rev. Microbiol.* **2014**, *68*, 459-476.
6. Ando, T.; Uchihashi, T.; Kodera, N. High-Speed AFM and Applications to Biomolecular Systems. *Ann. Rev. Biophys.* **2013**, *42*, 393-414.
7. Miyagi, A.; Ramm, B.; Schwille, P.; Scheuring, S. High-Speed Atomic Force Microscopy Reveals the Inner Workings of the MinDE Protein Oscillator. *Nano Lett.* **2018**, *18*, 288-296.
8. Lambertz, C.; Martos, A.; Henkel, A.; Neiser, A.; Kliesch, T-T.; Janshoff, A.; Schwille, P.; Sönnichsen, C. Single Particle Plasmon Sensors as Label-Free Technique to Monitor MinDE Protein Wave Propagation on Membranes. *Nano Lett.* **2016**, *16*, 3540-3544.
9. Zhang, Y.; Armstrong, M. J.; Bassir Kazeruni, N. M.; Hess, H. Aldolase Does Not Show Enhanced Diffusion in Dynamic Light Scattering Experiments. *Nano Lett.* **2018**, *18*, 8025-8029.
10. Dimitriadis, E. K.; Horkay, F.; Maresca, J.; Kachar, B.; Chadwick, R. S. Determination of Elastic Moduli of Thin Layers of Soft Material Using the Atomic Force Microscope. *Biophys. J.* **2002**, *82*, 2798-2810.
11. Butt, H. J.; Brunero, C.; Michael, K. Force Measurements with the Atomic Force Microscope: Technique, Interpretation and Applications. *Surf. Sci. Rep.* **2005**, *59*, 1-152.

12. Wang, W.; Foley, K.; Shan, X.; Wang, S.; Eaton, S.; Nagaraj, V. J.; Wiktor, P.; Patel, U.; Tao, N. Single cells and intracellular processes studied by a plasmonic-based electrochemical impedance microscopy. *Nature Chem.* **2011**, *3*, 249–255.
13. Ahijado-Guzmán, R.; Prasad, J.; Rosman, C.; Henkel, A.; Tome, L.; Schneider, D.; Rivas, G.; Sönnichsen, C. Plasmonic Nanosensors for Simultaneous Quantification of Multiple Protein–Protein Binding Affinities. *Nano Lett.* **2014**, *14*, 5528–5532.
14. Ye, W.; Celiksoy, S.; Jakab, A.; Khmelinskaia, A.; Heermann, T.; Raso, A.; Wegner, S. W.; Rivas, G.; Schwille, P.; Ahijado-Guzmán, R.; Sönnichsen, C. Plasmonic Nanosensors Reveal a Height Dependence of MinDE Protein Oscillations on Membrane Features. *J. Am. Chem. Soc.* **2018**, *140*, 17901–17906.
15. Ament, I.; Prasad, J.; Henkel, A.; Schmachtel, S.; Sönnichsen, C. Single Unlabeled Protein Detection on Individual Plasmonic Nanoparticles. *Nano Lett.* **2012**, *12*, 1092–1095.
16. Zijlstra, P.; Paulo, P. M. R.; Orrit, M. Optical Detection of Single Non-Absorbing Molecules Using the Surface Plasmon Resonance of Gold Nanorod. *Nat. Nanotechnol.* **2012**, *7*, 379–382.
17. Beuwer, M. A.; Prins, M. W. J.; Zijlstra, P. Stochastic Protein Interactions Monitored by Hundreds of Single-Molecule Plasmonic Biosensors. *Nano Lett.* **2015**, *15*, 3507–3511.
18. Taylor, A. B.; Zijlstra, P. Single-Molecule Plasmon Sensing: Current Status and Future Prospects. *ACS Sens.* **2017**, *2*, 1103–1122.
19. Ahijado-Guzmán, R.; Menten, J.; Prasad, J.; Lambertz, C.; Rivas, G.; Sönnichsen, C. Plasmonic Nanosensors for the Determination of Drug Effectiveness on Membrane Receptors. *ACS Appl. Mater. Interfaces* **2017**, *9*, 218–223.
20. Ye, W.; Götz, M.; Celiksoy, S.; Tüting, L.; Ratzke, C.; Prasad, J.; Ricken, J.; Wegner, S. W.; Ahijado-Guzmán, R.; Hugel, T.; Sönnichsen, C. Conformational Dynamics of a Single Protein Monitored for 24 h at Video Rate. *Nano Lett.* **2018**, *18*, 6633–6637.
21. Loose, M.; Fischer-Friedrich, E.; Ries, J.; Kruse, K.; Schwille, P. Spatial Regulators for Bacterial Cell Division Self-organize into Surface Waves *in vitro*. *Science* **2008**, *320*, 789–792.
22. Hartland, G. V. Optical Studies of Dynamics in Noble Metal Nanostructures. *Chem. Rev.* **2011**, *111*, 3858–3887.
23. Willets, K. A.; Van Duyne, R. P. Localized Surface Plasmon Resonance Spectroscopy and Sensing. *Annu. Rev. Phys. Chem.* **2007**, *58*, 267–97.
24. Halatek, J.; Frey, E. Rethinking Pattern Formation in Reaction-Diffusion Systems. *Nat. Phys.* **2018**, *14*, 507–514.

25. Myleykovskaya, E.; Fishov, I.; Fu, X.; Corbin, B. D.; Margolin, W.; Dowhan, W. Effects of Phospholipid Composition on MinD-membrane Interactions *in vitro* and *in vivo*. *J. Biol. Chem.* **2003**, *278*, 22193–22198.
26. Renner, L. D.; Weibel, D. B. Cardiolipin Microdomains Localize to Negatively Curved regions of *Escherichia coli* Membranes. *Proc. Natl. Acad. Sci. USA*, **2011**, *108*, 6264–6269.
27. Renner, L. D.; Weibel, D. B. MinD and MinE Interact with Anionic Phospholipids and Regulate Division Plane Formation in *Escherichia coli*. *J. Biol. Chem.* **2012**, *287*, 38835–38844.
28. Visser, E. W. A.; Horáček, M.; Zijlstra, P. Plasmon Rulers as a Probe for Real-Time Microsecond Conformational Dynamics of Single Molecules. *Nano Lett.* **2018**, *18*, 7927-7934.
29. Sönnichsen, C.; Reinhard, B. M.; Liphardt, J.; Alivisatos, A. P. A Molecular Ruler Based on Plasmon Coupling of Single Gold and Silver Nanoparticles. *Nat. Biotech.* **2005**, *3*, 741-745.

BEYOND PLASMONICS

Single Out-of-Resonance Dielectric Nanoparticles as Molecular Sensors

Sirin Celiksoy, Weixiang Ye, Rubén Ahijado-Guzmán* and Carsten Sönnichsen*

*Corresponding Authors

A version of this chapter is published in ACS sensors.

Light scattering from single nanoparticles and nanostructures is a commonly used readout method for nanosensors. Increasing the spectral sensitivity of resonant nanosensors to changes in their local surrounding has been the focus of many studies. Switching from spectral to intensity monitoring allows to investigate non-resonant or out-of-resonance dielectric nanoparticles. Here, we systematically compared such dielectric silica nanoparticles with plasmonic gold nanorods by deriving analytical expressions and by performing experiments. The experiments show a similar sensitivity for the detection of an adsorbate layer for both particle types, which is in good agreement with theory. The flat spectral response of dielectric silica nanoparticles simplifies the choice of illumination wavelength. Furthermore, such dielectric nanoparticles can be made from many oxides, polymers and even biological assemblies, broadening the choice of materials for the nanosensor.

5.1 Introduction

The small size and the high light scattering cross section of plasmonic nanoparticles have established them as highly sensitive point-like sensors within the fields of nano- and biotechnology.¹ These plasmonic particle-based nanosensors, mainly made from gold, have been used to study biological macromolecules and their interactions with up to single-molecule sensitivity.² Recently, alternative sensing platforms made from high refractive index

dielectric particles have been demonstrated.³⁻⁵ As resonance phenomena, such optical nanosensors use Fano resonances⁶⁻⁷, whispering gallery modes (WGM)⁸⁻⁹ or bound states in the continuum (BIC) of a metamaterial¹⁰. Local changes to the sensor's surrounding are usually monitored spectroscopically *via* their effect on the resonance wavelength. Monitoring the scattering efficiency or intensity at a single wavelength instead simplifies the setup, making it cost effective, and faster.¹¹⁻¹² Single wavelength intensity monitoring eliminates the need for a resonance, something that has not been appreciated much in literature so far. Only the detection of small dielectric nanoparticles (proteins) purely on the basis of their scattering has been demonstrated.¹³⁻¹⁵

In this work, we go beyond detection and use such dielectric nanoparticles as individual nanosensors for the binding of molecules to their surface. We systematically compared the sensing performance of dielectric silica nanoparticles with that of plasmonic gold nanorods, by deriving analytical expressions and by performing experiments. Firstly, we monitored the response to refractive index changes, secondly the sensitivity to the adsorption of polyelectrolyte layers and thirdly the response to an oscillating surface coverage. The experiments show a similar sensitivity for the detection of an adsorbate layer for both nanoparticle types, which is in good agreement with theory. The flat spectral response of dielectric nanoparticles simplifies the choice of illumination wavelength. Furthermore, such dielectric nanoparticles can be made from many oxides, polymers and even biological assemblies, broadening the choice of materials for the nanosensor. A broader choice of nanosensor material allows to take advantage of many chemical functionalization strategies already developed in different context. For example, silica nanoparticles are available with specific tags to attach molecules (e.g. proteins or DNA) or coated with lipid membranes.¹⁶⁻¹⁹ Non-resonant or out-of-resonance* dielectric nanoparticles are therefore very attractive as an alternative platform for single particle nanosensors.

*We use the term 'non-resonant' in the sense that there is no resonance within the visible and NIR spectral region. It is clear that any particle shows a characteristic resonance at some frequencies due to vibrational or electronic transitions.

5.2 Results and Discussion

Measurement Principle. To compare the performance of plasmonic and dielectric nanoparticles, we used a single particle spectroscopy setup with dark-field illumination. A dark-field condenser directs the illumination light at oblique angles, so that only the light scattered by the nanoparticles enters the objective (Figure 5.1a). We immobilized nanoparticles randomly on the bottom of a microfluidic flow cell, with a spacing that is large enough to identify individual nanoparticles. A camera recorded the scattering intensity of all individual nanoparticles within the field of view (cf. Appendix Chapter D for details). Plasmonic nanoparticles predominantly scatter light at their plasmon resonance wavelength λ_{res} whereas dielectric silica nanoparticles scatter light at all wavelengths. Therefore, dielectric nanoparticles appear white and the gold nanorods used here appear red under white light illumination (Figure 5.1b). Plasmonic nanoparticles react to an increase in the polarizability of their immediate surrounding (caused, for example, by the binding of an analyte) with

a red-shift of the plasmon resonance wavelength $\Delta\lambda_{\text{res}}$ and an overall increase in scattering efficiency (Figure 5.1c, inset left). Dielectric silica nanoparticles respond with a uniform increase at all wavelengths (Figure 5.1c, inset right). Here, we monitor the scattering efficiency at a fixed detection wavelength λ_D (indicated by the gray shading in Figure 5.1c, inset), which makes it possible to compare the results from the two types of nanoparticles within the same experiment.

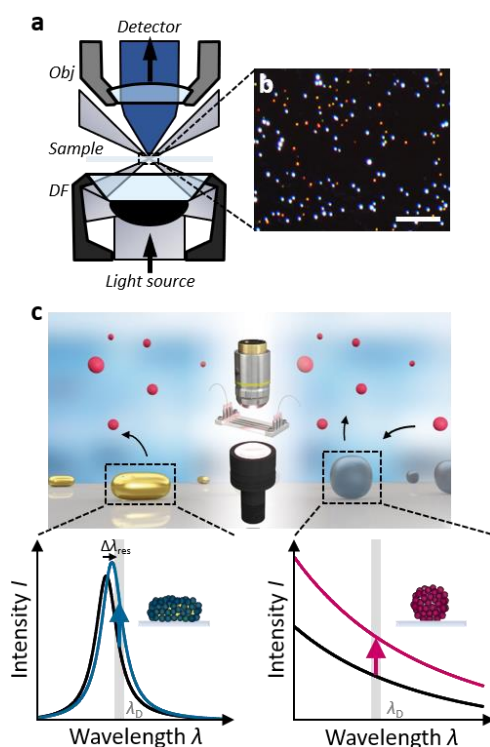


Figure 5.1: Measurement principle. **a)** Schematics of a dark-field microscope setup. The illumination light enters a dark-field condenser (*DF*) from below. The dark-field condenser directs the light (gray) at oblique angles so that only light scattered by nanoparticles (blue) enters the objective (*Obj*) and is directed to the detector. **b)** Real-color dark-field image of a mixture of gold nanorods (red spots) and silica nanospheres (white spots) under white light illumination. Scale bar corresponds to 50 μm . **c)** Sketch of the sensing principle of plasmonic and dielectric nanosensors. Both sensor types are immobilized on a glass substrate with a spacing large enough to detect individual nanoparticles under dark-field illumination. The left inset shows a schematic representation of single gold nanorod spectra before (black) and after (blue) the binding of an analyte to the nanoparticle surface: The plasmon resonance wavelength shifts by $\Delta\lambda_{\text{res}}$ and the intensity increases by ΔI (blue arrow) at the detection wavelength λ_D (gray area). The right inset depicts a schematic illustration of silica nanoparticle scattering spectra before (black) and after (pink) analyte binding. Artwork in top image of panel c) courtesy of Felix Schlapp.

Since nanoparticles have a size and shape distribution, their scattering efficiency varies from particle to particle. Therefore, it is useful to discuss the relative scattering intensity change ΔI_{rel} . This is the scattering intensity change ΔI induced by a given process around the nanoparticles (e.g. analyte binding), relative to the initial scattering intensity I_0 of the same particle: $\Delta I_{\text{rel}} = \Delta I / I_0$. The choice of the detection wavelength is important, especially for the

plasmonic nanoparticles. We choose a detection wavelength λ_D where the relative change in scattering intensity is largest, i. e. at the red side of the plasmon resonance wavelength (see Figure 5.1c, inset left).

Response to changes of the close vicinity. To compare the sensitivity of different nanosensors, it is common practice to measure the change induced by a variation of the bulk dielectric constant in the surrounding solvent, Δn .²⁰⁻²¹ It is important to switch back and forth between different solutions (here, glucose at different concentrations in water) in order to avoid irreversible changes to the nanosensor itself, for example surface charge or removal of surfactants. Plasmonic nanoparticles show a linear response ΔI_{rel} to refractive index changes Δn (Figure 2a, blue dots). This allows us to define a sensitivity parameter $S_I = dI_{\text{rel}}/dn$, the intensity bulk sensitivity. Silica nanoparticles show a similar behavior (Figure 5.2a, pink dots), but with a negative slope. Whereas the signal of plasmonic nanoparticles depends strongly on particle properties such as size, aspect ratio, or surface quality,^{20, 22} the silica nanoparticles show a size-independent intensity response (Figure 5.2a, pink dots, crosses and squares).

The Clausius-Mossotti relationship²³ describes how the light scattering efficiency of small particles depends on the light frequency or wavelength. We deduce that the intensity bulk sensitivity of dielectric nanoparticles follows $S_I = 2/(n - n_p)$ (cf. Appendix Chapter D) where n and n_p correspond to the medium and particle refractive index, respectively. The experimental values and the theoretical predictions agree reasonably well (Table 5.1). There is a singularity if the medium and particle refractive index, n and n_p , match at which point, the silica nanoparticles would become invisible (cf. Appendix Chapter D). In other words, the scattering efficiency is zero. (Note: it is also important to consider the measurement noise (which depends on the absolute scattering intensity) and not only the sensitivity. We will discuss the noise further below).

It is more difficult to find an analytical expression for the intensity bulk sensitivity of plasmonic nanoparticles because of the imaginary part of the metals' dielectric function. However, we addressed this in another publication²⁴ and found the relationship: $S_I = \frac{8}{n} + \frac{-4S\lambda}{\lambda_{\text{res}}} + \frac{-2S\lambda}{\epsilon_2} \frac{\partial \epsilon_2}{\partial \lambda_{\text{res}}} + \frac{2S\lambda}{r}$. Again, experimental values and theoretical predictions for S_I of plasmonic nanoparticles agree reasonably well (Table 5.1). The absolute value for the intensity bulk sensitivity of dielectric nanoparticles is comparable to that of the plasmonic nanoparticles, which is interesting in the context of many previous attempts to increase plasmonic sensitivities that have resulted in comparatively moderate improvements.²⁵

So far, we have discussed the response of nanoparticles to changes in the refractive index of the complete environment, i. e. the bulk refractive index sensitivity. However, most applications for nanoparticle sensors, rely on particles functionalized with receptors for the recognition of specific analytes. The observed signal is, in such applications, the response to a *layer* of adsorbates. This layer sensitivity is, in general, not identical to the intensity bulk sensitivity S_I . To distinguish both properties, we use the symbol \mathcal{S} (S cedilla, pronounced *Sb* like

in shoe) for the intensity layer or surface sensitivity, defined as $\mathcal{S}_I = \lim_{l \rightarrow 0} dI_{\text{rel}}/dl$. We believe that the intensity surface sensitivity \mathcal{S}_I has the potential to be one of the most relevant parameters describing the performance of single particle nanosensors with intensity readout, because it predicts the change in signal caused by the adsorption of a layer to the sensor surface. Experimentally, we measure \mathcal{S}_I by monitoring the change induced by increasingly thick coatings using the Layer-by-Layer (*LbL*) deposition method.²⁶⁻²⁷ We used one batch of gold nanorods and three batches of silica nanoparticles with mean diameters of 100 nm, 200 nm, and 300 nm, chosen to yield scattering intensities smaller, about equal to, and larger than the gold nanorods.

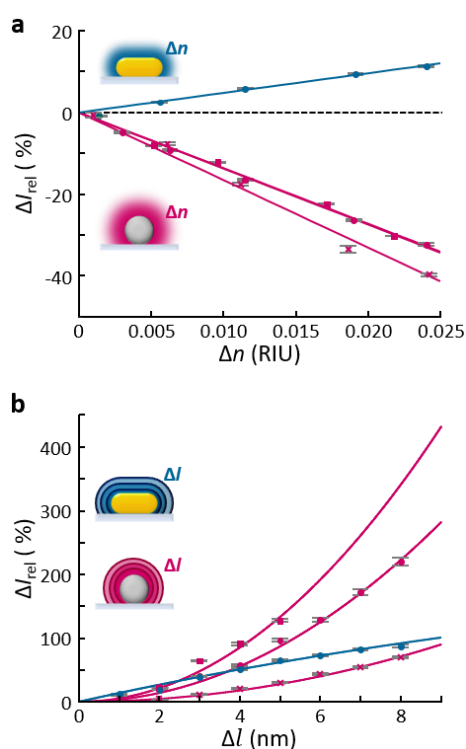


Figure 5.2: Response to refractive index changes and adsorbate layers. a) The relative intensity change ΔI_{rel} for gold nanorods (blue dots) and silica nanoparticles with diameters of 100 nm (pink squares), 200 nm (pink dots) and 300 nm (pink crosses) with respect to an increasing refractive index change Δn of the surrounding medium. The experimental values are the median of many single nanoparticles with error bars corresponding to the standard error. **b)** Increase of the relative intensity ΔI_{rel} after the deposition of polyelectrolyte layers Δl for gold nanorods (blue dots) and silica nanoparticles with diameters of 100 nm (pink squares), 200 nm (pink dots) and 300 nm (pink crosses). The data points depict the median of many single nanoparticles and the error bars the standard error.

Figure 5.2b shows the relative intensity change for both types of nanoparticles after each deposition step. The response of the plasmonic nanosensors (Figure 5.2b, blue dots) saturates when the layer fills the entire sensing volume. In contrast, the relative scattering intensity of the dielectric silica nanoparticles does not saturate. This behavior can be understood as an effective increase of the particle diameter, assuming a similar refractive index of the layer and the silica nanoparticle. The Clausius-Mossotti relationship predicts a

scattering intensity I proportional to the square of the particle volume $I \sim V^2$ resulting in $\mathcal{S}_I = 6/r$ (cf. Appendix Chapter D). The experimental values agree with this calculation quite accurately. (Table 5.1). The intensity surface sensitivity of plasmonic nanoparticles is related to their intensity bulk sensitivity S_I by $\mathcal{S}_I = S_I \Delta n / d_s^{24}$, where d_s is the sensing distance, defined as the layer thickness that gives 1/e of the response of a bulk dielectric constant change.²⁸ Again, the theoretical model and experimental data are in good agreement (Table 5.1).

Table 5. 1: Comparison between experimental data and theoretical predictions (in gray) for S_I and \mathcal{S}_I .

	S_I (RIU ⁻¹)	$\mathcal{S}_I / \Delta n$ (nm ⁻¹ RIU ⁻¹)
gold	17.8	1.7
	19.7* ± 3.0	1.9 ± 0.2
silica ₁₀₀	-16.7	0.92
	-16.7 ± 2.5	0.54 ± 0.08
silica ₂₀₀	-16.7	0.52
	-13.6 ± 2.0	0.32 ± 0.05
silica ₃₀₀	-16.7	0.36
	-13.8 ± 2.1	0.10 ± 0.02

*calculated from a layer experiment (details in the supporting information).
The experimental error is estimated as 15% from the uncertainties of the input values.

Signal-to-noise ratio of silica and gold nanoparticles. As stated before, the surface sensitivity \mathcal{S}_I is the most important factor describing nanoparticle sensor performance. The other factor to consider is the noise level. Measurement noise is, however, very difficult to treat theoretically because it is determined by many specific details of the setup and the experimental procedure, such as the temperature stability of the room. In our example, it is possible to measure the two types of nanoparticles within the same experiment, which makes the fairest comparison possible. We measured the noise level for each nanoparticle type by recording the scattering intensity of the same nanoparticle as a function of time with a time-resolution of 50 milliseconds (Appendix Figure D.3a). The standard deviation over 1 minute of this ‘time trace’ is a good measure of the overall noise level and shows a trend that is well described by assuming photon statistics for the leading noise source (Appendix Figure D.3b). Figure 5.3a shows the signal for a 1 nm layer normalized to this measured noise level for the three sizes of silica nanoparticles (pink bars) and the gold nanorods (blue bar). The silica nanoparticles show a signal-to-noise ratio (S/N_{layer}) in the same order of magnitude as the gold nanorods. The differences should not be overestimated because the values shown in Figure 5.3a depend on the thickness of the adsorbate layer. Slightly thicker layers (e.g. 5 nm) reverse the trend, with plasmonic nanoparticles performing slightly worse (Appendix Figure D.7). In principle, these results indicate the possibility of tuning particle size and type.

However, we expect that other considerations, such as, the ease of surface modification, will be more important when choosing the type of particle for a given application.

Another parameter for the comparison of dielectric and plasmonic nanoparticles is their strongly differing surface area. For single-molecule detection, which is a promising and exciting application for nanosensors², we need to take into account how many molecules form a layer. In general, the number of attached molecules N in a layer is proportional to the layer's volume V_L ($N \sim V_L$), which scales for small changes of the layer thickness Δl with the surface area A_p of the particles as: $V_L \approx A_p \cdot \Delta l$. Therefore, ignoring the position-dependent sensitivity of gold nanorods²⁹, we can estimate the signal-to-noise level for single-molecule detection ($S/N_{\text{single molecule}}$) by normalizing the data from Figure 5.3a to the available surface area of the respective nanoparticles. The results show a strong advantage of gold nanorods over silica nanospheres with $S/N_{\text{single molecule}}$ values larger by about one order of magnitude (Figure 5.3b). Single-molecule detection is better with gold nanorods due to their much smaller size compared to silica nanoparticles with the same scattering intensity.

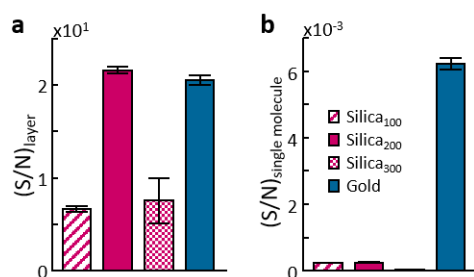


Figure 5.3: Signal-to-Noise Ratio. **a)** Comparison of signal-to-noise ratios $(S/N)_{\text{layer}}$ for the adsorption of a 1 nm layer on gold nanorods (blue) and silica nanoparticles (pink) (legend in panel b). **b)** The signal-to-noise ratio for single molecules $(S/N)_{\text{single molecule}}$, calculated by normalizing $(S/N)_{\text{layer}}$ to the sensor's surface area.

Sensing with silica and gold nanoparticles. The systematic comparison of signal and noise levels for different analytes and nanoparticles presented above predicts that silica and gold nanoparticles should perform similarly with regards to the observation of coverage changes. To verify this prediction, we performed an experiment with both particle types simultaneously on the supporting glass slide (Figure 5.1b and 5.1c) and compared their signal and noise levels. As a convenient system to induce layer changes, we used the well-known dynamic Min protein system. The Min proteins attach and detach from a lipid membrane in a synchronized way resulting in periodic coverage changes that are caused by a layer of Min proteins building up and then rapidly detaching.³⁰ In earlier experiments using gold nanorods, we have shown that it is possible to monitor this periodic attachment and detachment process on the lipid membrane spanning the nanoparticles.²⁸

To characterize the noise level N , we first recorded a 'baseline' (Figure 5.4a left) of the lipid membrane-covered nanoparticles in buffer. N is the standard deviation of the baseline (recorded with a time-resolution of 300 ms) over

15 min. After the addition of the Min proteins (schematically represented by the gray area in Figure 5.4a center), the typical ‘Min oscillations’ of the coverage layer are evident. Both silica and gold nanoparticles respond to these coverage changes with an oscillating scattering intensity (Figure 5.4a right). From these oscillations, we extracted the oscillation amplitude A and period P , which match well with our previous reports.²⁸ All of these values (N , A and P) were determined for all the nanoparticles in the field of view separately (Appendix Figure D.4). For the comparison of the two particle types, we used the amplitude A as the ‘signal level’ and divided this value by the noise N level obtained from the baseline. The resulting signal-to-noise ratio is approximately two times better for silica nanospheres compared to gold nanorods in this experiment (Figure 5.4b), which agrees qualitatively with the predictions for an adsorbate layer thickness of 4 to 5 nm (Appendix Figure D.7).

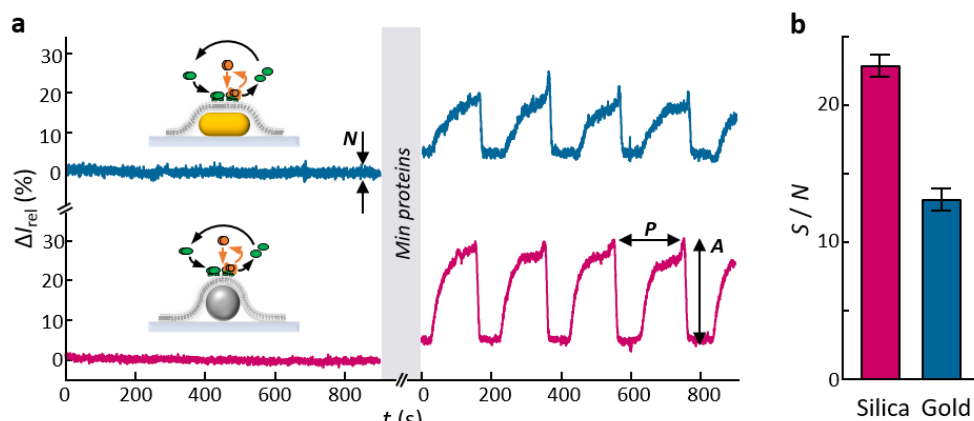


Figure 5.4: Monitoring Min waves. **a)** Baseline (left) and Min protein oscillation (right) monitored on gold nanorods (blue, top) and silica nanoparticles (pink, bottom). The noise level N is determined from the standard deviation of the baseline. After the Min proteins are added (gray area), the Min proteins periodically attach and detach (insets of the process on the left) with an oscillation amplitude A and period P . **b)** We compare the signal-to-noise (S/N) level for both particle types by dividing the amplitude A (the ‘signal’) with the noise N obtained from the baseline.

To demonstrate the use of dielectric nanoparticles as a replacement for gold nanorods, we also performed a typical ‘NanoSPR’ titration measurement determining binding affinities (K_D values).³¹ As a test system we chose the interaction between the MinD protein and the supported lipid membrane. The experiment reveals a typical binding isotherm with a K_D value of $5.3 \mu\text{M} \pm 2.0 \mu\text{M}$ that agrees with literature reports (Appendix Figure D.5).³²

5.3 Conclusion

Both the Min wave and the titration experiment demonstrate that out-of-resonant dielectric nanoparticles, in our example silica nanospheres, are a worthwhile alternative to gold nanorods for the use as nanosensors, except for the detection of single molecules. Dielectric nanoparticles work equally well at any detection wavelength, removing the need to adjust the detection wavelength

to a given resonance position. Our experimental results show that silica nanoparticles with a diameter of 200 nm perform best in our case but the balance between signal strength and noise level could vary in a different setup. An advantage of dielectric out-of-resonance nanosensors is that they can be composed of any transparent material, for example many oxides, lipid vesicles or polymer beads. The broad choice of materials makes it more likely that the surface chemistry is already developed for a given analyte-receptor system. We believe these advantages make out-of-resonant nanoparticles especially useful for the study of biological macromolecules such as the formation of a protein corona.³³⁻³⁴

5.4 Author Contributions

S.C. and C.S. initiated and designed the research. S.C. developed the measurement setup and the analysis software. S.C. and W.Y. derived the mathematical models and interpreted the data under the guidance of C.S.. S.C. performed the experiments under the guidance of R. A-G.. The manuscript text was written with contributions by S.C. and C.S.. S.C. prepared all figures.

5.5 Acknowledgement

This work was financially supported by the ERC Grant 259640 (“SingleSense”). W.Y. was funded by the Graduate School of Excellence Materials Science in Mainz (Grant GSC 266). We thank Eva Wächtersbach and Karl Wandner for the assistance with experiments and software development. We thank Petra Schwille’s group for providing purified Min proteins. We thank Felix Schlapp for preparing the artwork of the table of contents (TOC) image and the top panel of Figure 1c.

5.6 Bibliography

1. Anker, J. N.; Hall, W. P.; Lyandres, O.; Shah, N. C.; Zhao, J.; Van Duyne, R. P. Biosensing with Plasmonic Nanosensors. *Nat. Mater.* **2008**, *7*, 442-453.
2. Taylor, A. B.; Zijlstra, P. Single-Molecule Plasmon Sensing: Current Status and Future Prospects. *ACS Sensors* **2017**, *2*, 1103-1122.
3. Zhu, X.; Imran Hossain, G. M.; George, M.; Farhang, A.; Cicek, A.; Yanik, A. A. Beyond Noble Metals: High Q-Factor Aluminum Nanoplasmonics. *ACS Photonics* **2020**, *7*, 416-424.
4. Yan, J.; Liu, P.; Lin, Z.; Yang, G. New Type High-Index Dielectric Nanosensors Based on the Scattering Intensity Shift. *Nanoscale* **2016**, *8*, 5996-6007.
5. Yavas, O.; Svedendahl, M.; Quidant, R. Unravelling the Role of Electric and Magnetic Dipoles in Biosensing with Si Nanoresonators. *ACS Nano* **2019**, *13*, 4582-4588.
6. Wu, C.; Khanikaev, A. B.; Adato, R.; Arju, N.; Yanik, A. A.; Altug, H.; Shvets, G. Fano-resonant Asymmetric Metamaterials for Ultrasensitive

- Spectroscopy and Identification of Molecular Monolayers. *Nat. Mater.* **2012**, *11*, 69-75.
7. Luk'yanchuk, B.; Zheludev, N. I.; Maier, S. A.; Halas, N. J.; Nordlander, P.; Giessen, H.; Chong, C. T. The Fano Resonance in Plasmonic Nanostructures and Metamaterials. *Nat. Mater.* **2010**, *9*, 707-715.
 8. Frustaci, S.; Vollmer, F. Whispering-Gallery Mode (WGM) Sensors: Review of Established and WGM-based Techniques to Study Protein Conformational Dynamics. *Current Opinion in Chemical Biology* **2019**, *51*, 66-73.
 9. Vollmer, F.; Arnold, S. Whispering-Gallery-Mode Biosensing: Label-Free Detection Down to Single Molecules. *Nat. Methods* **2008**, *5*, 591-596.
 10. Romano, S.; Zito, G.; Torino, S.; Calafiore, G.; Penzo, E.; Coppola, G.; Cabrini, S.; Rendina, I.; Mocella, V. Label-Free Sensing of Ultralow-Weight Molecules with All-Dielectric Metasurfaces Supporting Bound States in the Continuum. *Photon. Res.* **2018**, *6*, 726-733.
 11. Beuwer, M. A.; Prins, M. W. J.; Zijlstra, P. Stochastic Protein Interactions Monitored by Hundreds of Single-Molecule Plasmonic Biosensors. *Nano Letters* **2015**, *15*, 3507-3511.
 12. Baaske, M. D.; Neu, P. S.; Orrit, M. Label-Free Plasmonic Detection of Untethered Nanometer-Sized Brownian Particles. *ACS Nano* **2020**, *14*, 14212-14218.
 13. Piliarik, M.; Sandoghdar, V. Direct Optical Sensing of Single Unlabelled Proteins and Super-Resolution Imaging of Their Binding Sites. *Nat. Comm.* **2014**, *5*, 4495.
 14. Liebel, M.; Hugall, J. T.; van Hulst, N. F. Ultrasensitive Label-Free Nanosensing and High-Speed Tracking of Single Proteins. *Nano Letters* **2017**, *17*, 1277-1281.
 15. Li, M.; Yuan, T.; Jiang, Y.; Sun, L.; Wei, W.; Chen, H.-Y.; Wang, W. Total Internal Reflection-Based Extinction Spectroscopy of Single Nanoparticles. *Angew. Chem. Int. Ed.* **2019**, *58*, 572-576.
 16. Qhobosheane, M.; Santra, S.; Zhang, P.; Tan, W. Biochemically Functionalized Silica Nanoparticles. *Analyst* **2001**, *126*, 1274-1278.
 17. Torney, F.; Trewyn, B.; Lin, V.; Wang, K. Mesoporous Silica Nanoparticles Deliver DNA and Chemicals into Plants. *Nat. Nanotechnol.* **2007**, *2*, 295-300.
 18. Sobrinos-Sanguino, M.; Zorrilla, S.; Monterroso, B.; Minton, A. P.; Rivas, G. Nucleotide and Receptor Density Modulate Binding of Bacterial Division FtsZ Protein to ZipA Containing Lipid-Coated Microbeads. *Sci. Rep.* **2017**, *7*, 13707.
 19. Liberman, A.; Mendez, N.; Trogler, W. C.; Kummel, A. C. Synthesis and Surface Functionalization of Silica Nanoparticles for Nanomedicine. *Surf. Sci. Rep.* **2014**, *69*, 132-158.

20. Chen, H.; Kou, X.; Yang, Z.; Ni, W.; Wang, J. Shape- and Size-Dependent Refractive Index Sensitivity of Gold Nanoparticles. *Langmuir* **2008**, *24*, 5233-5237.
21. Khan, A. U.; Zhao, S.; Liu, G. Key Parameter Controlling the Sensitivity of Plasmonic Metal Nanoparticles: Aspect Ratio. *J. Phys. Chem. C* **2016**, *120*, 19353-19364.
22. Du, C.; Yang, W.; Peng, S.; Shi, D. Optimal Geometry Parameter for Plasmonic Sensitivities of Individual Au Nanoparticle Sensors. *Phys. Chem. Chem. Phys.* **2019**, *21*, 7654-7660.
23. Jackson, J. D., *Classical electrodynamics*. Wiley: New York, 1999.
24. Celiksoy, S.; Ye, W.; Wandner, K.; Kaefer, K.; Sönnichsen, C. Intensity-based Single Particle Plasmon Sensing. *Nano Lett.* **2020**, submitted for publication.
25. Guo, L.; Jackman, J. A.; Yang, H.-H.; Chen, P.; Cho, N.-J.; Kim, D.-H. Strategies for Enhancing the Sensitivity of Plasmonic Nanosensors. *Nano Today* **2015**, *10*, 213-239.
26. Kedem, O.; Tesler, A. B.; Vaskevich, A.; Rubinstein, I. Sensitivity and Optimization of Localized Surface Plasmon Resonance Transducers. *ACS Nano* **2011**, *5*, 748-760.
27. Au - Hoang, T. B.; Au - Huang, J.; Au - Mikkelsen, M. H. Colloidal Synthesis of Nanopatch Antennas for Applications in Plasmonics and Nanophotonics. *J. Vis. Exp.* **2016**, *111*(e53876), 1-7.
28. Ye, W.; Celiksoy, S.; Jakab, A.; Khmelinskaia, A.; Heermann, T.; Raso, A.; Wegner, S. V.; Rivas, G.; Schwille, P.; Ahijado-Guzmán, R.; Sönnichsen, C. Plasmonic Nanosensors Reveal a Height Dependence of MinDE Protein Oscillations on Membrane Features. *J. Am. Chem. Soc.* **2018**, *140*, 17901-17906.
29. Beuwer, M. A.; van Hoof, B.; Zijlstra, P. Spatially Resolved Sensitivity of Single-Particle Plasmon Sensors. *J. Phys. Chem. C* **2018**, *122*, 4615-4621.
30. Loose, M.; Fischer-Friedrich, E.; Ries, J.; Kruse, K.; Schwille, P. Spatial Regulators for Bacterial Cell Division Self-Organize into Surface Waves in Vitro. *Science*, **2008**, *320*, 789-92.
31. Ahijado-Guzmán, R.; Prasad, J.; Rosman, C.; Henkel, A.; Tome, L.; Schneider, D.; Rivas, G.; Sönnichsen, C. Plasmonic Nanosensors for Simultaneous Quantification of Multiple Protein-Protein Binding Affinities. *Nano Lett.* **2014**, *14*, 5528-5532.
32. Renner, L. D.; Weibel, D. B. MinD and MinE Interact with Anionic Phospholipids and Regulate Division Plane Formation in Escherichia coli. *J. Bio.Chem.* **2012**, *287*, 38835-38844.
33. Ritz, S.; Schöttler, S.; Kotman, N.; Baier, G.; Musyanovych, A.; Kuharev, J.; Landfester, K.; Schild, H.; Jahn, O.; Tenzer, S.; Mailänder, V. Protein Corona of Nanoparticles: Distinct Proteins Regulate the Cellular Uptake. *Biomacromolecules* **2015**, *16*, 1311-1321.

34. Schöttler, S.; Becker, G.; Winzen, S.; Steinbach, T.; Mohr, K.; Landfester, K.; Mailänder, V.; Wurm, F. R. Protein Adsorption is Required for Stealth Effect of Poly(ethylene glycol)- and Poly(phosphoester)-Coated Nanocarriers. *Nat. Nanotechnol.* **2016**, *11*, 372-377.

PART III

SUMMARY

SUMMARY

The Nanobiotechnology Group has pioneered the use of single plasmonic nanoparticles as sensors for their local environment. The group and others have shown an impressive array of applications, ranging from single protein detection to the determination of affinity constants. The technique relies on measuring the light scattering spectrum of single plasmonic nanoparticles in a dark-field optical microscope. The setups available in the Nanobiotechnology Group use two different measurement methods, referred to internally as 'refinement' and 'spectral imaging'. The 'refinement' method has a fast time resolution in the millisecond range but can only measure one particle at a time. In contrast, the 'spectral imaging' method has improved the number of particles that can be measured in parallel, but at the cost of lower time resolution in the second range. This circumstance forced us to choose between time-resolution and statistics. Therefore, it was not possible to study time-resolved processes (with a time resolution below a hundred milliseconds) on many particles in parallel. This made it impossible to observe dynamic processes time and spatially resolved or address the heterogeneity of the sample under investigation. The goal of my work was to develop a new readout method for plasmonic sensing to overcome the limitation of the existing setups and, at the same time, make the setup simpler and cheaper.

To achieve this goal, I moved away from the 'classical' spectral detection of the plasmon signal and used intensity changes as a measure for binding events instead. Intensity measurements have the advantage of simplifying the entire setup, being time and spatially resolved and making it possible to utilize sensor elements without resonance (e.g., dielectric nanoparticles). In this work, I have

described my success in this direction and some of the applications, which have been possible with it.

Intensity-based plasmon sensing. In chapter 2, I addressed the question of whether it is possible to detect the intensity change occurring with a shift of the particle's scattering spectrum. In cooperation with Karl Wandner, I developed a simplified microscopy setup that allows measuring the scattering intensities of nanoparticles at a single wavelength and developed the necessary control and analysis software. I found out that the most important points for single line detection are to determine the particles' background intensity robustly and reliably and adapt the detection wavelength to the nanoparticle sample distribution. Using analyte-responsive and non-responsive nanoparticles as sensors simultaneously, I demonstrated the potential of the new measurement mode to observe analyte-specific signal changes. Only the responsive nanoparticles showed an increase in intensity after analyte interaction. That the non-responsive nanoparticles did not reveal any signal change proves that the intensity increase was not due to interfering sources, such as defocusing or impurities in the oil, but was caused by a real binding event. Indeed, the variation of intensity change within a particle sample is larger than that of resonance wavelength changes, but my new method also allows the detection of thousands of nanosensors in the field of view simultaneously, ensuring high statistics and accuracy. Compared to the conventional spectral readout method, I can now observe a multitude of sensors with a time resolution of up to 20 ms for an indefinite observation time (in principle). For the investigation of biochemical systems, this opens up completely new possibilities, e.g., observing a protein's different states over a whole day and visualizing biological processes without the need for labeling.

Theoretical background. Another aspect of my work (Chapter 3) was a theoretical understanding of the intensity change after analyte binding. It helps us to interpret the experimental data and optimize the system. Together with Weixiang Ye, I derived a simple equation based on Clausius Mossotti's formula to describe the intensity sensitivity and identify the various contributions to the overall change: Rayleigh scattering, dielectric contrast, plasmon shift, and frequency-dependent plasmon bulk damping. We found that the main contribution comes from the shift term, especially for nanosensors with resonances above 700 nm. Interestingly, this quantity is proportional to, which resembles the 'figure of merit' (FOM) known in the literature as a measure to characterize nanosensors. We also found that the intensity bulk sensitivity decreases for increasing particle volume. Therefore, it is beneficial to use the smallest nanosensors possible. Our quantity's major advantage is that it can be used to compare different nanosensors with each other, even non-plasmonic sensors, such as dielectric nanoparticles.

Label-free imaging with dark-field microscopy. The advantage of being spatially and temporally resolved at the same time enabled me to utilize plasmonic sensors to visualize dynamic biological processes for the first time (Chapter 4). To exemplify the method, called imaging-nanoSPR (i-nSPR), I used

the Min system, which is known to attach and detach from a lipid membrane periodically. This oscillation happens on the minute timescale with spatial patterns in the 10-100 μm regime, the 'Min waves'. My novel intensity-based readout method allowed me to observe the oscillation for one entire day (24 hours) instead of only for minutes to hours as usually done in other studies. Thus, I could show that the min-wave pattern changes dramatically over time, from an initially synchronized wave pattern into a chaotic arrangement until, finally, there is no min-wave pattern left. The period between the oscillation increases and the waveform changes from a zig-zag pattern to sparsely spaced blips. I found that both oscillation period and pattern depend on the membrane composition. Membranes lacking cardiolipin led to an oscillatory behavior for at least 24 hours, whereas for membranes containing cardiolipin, the period changed within 24 hours. Surprisingly, there is a correlation between the amount of cardiolipin and the increasing time of the period. A reason for it could be that Min waves might organize the lipid membranes towards spatially separated areas of different lipid compositions. However, for a clear statement, more data is required.

Beyond plasmonics. Switching from the spectral readout to the intensity-based measurement method allows using out-of-resonance dielectric nanoparticles as sensors to study molecular interactions. In chapter 5, I systematically compared the performance of this new class of sensors in dark-field microscopy with the gold nanorods conventionally used. Interestingly, the sensitivity of dielectric nanosensors to the adsorption of complete layers is of the same order of magnitude as the one of gold nanoparticles, which is also consistent with theoretical calculations. Out-of-resonance dielectric nanoparticles have the advantage of being independent of the detection wavelength, unlike gold nanoparticles, which further simplifies the intensity-based method. Such dielectric nanoparticles can be made from many oxides, polymers, and even biological compositions, expanding the range of sensor materials to adapt the properties ideally to the system being investigated.

Overall, the new setup allowed me to obtain previously inaccessible information on long-time scales, visualize dynamic processes with plasmonic nanoparticles and introduce new sensor elements for dark-field microscopy. The new setup will be an indispensable tool in advanced molecular biology and biophysics labs around the world.

PART IV

APPENDIX

CAN WE DETECT THE PLASMON SHIFT *VIA* INTENSITY READOUT?



A.1 Material and Methods

Materials. Gold chlorate trihydrate ($\text{HAuCl}_4 \cdot 3\text{H}_2\text{O}$, $\geq 99.9\%$), hexadecyltrimethylammonium bromide (CTAB, 99%), sodium borohydride (NaBH_4 , 99.99%), hydrogen chloride (HCl, 37 wt. % in water), sodium chloride (NaCl , $\geq 99.8\%$) Tris(2-carboxyethyl)phosphine hydrochloride (TCEP, $\geq 98\%$), sodium dodecylsulfate (SDS, $> 99\%$), Tris(hydroxymethyl)aminomethane (TRIS, $\geq 99.9\%$), Streptavidin from *streptomyces avidinii* (salt-free, lyophilized powder, ≥ 13 units/mg protein), TWEEN[®]20, phosphate buffered saline (PBS) and Kanamycin sulfate from *streptomyces kanamyceticus* were obtained from Sigma Aldrich. Silver nitrate (AgNO_3 , $\geq 99.9\%$) was bought from Carl Roth, sodium oleate ($> 97\%$) from TCI and Poly(4-styrenesulfonic acid) solution (PSS, MW=75000g/mol, 18 wt. % in water), Poly(allylamine hydrochloride) (PAH, MW=17500 g/mol) and Sodium hydroxide (NaOH , 1 M) were purchased from Merck. Alpha-methoxy-omega-mercapto polyethylene glycol (Methoxy-PEG, MW = 5056 Da) and alpha-biotin-omega-mercapto polyethylene glycol (Biotin-PEG, MW=3317 Da) were bought from Iris Biotech GmbH. The aminoglycoside-binding aptamer (Sequence: 5'-HS- (CH₂)₆-GGGACTTGTTTAGGTAATGAGTCCC-3') was ordered from biomers. For all experiments, deionized water from a Merck Millipore system ($> 18 \text{ M}\Omega$, MilliQ) was used.

Synthesis and characterization of gold nanorods. I have synthesized three different gold nanorod batches 1-3 to have a variety in resonance wavelengths as needed for the section 'What is the optimal detection wavelength λ_D ?' and I

used batch 5 to determine the binding isotherm shown in the section ‘Comparison to spectral readout’. To determine the surface sensitivity, I used batch 4 to acquire the spectral data and batch 2 for the results using the intensity-based detection. The gold nanorod batches were prepared by a two-step seeded-growth process.¹ The total volume was 10 mL. Batch 1 and 3 were synthesized by former group members and I used those with permission from the Nanobiotechnology Group. The details are summarized in Table A.1.

Table A.1: Details for gold nanorod synthesis.

Batch	Seeds	AgNO ₃	AA
2	12 μ L	50 μ L / 4mM	70 μ L / 79 mM
4	10 μ L	70 μ L / 4mM	140 μ L / 79 mM
5	125 μ L	65 μ L / 4mM	50 μ L / 64 mM

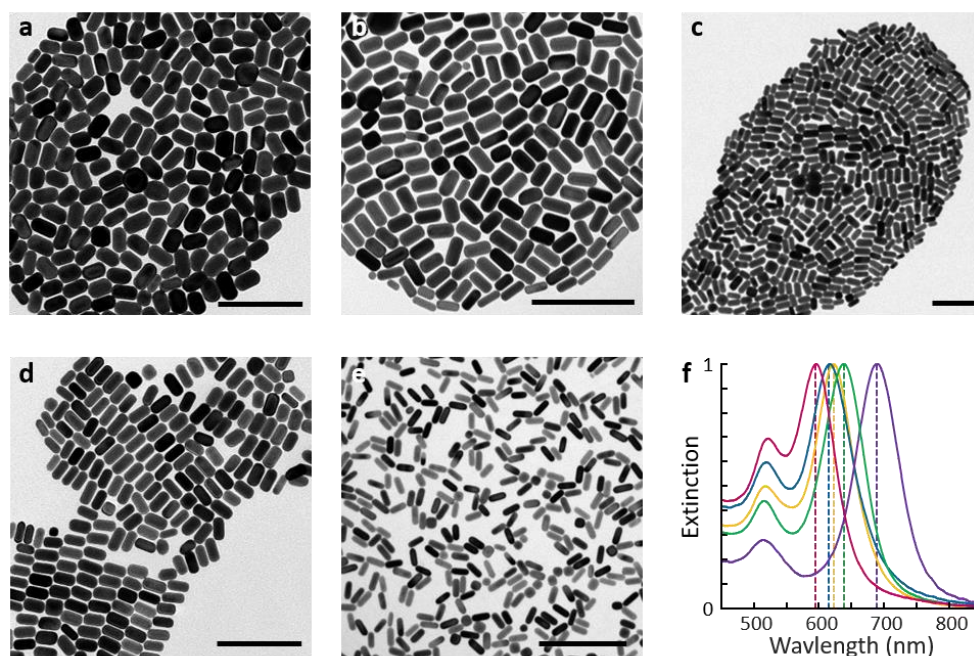


Figure A.1: TEM images and ensemble extinction spectra of gold nanosensors. (a-e) Representative TEM image of gold nanorods from batch 1 to 5. (f) Normalized ensemble extinction spectra of gold nanosensor batch 1 (magenta), batch 2 (blue), batch 3 (green), batch 4 (yellow) and batch 5 (purple). The mean resonance wavelength λ_{res} (dashed lines) is determined by applying a Gaussian function to the experimental data (upper 30%). The results are listed in Table A.2.

I characterized all four gold nanorod batches by transmission electron microscopy (TEM) and by ensemble extinction spectroscopy (see Figure A.1). TEM images were recorded using a Tecnai G2 Spirit FEI electron microscope at an acceleration voltage of 120 keV. From the TEM images, I determined the mean nanoparticle size and the standard deviation by evaluating hundreds of gold nanorods using a Matlab[®]-based software written by Andreas Henkel. The width (W) and length (L) of the nanoparticle batches are shown in Table A.2. To prepare the samples for the ensemble extinction spectroscopy, I took 50 μ L

of the nanoparticle stock solution and diluted it in 500 μL water. The spectra were measured utilizing an Ocean Optics USB 2000 spectrometer. From the data, I determined the resonance wavelength (λ_{res}) by fitting the data with a Gaussian function. The values are listed in Table A.2. Additionally, I calculated the polydispersity index (PDI) as described in Chapter D.1 (Table A.2).

Table A.2: Characterization of gold nanorods.

Batch	W (nm)	L (nm)	$V(\times 10^4 \text{ nm})$	PDI	λ_{res} (nm)
1	34.7 ± 3.9	58.1 ± 5.2	4.40 ± 1.50	1.12	594.7
2	25.4 ± 4.2	50.2 ± 4.4	2.11 ± 0.96	1.21	617.0
3	27.3 ± 6.0	60.5 ± 6.3	3.01 ± 1.84	1.37	636.2
4	26.5 ± 2.8	51.8 ± 4.7	2.37 ± 0.78	1.11	621.9
5	14.3 ± 2.2	39.6 ± 3.8	5.59 ± 2.51	1.20	688.7

Functionalization of gold nanorods with Polyethylene glycol (PEG). The functionalization process was adapted from Bach et al.² Specifically, 100 μL of the gold nanoparticle batches 1-3 were washed with water by centrifugation to remove the excess surfactant. 10 μL of a 5mM PEG solution, either Biotin-PEG or Methoxy-PEG, and 5 μL of 2% TWEEN[®]20 were added to each gold nanoparticle batch and incubated for 30 min at room temperature. After the incubation time, 50 μL of a 2M NaCl solution was added in 10 μL steps for a time interval of 10 min to increase the density of PEG by lowering electrostatic repulsion. Finally, the samples were incubated overnight on an orbital shaker at room temperature and stored until use in the fridge at 8 $^{\circ}\text{C}$.

Functionalization of gold nanorods with Aptamer. The functionalization of gold nanorod batch 4 with aminoglycoside-binding aptamer was conducted as described by Katharina Käfer³ with some modifications to the reactants' amounts. The first step was to ensure that the aptamer solution does not contain disulfide bridges. Therefore, 10 μL of a 100 μM aptamer stock solution in TRIS buffer was mixed with 2 μL of a 100 mM TCEP solution (1M NaOH and water (2:1)), 10 μL of a 1 % aqueous SDS solution, and 166 μL TRIS buffer and incubated for 30 min at room temperature. In the meantime, 100 μL of the nanoparticle sample was washed with water by centrifugation to remove the excess surfactant. The remaining pellet was quickly added to the aptamer mixture when the incubation time was completed. Finally, the sample was incubated overnight on an orbital shaker at room temperature and stored until use in the fridge at 8 $^{\circ}\text{C}$.

Note: The approach to functionalize gold nanoparticles is based on the covalent bonding between gold and thiol groups attached to the molecules of interest.^{4,5} I have adjusted the centrifugation time and relative centrifugal force (rcf) for each particle batch by balancing complete particle sedimentation while avoiding aggregation.

Flow cell preparation and cleaning. For all experiment, I used a homebuilt microfluidic flow cell. The preparation process is described in the doctoral thesis

of Christina Rosman.⁶ To clean the flow cell, between 0.5 mL to 1 mL of an aqueous Hellmanex[®] solution (v/v 50%/50%) was flushed through the flow cell, depending on the purity of the glass slide. If visual residues remained, this process was repeated. Finally, the flow cell was washed with distilled water before starting the actual measurement.

General procedure for the dark-field measurements. After the flow cell was inserted into the microscope setup ('Single Line Setup' or 'Refinement Setup') and cleaned with Hellmanex[®] solution, the gold nanosensors were randomly deposited on the glass slides of the flow cell by adding a small amount of 1 M salt solution. It was essential to use diluted particle samples to prevent aggregation of the particles. For the intensity-based measurement method, it was advantageous to prepare the microscope setup one day in advance of the measurement and, if possible, to deposit the nanosensors already. Note: For functionalized nanosensors, this was only possible under the condition that they are stable at room temperature. Subsequently, either image series with the 'Single Line Setup' or scattering spectra with the 'Refinement Setup'⁷ were acquired and evaluated to detect binding events, as shown in the figures of the main text.

QSA simulation to validate the proof-of-concept study. To check if the experimentally determined intensity increase (ΔI_{rel}), caused by the adsorption of streptavidin to biotin-PEG-coated gold nanorods, matches theoretical predictions, I simulated scattering spectra for gold nanorods using Gans' equation within the quasi-static approximation (QSA) for coated ellipsoidal particles.⁸⁻⁹ I determined the scattering intensity change at a fixed wavelength ($\lambda_D = 660$ nm, illumination wavelength I used for the experiment) for a particle size distribution, shown in Table A.2 of batch 2, with the dimension of the linker biotin-PEG (l_{PEG} 6 nm in PBS buffer) and the protein streptavidin ($D_{prot} = 5$ nm) from literature¹⁰, a refractive index for both layers of 1.45, and tabulated values for the dielectric function of gold.¹¹ From the simulated data, I determined the median for the distribution and compared the result to the experimental value (Table 2.3 main text).

Signal-to-noise ratio for Min waves utilizing the spectral and intensity readout method. To compare the performance of both detection methods to investigate the Min protein system dynamics quantitatively, I determined the signal-to-noise ratio (SNR) of the measured nanoparticles. The spectral data was recorded with a time resolution of 250 ms for 200 s and the intensity data with a time resolution of 30 ms for 400 s. I calculated the amplitude \mathcal{A} by taking the difference between the upper and lower envelope of the signal. To estimate the short-term noise, I have detrended the signal with a 0.01 Hz frequency filter and calculated the remaining signal's standard deviation N (Figure A.2), which I used as a measure for (high frequency) noise. The results for the SNR are shown in Figure 2.12 of the main text.

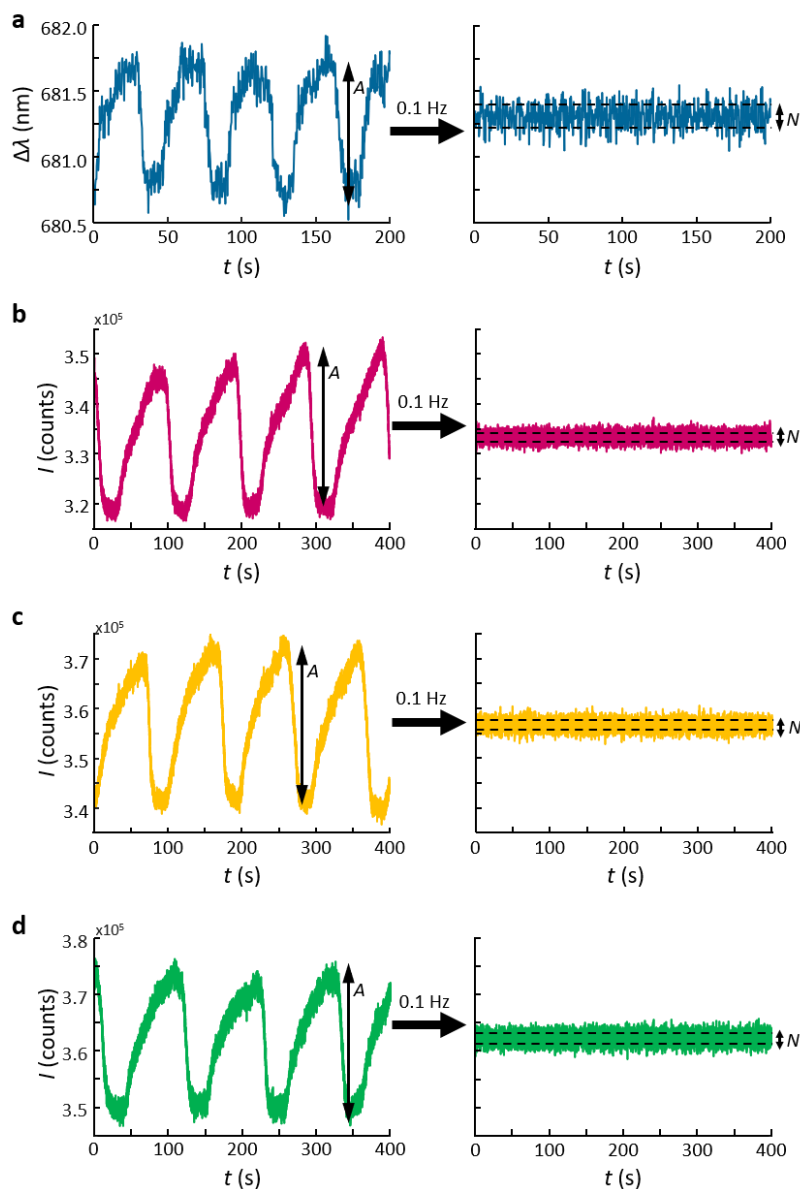


Figure A.2: Detrended signal of Min waves. Signal change of surface coverage fluctuations as a function of time **a)** recorded with the refinement setup (250 ms time resolution for 200 s) or **b-d)** with the single line setup (30 ms time resolution for 400 s). The black arrow depicts the amplitude A . The signal was detrended using a 0.1 Hz frequency filter to estimate the short-term noise by determining the standard deviation (N) of the remaining signal (right panel).

Data evaluation. To evaluate the recorded data at the single line setup, I developed a Matlab[®]-based software together with Karl Wandner. For the intensity-based method, it is essential to determine the particle intensities reliably since different noise sources such as scattering centers in the oil, defocusing or image drift can influence the measurement signal. The evaluation is based on three major steps: first, calculating the image background, second, finding the particle locations and third, calculating the particles' scattering intensities. To determine the background image, I used standard image processing methods (cf. Chapter 2 for details). After subtracting the background image from the raw

image (Figure A.2a), we find the particle positions. For this step, the Matlab[®] function 'imdilate' is used. Simplified, it works like shifting a disk with a whole in the center over image. The images are processed by the function so that only spikes (maximum pixel of each particle) remain (Figure A.2c). All pixels with values above the intensity threshold, which can be adjusted, are assigned to particles (Figure A.2d).

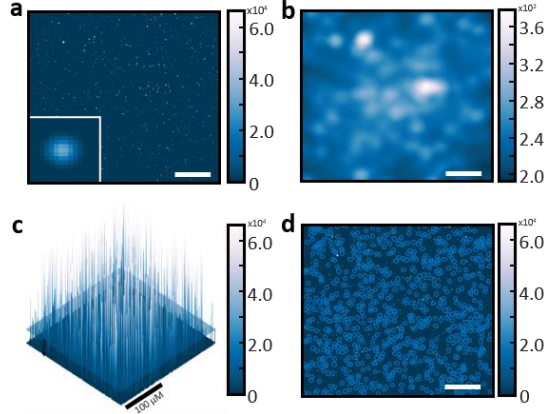


Figure A.3: Data evaluation. **a)** Raw image of the field of view recorded with the single line setup. The inset depicts the zoom-in of one single particle. **b)** A calculated background image based on the raw image in panel a). **c)** 3D image of all the particles in the field of view. The blue transparent plane indicates the intensity threshold I used to assign particles. **d)** Corrected image (Raw image subtracted the background image) with blue circles to mark the particles' location. The scale bar corresponds to $50 \mu\text{m}$ unless stated otherwise.

To correct possible image drifts, a 2D cross-correlation between the current image and the reference image is performed beforehand and if necessary, the particle positions are changed accordingly. To obtain a more stable intensity signal for each particle, we do not consider one pixel but determine the sum of several pixels (disk). For this purpose, we have generated an algorithm that calculates the diameter of the particles. Figures A.5a and A.5b show two example images of single particles, with the corresponding intensity profiles (sum in x- and y-direction). The diameter of the particle P is calculated as the mean between the number of pixels above a threshold of 20% of the maximum intensity P_x, P_y (in x- and y-direction, respectively) with one pixel added as safety margin:

$$(A1) \quad 2P = P_x + P_y + 2$$

For the disk, we use a disk diameter D that corresponds to twice the particle diameter P , i.e. $D = P_x + P_y + 2$ to ensure that most pixels contributing to the scattering intensity of the particle are considered for the calculation. Figure A.4c shows the distribution of the disk diameters D obtained in this way for all particles in the field of view. The particle size can also be used as a filter criterion for further analysis (next paragraph).

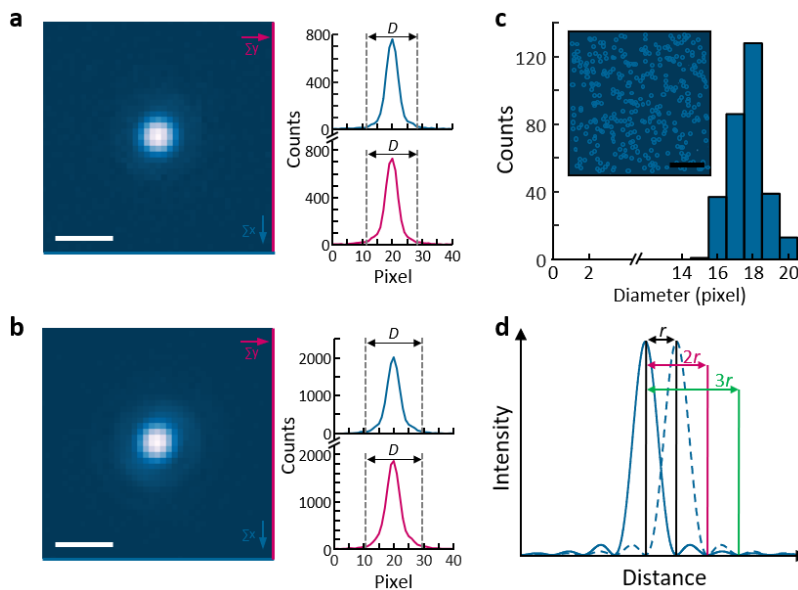


Figure A.4: Calculation of the particle diameter. a-b) Two examples for single nanoparticles images (left panel). Intensity profile in x-and y-direction, marked as a blue and magenta line in the image, respectively (right panel). The gray dashed lines indicate the diameter D of the nanoparticle's disks, I used for further calculation. c) Histogram of particle diameter distribution. Inset depict the particle image with blue circles to mark the particles' location. Scale bar corresponds to $50 \mu\text{m}$. d) Sketch of the intensity profile of two point-spread-functions (PSF, blue solid and dashed line). The black arrow depicts the Rayleigh criterion (inset). The other two arrows illustrate the distance needed to capture the first-order (pink) or second-order (green) diffraction.

Besides, I compared whether the value of the diameter P is in the theoretical expected range. For this purpose, I approximated the diameter of the Airy disk with the Rayleigh criterion¹² (Figure A.4d) as shown below.

$$P = 2 \cdot \left(0.61 \frac{\lambda}{NA}\right) \cdot M_g \quad (\text{A2})$$

With λ being the wavelength of the light used ($\lambda = 660 \text{ nm}$), NA is the numerical aperture of the lens ($NA = 0.7$) and M_g is the magnification ($M_g = 50\times$).

From this, we calculate a nanoparticle diameter of $58 \mu\text{m}$, which corresponds to a pixel number of 9 for the camera we use (pixel size of $6.5 \mu\text{m}$). To obtain measurement signals stable against slight defocusing, it turned out to be important not only to consider the central maximum as calculated using the Rayleigh criterion but also to include the first side-maximum (equals to a factor of 2), which results in about 18 pixels as ideal size for the disk over which the intensity is summed. The resulting value corresponds to the experimentally determined median of 18 pixels.

Another aspect of the method development was the filtering of the signal. Since the intensity-based measurement method no longer has the particle spectra to make a preselection, I incorporated additional analysis criteria. I want to explain the filter in more detail by applying them to three example measurements. For this, I have looked at the extent to which the different filters influence the measurement signal, its standard deviation and the number of particles. Before I present the result, I would like to explain the filters briefly.

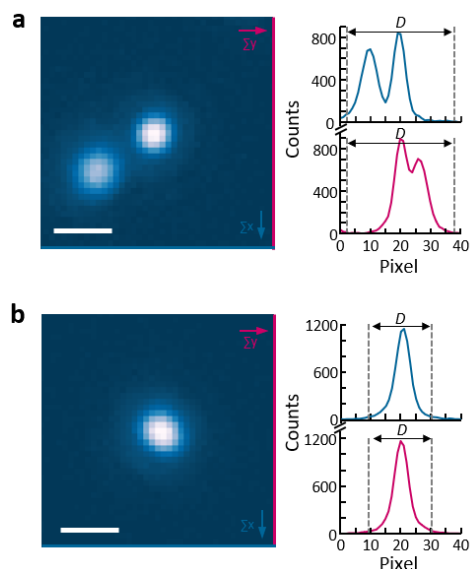


Figure A.5: Bad particles. Examples for nanoparticle images (left panel), where **a**) the particles are too close to each other or **b**) not individual particles (aggregates). Intensity profile in x- and y-direction, marked as a blue and magenta line in the image, respectively (right panel). The gray dashed lines indicate the diameter D of the nanoparticles. Determined by the software.

Particle size. As already indicated in the paragraph above, one can use the individual particle size as a filter criterion. If the calculated particle diameter is above the fixed diameter used for the analysis, the 'bad' particles are excluded from further evaluation. For example, the reasons for larger values can be that two particles are too close to each other or are not individual particles, as shown in Figure A.5. Furthermore, one can use the particle size difference between the two measurements. The diameter should not increase more than 10% to avoid problems due to defocusing between the runs.

Shift. The Shift filter uses the principle of removing all particles larger and smaller than two sigma of the mean value to identify outliers.

Negative. This filter removes all particles from the measurements whose intensity decreases. The adsorption of an analyte causes a redshift of the plasmon and thus an intensity increase if the detection wavelength is close to its optimal. Therefore, a decrease in intensity can be attributed to an unfavorable particle resonance wavelength. (cf. Chapter 2).

Applying the filters shows that the average relative intensity change remains nearly constant, the standard deviation decreases, and the particle numbers decrease as well (as expected). To judge how good the three filters are, I looked at the signal-to-noise ratio. As signal, I took the average relative intensity change and as noise the standard deviation. It shows that the SNR improves through the filters, with the largest improvement (about a factor of 2) occurring by using all filters, which filters out approximately 20-35% of the spots. Note: The neg-filter should be used with caution since only outliers in resonance wavelength distribution of the particle ensemble should be affected. If real physical effects,

e.g., charging could occur during the measurement than this filter is not applicable.

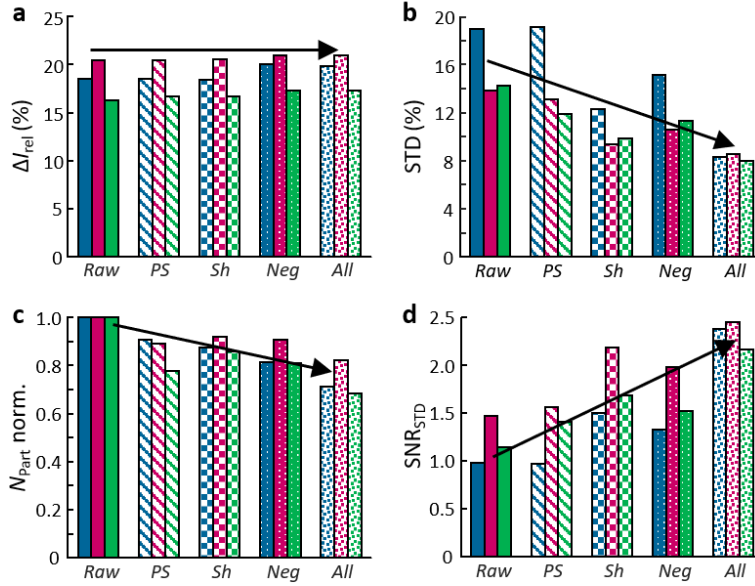


Figure A.6: Data analysis. Bar plot showing the **a)** relative intensity change (ΔI_{rel}), **b)** the standard deviation (STD), **c)** the number of nanoparticles (N_{part}) and **d)** the signal-to-noise ratio (SNR_{STD}). The evaluation was done for the data without filtering (*Raw*) and after applying the particle size (*PS*) or the shift (*Sh*) filter, discarding negative shifting nanoparticles (*Neg*) and for the combination (*All*) for three different measurements.

A.2 Supplementary Text

What is the optimal detection wavelength of a single particle? To determine the optimal detection wavelength λ_D for a single nanoparticle, I approximated the particle's scattering spectrum with a Lorentzian function (see equation (A3)).

$$I(\lambda) = \frac{I_m \Gamma^2}{4(\lambda - \lambda_{res})^2 + \Gamma^2} \quad (A3)$$

If the particles close surrounding changes, the resonance wavelength shifts by $\Delta\lambda_{res}$ and the intensity increases by ΔI . Since the nanoparticles have a size and shape distribution, we decided to normalize the intensity change to the initial intensity $I(\lambda_D)$: $\Delta I_{rel} = \Delta I / I(\lambda_D)$. The optimal detection wavelength λ_D is where the signal change is largest, i.e., the maximum of $(dI/d\lambda)/I$. Ignoring the change in maximum intensity and linewidth, we get:

$$\frac{dI/d\lambda|_{\lambda_D}}{I(\lambda_D)} = -\frac{8(\lambda_D - \lambda_{res})}{4(\lambda_D - \lambda_{res})^2 + \Gamma^2} \quad (A4)$$

The largest change is obtained when the derivative of equation (A4) (equation (A5)) becomes zero.

$$\frac{d}{d\lambda_D} \left[-\frac{8(\lambda_D - \lambda_{res})}{4(\lambda_D - \lambda_{res})^2 + \Gamma^2} \right] = \frac{32(\lambda_D - \lambda_{res})^2 + 8\Gamma^2}{(4(\lambda_D - \lambda_{res})^2 + \Gamma^2)^2} = 0! \quad (A5)$$

with I_m being the maximum scattering intensity, Γ the particle's linewidth, λ_{res} the resonance wavelength and λ the illumination wavelength.

Solving for λ_D , we obtain that the optimum is at $\lambda_D = \lambda_{\text{res}} \pm \Gamma/2$.

A.3 Bibliography

1. Nikoobakht, B.; El-Sayed, M. A., Preparation and Growth Mechanism of Gold Nanorods (NRs) Using Seed-Mediated Growth Method. *Chemistry of Materials* **2003**, *15* (10), 1957-1962.
2. Liu, K.; Zheng, Y.; Lu, X.; Thai, T.; Lee, N. A.; Bach, U.; Gooding, J. J., Biocompatible Gold Nanorods: One-Step Surface Functionalization, Highly Colloidal Stability, and Low Cytotoxicity. *Langmuir* **2015**, *31* (17), 4973-4980.
3. Kaefer, K. Plasmonic Gold Nanoparticles as Implantable Medical Sensors. PhD Thesis, Johannes Gutenberg-Universität, Mainz, **2018**.
4. Daniel, M.-C.; Astruc, D., Gold Nanoparticles: Assembly, Supramolecular Chemistry, Quantum-Size-Related Properties, and Applications toward Biology, Catalysis, and Nanotechnology. *Chemical Reviews* **2004**, *104* (1), 293-346.
5. Sperling, R. A.; Parak, W. J., Surface modification, functionalization and bioconjugation of colloidal inorganic nanoparticles. *Philosophical Transactions of the Royal Society A: Mathematical, Physical and Engineering Sciences* **2010**, *368* (1915), 1333-1383.
6. Rosman, C. Biological Applications of Plasmonic Metal Nanoparticles. PhD Thesis, Johannes Gutenberg-Universität, Mainz, 2013.
7. Henkel, A. Rod-shaped Plasmon Sensors. PhD Thesis, Johannes Gutenberg-Universität, Mainz, 2012.
8. Gans, R., Über die Form ultramikroskopischer Goldteilchen. *Annalen der Physik* **1912**, *342* (5), 881-900.
9. Becker, J. Plasmons as Sensors. PhD, Johannes Gutenberg-Universität Mainz, 2010.
10. Tüting, L.; Ye, W.; Settanni, G.; Schmid, F.; Wolf, B. A.; Ahijado-Guzmán, R.; Sönnichsen, C., Potassium Triggers a Reversible Specific Stiffness Transition of Polyethylene Glycol. *The Journal of Physical Chemistry C* **2017**, *121* (40), 22396-22402.
11. Johnson, P. B.; Christy, R. W., Optical Constants of the Noble Metals. *Physical Review B* **1972**, *6* (12), 4370-4379.
12. Pedrotti, F.; Pedrotti, L.; Bausch, W.; Schmidt, H., *Optik für Ingenieure*. Springer-Verlag Berlin Heidelberg: 2008.

A.4 Copyright

The Figure 2.11b in Chapter 2 is adapted from Figure 2b of the manuscript entitled ‘Single Particle Plasmon Sensors as Label-Free Technique to Monitor MinDE Protein Wave Propagation on Membranes’ published in Nano Letters. *Nano Lett.* **2016**, 16, 3540–3544. Copyright ©2021 American Chemical Society.



RightsLink®



Home



Help



Email Support



Sign in



Create Account

ACS Publications
Most Trusted. Most Cited. Most Read.

Single Particle Plasmon Sensors as Label-Free Technique To Monitor MinDE Protein Wave Propagation on Membranes

Author: Christina Lambertz, Ariadna Martos, Andreas Henkel, et al

Publication: Nano Letters

Publisher: American Chemical Society

Date: Jun 1, 2016

Copyright © 2016, American Chemical Society

PERMISSION/LICENSE IS GRANTED FOR YOUR ORDER AT NO CHARGE

This type of permission/license, instead of the standard Terms & Conditions, is sent to you because no fee is being charged for your order. Please note the following:

- Permission is granted for your request in both print and electronic formats, and translations.
 - If figures and/or tables were requested, they may be adapted or used in part.
 - Please print this page for your records and send a copy of it to your publisher/graduate school.
 - Appropriate credit for the requested material should be given as follows: "Reprinted (adapted) with permission from (COMPLETE REFERENCE CITATION). Copyright (YEAR) American Chemical Society." Insert appropriate information in place of the capitalized words.
 - One-time permission is granted only for the use specified in your request. No additional uses are granted (such as derivative works or other editions). For any other uses, please submit a new request.
- If credit is given to another source for the material you requested, permission must be obtained from that source.

[BACK](#)[CLOSE WINDOW](#)

INTENSITY-BASED SINGLE PARTICLE PLASMON SENSING



B.1 Material and Methods

Materials. Gold chlorate trihydrate ($\text{HAuCl}_4 \cdot 3\text{H}_2\text{O}$, $\geq 99.9\%$), hexadecyltrimethyl-ammonium bromide (CTAB, 99%), sodium borohydride (NaBH_4 , 99.99%), hydrogen chloride (HCl, 37 wt. % in water), sodium chloride (NaCl, $\geq 99.8\%$) and D-(+)-glucose ($\geq 99.5\%$) were obtained from Sigma Aldrich. Silver nitrate (AgNO_3 , $\geq 99.9\%$) was bought from Carl Roth, sodium oleate ($> 97\%$) from TCI and Poly(4-styrenesulfonic acid) solution (PSS, MW=75000g/mol, 18 wt. % in water) and Poly(allylamine hydrochloride) (PAH, MW=17500 g/mol) were purchased from Merck. For all experiments, we used deionized water from a Merck Millipore system ($> 18 \text{ M}\Omega$, MilliQ).

Synthesis and characterization of gold nanorods. We have synthesized three different gold nanorod batches to have a variety in resonance wavelengths λ_{res} but approximately the same volume. The gold nanorods were prepared by a two-step seeded-growth process according to literature¹⁻³ with the details specified in Table B.1. The dimensions of the gold nanorods were determined by transmission electron microscopy (TEM) using a Tecnai G2 Spirit FEI electron microscope at an acceleration voltage of 120 keV (representative images in Figure B.1).

Table B.1. Details for gold nanorod synthesis.

Batch	Seeds	AgNO ₃	conc. HCl	AA	5-BrSA
● 1 ¹	10 μL	70 μL / 4mM	-	140 μL / 79 mM	-
● 2 ²	50 μL	180 μL / 4mM	16 μL	27 μL / 64 mM	-
● 3 ³	800 μL	12 mL / 4mM	-	2 mL / 64 mM	1.1 g

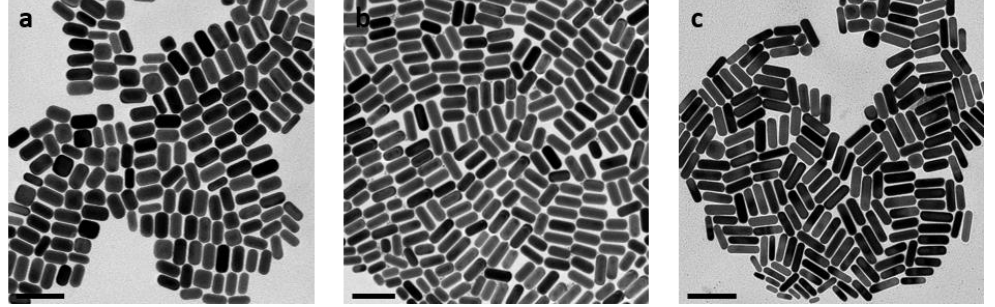


Figure B.1. Characterization of gold nanorods. Transmission electron microscopy images of gold nanorods used for the experiments presented in Figure 3.4 of the main text and in Figure B.2. The average dimensions are listed in Table B.2. The scale bar is 100 μm in all images.

From such images, we obtained the diameter (D) and length (L) of hundreds of nanorods and calculated with these values the particle volume by assuming a spherically capped cylinder shape: $V_{\text{TEM}} = \frac{\pi}{6} D^3 \left(\frac{3L}{2D} - \frac{1}{2} \right)$. The results are listed in Table B.2.

Table B.2. Characterization of gold nanorods.

Batch	D (nm)	AR	V_{TEM} (nm ³)	λ_{res} (nm)
● 1	26.5 ± 2.8	2.0 ± 0.2	28869 ± 7895	636.4 ± 17.4
● 2	23.3 ± 2.0	2.4 ± 0.3	24127 ± 6278	683.0 ± 19.8
● 3	19.5 ± 2.6	3.2 ± 0.4	18837 ± 5846	748.4 ± 29.0

Experimental verification of the intensity surface sensitivity \mathcal{S}_I and the intensity bulk sensitivity \mathcal{S}_I . To verify our theoretical description of the quantities \mathcal{S}_I and \mathcal{S}_I experimentally, we recorded the response of three batches of gold nanorods (batch 1-3) to changes in their close surroundings by the adsorption of polyelectrolyte layers with a homebuilt darkfield microscope.⁴ We immobilized the nanorods at the bottom of a microfluidic flow cell with sodium chloride (1 M) and washed the nanorods with a water/ethanol mixture (50%/50%) to remove the remaining surfactant. After the washing process, we deposited bilayers of poly (styrene sulfonate) (PSS) and poly (allyl amine hydrochloride) (PAH)⁵⁻⁷ sequentially and recorded the corresponding scattering spectra of the gold nanorods. If appropriate, we filtered the solutions to avoid problems from dust swimming near the nanoparticles. From these spectra, we determined the relative intensity change ΔI_{rel} at the detection wavelength λ_D^* by

fitting the data with a Lorentzian function. ΔI_{rel} shows a linear response for small layer changes.

Therefore, we extracted the proportionality factor S_I ($\Delta I_{\text{rel}} = S_I \cdot \Delta l$) for each particle from the linear fit and compared the result to values simulated using the boundary element method (BEM) (Figure 4b Main Text). S_I depends on the resonance wavelength. Hence, we have accounted for the resonance wavelength distribution of our particle batches 1-3 for the BEM predictions. As a lower limit, we used the mean resonance wavelength of batch 1 subtracting its standard deviation ($\lambda_{\text{res}} = 619$ nm) and as an upper limit the mean resonance wavelength of batch 3 adding its standard deviation ($\lambda_{\text{res}} = 777$ nm). In our measurements, the gold nanorods are immobilized on a glass surface, which means that only 60% of their sensing volume is available (c.f. Figure B.3). We consider this reduced sensitivity for our comparison and adjust the measurements accordingly.

To compute S_I from these measurements, we first had to estimate the particle's sensing distance d_s . From our previous work⁸, we know that d_s scales with the cubic root of the particles' volume V as $d_s = 0.37 \cdot V^{(1/3)}$. We used the method reported in our previous work⁸ to estimate the particle volume for each particle from its individual maximum scattering intensity I_{max} and its individual linewidth Γ . With these parameters and the known mean particle size (from TEM, Table B.2), we could estimate the individual particle volume V_i using the relationship

$$V_i = \sqrt{\frac{I_{\text{max}} \cdot \Gamma^2}{\langle I_{\text{max}} \cdot \Gamma^2 \rangle}} \cdot V_{\text{TEM}} \quad (\text{B1})$$

The knowledge of d_s for all individual nanoparticles allowed us to determine the intensity bulk sensitivity S_I . The results are presented in Figure 4a of the main text. Again, we related these results to our theoretical predictions. We have to note that S_I is a volume dependent quantity and thus, we have included the volume distribution of our particle batches for the theoretical predictions. As a lower volume limit, we used values obtained by the quasi-static approximation (QSA) for small-sized particles and as an upper limit the mean particle volume of batch 1 adding its standard deviation ($V = 33.9 \cdot 10^4$ nm³).

QSA simulation. To verify the description of our mathematical model for the intensity bulk sensitivity S_I , the 'Shift-Term' $S_{I_{\text{shifft}}}$ and the 'Intensity-Term' $S_{I_{\text{max}}}$, we simulated scattering spectra for gold nanorods with 10 nm diameter and various aspect ratios (1.5 to 6 in steps of 0.1) in two different refractive index media ($n_1 = 1.33$ and $n_2 = 1.331$). These simulations were calculated using Gans' equation within the quasi-static approximation (QSA) for ellipsoidal particles with tabulated values for the optical constant of gold.⁹⁻¹⁰ From the scattering spectra, we obtained the resonance wavelength λ_{res} and the linewidth Γ by fitting the data with a Lorentzian function. From these values, we determined the resonance wavelength bulk sensitivity S_λ according to $S_\lambda = \frac{\Delta \lambda_{\text{res}}}{\Delta n}$ and computed

*The detection wavelength λ_D is different for every gold nanorod due to their resonance wavelength distribution.

S_I , $S_{I_{\text{shift}}}$ and $S_{I_{\text{max}}}$, respectively. We compared these results to the values calculated with the formulas we derived in this work. The results are presented in Figure 3.2 and Figure 3.3.

BEM simulation. To check if our mathematical model of the intensity bulk sensitivity SI holds for larger gold nanorods, we calculated scattering spectra (wavelength from 480 to 1500 nm) for gold nanorods (modeled as spherocylindrical rod) with different aspect ratios (1.5 to 4.5, 0.1 steps) and diameters (15 nm to 55 nm, 1nm steps) embedded in water ($n_1 = 1.33$ RIU) and a slightly higher refractive index material ($n_2 = 1.331$ RIU) using the boundary element method (BEM).¹¹ From those scattering spectra, we obtained the resonance wavelength λ_{res} , the linewidth Γ , and computed the resonance wavelength bulk sensitivity S_λ according to $S_\lambda = \frac{\Delta\lambda_{\text{res}}}{\Delta n}$. To increase the total number of data points, we interpolated all values with a cubic spline function. We used these values (λ_{res} , Γ and S_λ) and tabulated values for the optical constant of gold to determine SI with equation (B16).¹⁰ We show the results in Figure 3.3 for S_I and in Figure B.3a for S_λ .

Molecular sensing under ‘real’ conditions. To demonstrate that our equations can be used to predict the outcome of an experiment under ‘real’ conditions, we investigated the adsorption of a lipid bilayer (DOPC/DOPG/CL (70/25/5) molar ratio) on nanoparticles. In such a ‘real experiment’, we use a common detection wavelength (Thorlabs Mounted LED, M735L3) for all particles, which is not the ‘optimal’ detection wavelength for all particles due to their inhomogeneous size and shape distribution. After depositing particles as described above, we have recorded the scattering intensity of each particle twice in the same buffer solution (50 mM Tris-HCl (pH 7.5), 150 mM KCl) to determine the measurement accuracy (Figure B.2, left panel). As expected, we see no change in the average and the deviation (the measurement accuracy) is well below 1%. We then deposited the lipid bilayer to the gold nanorods⁸ leading to an increase of the particle’s intensity by 47% on average (Figure B.2 blue dot). Note: We have adjusted the measurement data to account for the substrate effect of 60%.

To check if the outcome of such an experiment, where a common detection wavelength is used that is not ‘optimal’ for all particles, still follows the prediction from the equations developed in this work, we added the prediction as a yellow dot in the same figure. The input values are listed in Table B.3, and we estimate their error to be about 10% - 20% (error bar). We obtain an intensity increase of about 59% (Figure B.2 yellow dot), slightly higher than the measured value, which is expected from the suboptimal detection wavelength for some particles. A common detection method in the plasmonic sensing community is to use an ensemble of particles as a sensing platform.¹²

Table B.3. Input values* to determine the theoretical intensity change presented in Figure B.3.

	D (nm)	AR	I (nm)	λ_{res} (nm)	S_λ (nm/RIU)	d_s (nm)	l_L (nm)	n (RIU)	n_L (RIU)	ϵ_2	$d\epsilon_2 / d\lambda_{\text{res}}$ (1/nm)
gold	33.3	2.2	43	659	298	14.4	4.2	1.33	1.45	1.04	-0.0047

*The values (I , λ_{res} , S_λ) are determined using the boundary element method (BEM) for the average size of gold nanorods (Batch #5 in reference 8). The sensing distance d_s and the lipid bilayer thickness l_L are in accordance to literature.⁸ The refractive indices are estimated for water n and the lipid bilayer n_L . We used tabulated optical constants for gold reported in Johnson and Christy.¹⁰

To test if our approach is suitable for a particle ensemble, we sum up all particle's scattering intensities before and after the lipid bilayer's adsorption to determine the signal change. An intensity increase of 44% results (Figure B.3 magenta dot), which is very close to the mean of the change of individual particles validating the ensemble approach.

In conclusion, our theoretical model predicts reasonably well the outcome for experiments using a fixed detection wavelength for all particles, with the 'ideal' case being the upper limit and the real values 10% - 20% lower, depending on particle inhomogeneity. Furthermore, the evaluation on the single particle level is not essential and the outcome of ensemble evaluation is more or less identical.

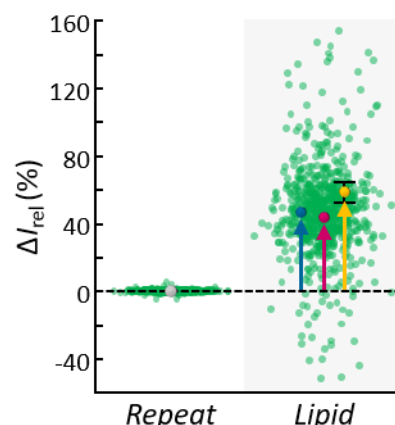


Figure B.2: Molecular sensing under 'real' conditions. The intensity changes ΔI_{rel} before and after adsorption of a lipid bilayer (gray area) for hundreds of single nanoparticle sensors (green dots). The large colored dots show the mean value of all particles for the repeat measurement (in gray), for the adsorption of the lipid bilayer ($\Delta I_{\text{rel}} = 47\%$, in blue), the calculated average intensity change of the particle ensemble ($\Delta I_{\text{rel}} = 44\%$, in magenta) and the theoretical expected intensity change ($\Delta I_{\text{rel}} = 59\%$, in yellow). The error bar depicts the estimated error (10%) of the theoretical value. The three arrows visualize the difference.

B.2 Supplementary Text

Influence of the glass substrate. To estimate the influence of the glass substrate on our measurement signal, we monitored the response of individual nanorods (batch 1-3) to refractive index changes (Δn) of the surrounding medium using a homebuilt darkfield microscope.⁴ We immobilized our nanorods with sodium chloride (1M) at the bottom of a microfluidic flow cell and washed the nanorods with a water/ethanol mixture (50% /50%) to remove excess surfactant. After the washing process, we measured for all the particles in the field-of-view single particle scattering spectra in different refractive index

§It is important to measure forth and back, to exclude irreversible changes and thus, false results for the sensitivity.

solutions (here, glucose at various concentrations in 1M NaCl)[§]. To calculate the resonance wavelength sensitivity S_λ for each individual particle, we determined from those spectra the resonance wavelength shift $\Delta\lambda_{\text{res}}$ by fitting the data with a Lorentzian function. For small refractive index changes of the surrounding medium, the data show a linear response. We extracted the proportionality factor S_λ ($\Delta\lambda_{\text{res}} = S_\lambda \cdot \Delta n$) for each particle from this linear fit. We compared the experimental values for S_λ with calculations (see below). The results match best, if we assume that 60% of the particles' sensing volume is available (c.f. Figure B.3b).

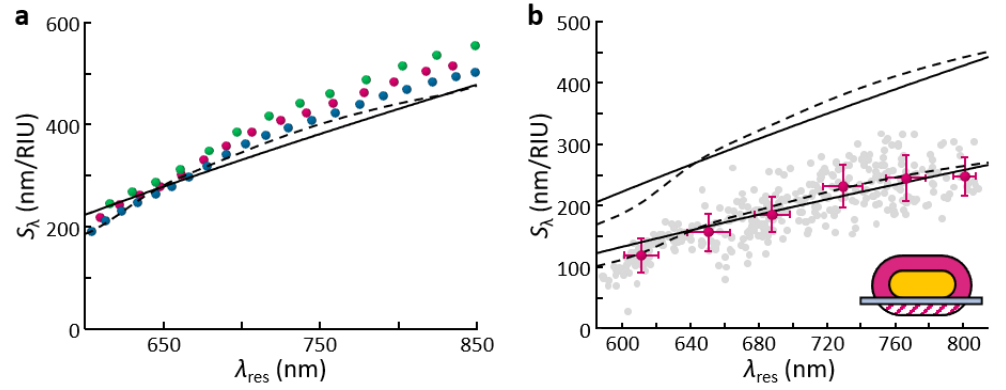


Figure B.3: Plasmon bulk sensitivity S_λ . **a)** Plasmon bulk sensitivity S_λ as function of resonance wavelength λ_{res} calculated with our mathematical models (equation (B6), dashed line and equation (B7), solid line) and electrodynamic calculations using the boundary element method (BEM) for different volumes mimicking small ($V = 1 \cdot 10^4 \text{ nm}^3$, blue dots), medium ($V = 5 \cdot 10^4 \text{ nm}^3$, pink dots) and large sized particles ($V = 15 \cdot 10^4 \text{ nm}^3$, green dots). **b)** Experimentally determined plasmon bulk sensitivity S_λ as a function of the resonance wavelength λ_{res} for the gold nanorod batches 1-3 (grey dots). The pink data points represent the average S_λ of experimental values in successive 20 nm intervals and the error bars the standard deviation for S_λ and λ_{res} , respectively. Theoretical expected trends of S_λ calculated using equation (B6) (solid lines) and equation (B7) (dashed lines) without considering the glass surface (upper lines) and assuming that only 60% of the particles' sensing volume is available (lower lines). The inset shows a gold nanorod immobilized on a glass surface (grey line). Part of the particles sensing volume (pink area) is blocked by the glass surface (pink dashed area).

Derivation of plasmon bulk sensitivity S_λ . The plasmon resonance is the frequency or wavelength where the polarizability α has a maximum. For particles with dimensions much smaller than the wavelength of light, this polarizability is given by the Clausius-Mossotti equation (simplified from Richard Gans)⁹:

$$(B2) \quad \frac{\alpha}{\epsilon_0} = \frac{V}{L} \cdot \frac{\epsilon - n^2}{\epsilon + n^2 \left(\frac{1}{L} - 1 \right)}$$

Here, V is the particle volume, L is a geometry factor, $1/3$ for spheres and $\frac{1}{L} \approx \left(\frac{a}{b} + 1 \right)^{1.6}$ for rods with the aspect ratio a/b smaller than 4, n is the medium's refractive index and $\epsilon = \epsilon_1 + i\epsilon_2$ the particle's dielectric function

In metals, the real part of the particles' susceptibility ϵ_1 can be negative and, especially for coin and alkali metals, the imaginary part ϵ_2 is comparatively small. Together, this leads to a strong maximum of the polarizability at a specific wavelength, the resonance wavelength λ_{res} . If ϵ_2 depends only weakly on wavelength, the polarizability has a maximum near the place where the real part \Re of the denominator in equation (B2) is zero:

$$\Re\left(\varepsilon + n^2\left(\frac{1}{L} - 1\right)\right) = 0 \quad (\text{B3})$$

This equation defines the condition for the resonance wavelength λ_{res} :

$$\varepsilon_1(\lambda_{\text{res}}) = -n^2\left(\frac{1}{L} - 1\right) \quad (\text{B4})$$

The refractive index sensitivity $S_\lambda = \frac{d\lambda_{\text{res}}}{dn}$ characterizes how strongly λ_{res} changes for small changes of the surrounding refractive index n . To compute S_λ , we expand with ε_1 by writing:

$$S_\lambda = \frac{d\lambda_{\text{res}}}{dn} = \frac{d\lambda_{\text{res}}}{d\varepsilon_1} \cdot \frac{d\varepsilon_1}{dn} = \frac{1}{d\varepsilon_1/d\lambda_{\text{res}}} \cdot \frac{d\varepsilon_1}{dn} \quad (\text{B5})$$

If we insert equation (S4) in equation (S5), we obtain:

$$S_\lambda = \frac{-2n\left(\frac{1}{L} - 1\right)}{\left.\frac{d\varepsilon_1}{d\lambda}\right|_{\lambda_{\text{res}}}} \quad (\text{B6})$$

We found earlier that for a Drude metal, it is also given by¹³

$$S_\lambda = \frac{\lambda_{\text{res}}}{n} \left(1 - \frac{n_\infty^2 \lambda_p^2}{\lambda_{\text{res}}^2}\right) \quad (\text{B7})$$

Both results, equation (B6) and equation (B7) are compared to the results from a simulation of nanorod spectra within the boundary element method (BEM) in Figure B.3a and show a good agreement. The advantage of equation (B6) is that it does not assume a dielectric function that follows the Drude model (which is important for metals with strong interband damping), the advantage of equation (B7) is that it is completely independent from the particle geometry, which enters only via the resonance wavelength.

Derivation of intensity bulk sensitivity S_I . If the refractive index n of the environment of the nanoparticle changes, the scattering intensity I changes as well. The absolute scattering intensity depends, among other things, on the illumination intensity and is therefore not a fundamental property of the nanoparticle itself. We use the *relative* intensity change as a measure for the sensitivity to (bulk) environmental changes and define the (relative) intensity bulk sensitivity:

$$S_I = \frac{dI/dn|_{\lambda_D}}{I(\lambda_D)} \quad (\text{B8})$$

The scattering spectrum of a plasmonic nanoparticle resembles to very good approximation a Lorentzian function and responds to a refractive index change (Δn) with a resonance wavelength shift and a change in maximum intensity. Therefore, we write the scattering intensity I as a product of a normalized Lorentzian function L and the intensity at the maximum I_{max} :

$$I = I_{\text{max}} \cdot L \quad (\text{B9})$$

Where n_∞ is the background refractive index arising from the bound d-band electrons and λ_p the plasma frequency of the conduction band electrons, for gold with $\lambda_p = 136$ nm and $n_\infty = 3.1$ or $\lambda_p n_\infty = 422$ nm.

The normalized Lorentz function has only two parameters, the peak or resonance wavelength λ_{res} , the linewidth at half maximum Γ , and is equal to

$$(B10) \quad L = \frac{\Gamma^2}{4 \cdot (\lambda - \lambda_{\text{res}})^2 + \Gamma^2}$$

The intensity refractive index sensitivity depends on the position of the detection wavelength λ_{D} relative to the plasmon resonance wavelength λ_{res} . The largest relative change is near $\lambda_{\text{D}} = \lambda_{\text{res}} + \frac{\Gamma}{2}$. At this wavelength is $L = \frac{1}{2}$ by definition. We know that changes of the refractive index of the environment (Δn) shift the plasmon resonance wavelength by $\Delta \lambda_{\text{res}}$ and change the linewidth at half maximum by $\Delta \Gamma$. At the same time, the maximum intensity I_{max} is increased by ΔI_{max} . We estimate the effect of these changes at the detection wavelength by inserting equation (B9) into equation (B8) and simplifying with the above-mentioned relationship for the Lorentzian function:

$$(B11) \quad \begin{aligned} S_{\text{I}} &= \frac{1}{I(\lambda_{\text{D}})} \cdot \frac{d}{dn} [I_{\text{max}} \cdot L] \Big|_{\lambda_{\text{D}}} \\ &= \frac{2}{I_{\text{max}}} \left(\frac{dI_{\text{max}}}{dn} \cdot L + \frac{dL}{dn} \cdot I_{\text{max}} \right) \Big|_{\lambda_{\text{D}}} \\ &= \frac{1}{I_{\text{max}}} \cdot \frac{dI_{\text{max}}}{dn} + 2 \cdot \frac{dL}{dn} \Big|_{\lambda_{\text{D}}} \end{aligned}$$

To calculate the first term $\left(\frac{1}{I_{\text{max}}} \cdot \frac{dI_{\text{max}}}{dn} \right)$ in equation (S11), named ‘*Intensity-Term*’ ($S_{\text{I}_{\text{max}}}$) in the following, we use¹⁴

$$(B12) \quad I_{\text{max}} = \text{const} \cdot \frac{n^8}{\lambda_{\text{res}}^4 \cdot \varepsilon_2^2} \Big|_{\lambda_{\text{res}}}$$

$$(B13) \quad S_{\text{I}_{\text{max}}} = \frac{\frac{dI_{\text{max}}}{dn}}{I_{\text{max}}} = \left(\frac{8}{n} - \frac{4S_{\lambda}}{\lambda_{\text{res}}} - \frac{2S_{\lambda}}{\varepsilon_2} \frac{d\varepsilon_2}{d\lambda_{\text{res}}} \right)$$

We continue with the second term $\left(2 \cdot \frac{dL}{dn} \right)$ in equation (B11), called ‘*Shift-Term*’ ($S_{\text{I}_{\text{shift}}}$) in the following.

$$(B14) \quad \begin{aligned} S_{\text{I}_{\text{shift}}} &= 2 \frac{dL}{dn} \Big|_{\lambda_{\text{D}}} = 2 \frac{dL}{d\lambda_{\text{res}}} \cdot \frac{d\lambda_{\text{res}}}{dn} = 2 \frac{d}{d\lambda_{\text{res}}} \left[\frac{\Gamma^2}{4 \cdot (\lambda - \lambda_{\text{res}})^2 + \Gamma^2} \right] \cdot S_{\lambda} \\ &= \left(\frac{1}{\Gamma} \frac{d\Gamma}{d\lambda_{\text{res}}} + \frac{2}{\Gamma} \right) \cdot S_{\lambda} \end{aligned}$$

If we insert the results of equation (B13), in blue, and equation (B14), in pink, into equation (B11), we obtain:

$$(B15) \quad S_{\text{I}} = \frac{8}{n} + \frac{-4S_{\lambda}}{\lambda_{\text{res}}} + \frac{-2S_{\lambda}}{\varepsilon_2} \frac{d\varepsilon_2}{d\lambda_{\text{res}}} + \frac{S_{\lambda}}{\Gamma} \frac{d\Gamma}{d\lambda_{\text{res}}} + \frac{2S_{\lambda}}{\Gamma}$$

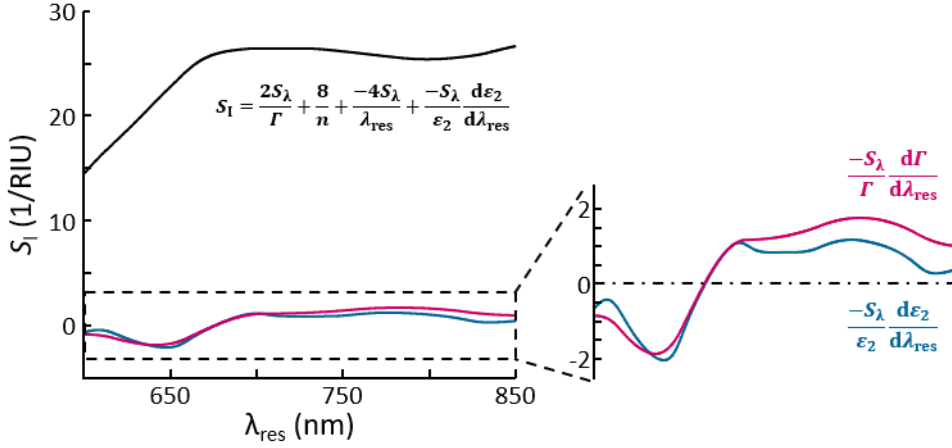


Figure B.4: Comparison of the bulk damping of gold nanoparticles to the overall intensity bulk sensitivity S_I . Intensity bulk sensitivity S_I as a function of resonance wavelength λ_{res} (black line) compared to the contribution of the particle's linewidth change (pink line) or the contribution of the imaginary part of the particle's susceptibility (blue line).

We find that $\frac{S_\lambda}{\epsilon_2} \frac{d\epsilon_2}{d\lambda_{\text{res}}}$ and $\frac{S_\lambda}{\Gamma} \frac{d\Gamma}{d\lambda_{\text{res}}}$ occur in both terms and show approximately the same trend when compared to the total equation of S_I (c.f. Figure S2), which simplifies the equation above to:

$$S_I = \frac{8}{n} - \frac{4S_\lambda}{\lambda_{\text{res}}} - \frac{S_\lambda}{\epsilon_2} \frac{d\epsilon_2}{d\lambda} + \frac{2S_\lambda}{\Gamma} \quad (\text{B16})$$

Derivation of intensity surface sensitivity \mathcal{S}_I . More interesting than the intensity bulk sensitivity S_I is the intensity surface sensitivity \mathcal{S}_I , which describes the signal change at the detection wavelength resulting from the adsorption of a small layer l . We define this quantity as follows:

$$\mathcal{S}_I = \lim_{l \rightarrow 0} \frac{dI/dl|_{\lambda_D}}{I(\lambda_D)} \quad (\text{B17})$$

We expand equation (B17) with n and write:

$$\mathcal{S}_I = \lim_{l \rightarrow 0} \frac{1}{I(\lambda_D)} \cdot \left[\frac{dI}{dn} \cdot \frac{dn}{dl} \right] = S_I \cdot \lim_{l \rightarrow 0} \frac{dn}{dl} \quad (\text{B18})$$

In this expression, the blue part is the quantity S_I . The connection of the effective refractive index n_{eff} to the layer thickness l can be modelled as an exponentially saturating function according to¹⁵:

$$n_{\text{eff}} = n + \Delta n \cdot \left(1 - e^{(-l/d_s)} \right) \quad (\text{B19})$$

Here, d_s is a parameter describing the sensing distance of the particle and n is the medium's refractive index. Using this relationship, we can derive how the refractive index changes for the adsorption of small layers $\left(\frac{dn}{dl} \right)$.

$$\frac{dn}{dl} = \frac{dn_{\text{eff}}}{dl} = \frac{\Delta n}{d_s} \cdot \left(e^{(-l/d_s)} \right) \quad (\text{B20})$$

Inserting equation (B20) into equation (B18) and using $\lim_{l \rightarrow 0} e^{(-l/d_s)} = 1$, we obtain:

$$(B21) \quad \mathfrak{S}_I = S_I \cdot \frac{\Delta n}{d_s}$$

An overview of all definitions is listed in Table B.4.

Table B.4: Summary of definitions and results for plasmon sensitivities.

Name	Definition	Equation
<i>Intensity bulk sensitivity</i>	$S_I = \frac{dI/dn _{\lambda_D}}{I(\lambda_D)}$	$S_I = \frac{8}{n} - \frac{4S_\lambda}{\lambda_{\text{res}}} - \frac{S_\lambda}{\varepsilon_2} \frac{d\varepsilon_2}{d\lambda_{\text{res}}} + \frac{2S_\lambda}{\Gamma}$
<i>Intensity surface sensitivity*</i>	$\mathfrak{S}_I = \lim_{l \rightarrow 0} \frac{dI/dl _{\lambda_D}}{I(\lambda_D)}$	$\mathfrak{S}_I = S_I \cdot \frac{\Delta n}{d_s}$
<i>Resonance wavelength bulk sensitivity</i>	$S_\lambda = \frac{d\lambda_{\text{res}}}{dn}$	$S_\lambda = 2n \left(1 - \frac{1}{L}\right) \cdot \frac{1}{\frac{d\varepsilon_1}{d\lambda_{\text{res}}}}$
<i>Resonance wavelength surface sensitivity</i>	$\mathfrak{S}_\lambda = \lim_{l \rightarrow 0} \frac{d\lambda_{\text{res}}}{dl}$	$\mathfrak{S}_\lambda = S_\lambda \cdot \frac{\Delta n}{d_s}$

*Also known in the literature¹⁷ as FOM*_{layer}.

B.3 Additional Figures

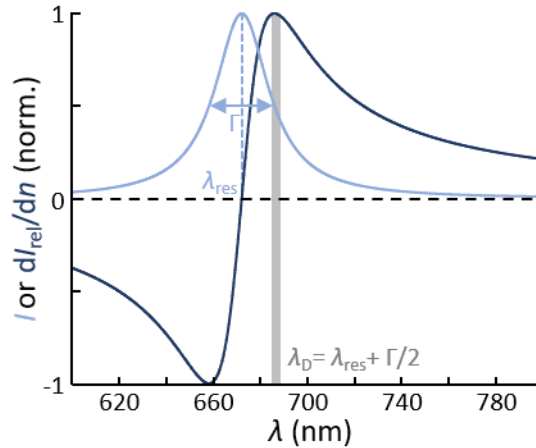


Figure B.5: Optimal detection wavelength λ_D . Representative scattering intensity of a gold nanorod (light blue line) with the corresponding resonance wavelength λ_{res} and linewidth Γ . Relative change in intensity at the detection wavelength λ_D after the ambient refractive index of the gold nanorod has changed (dark blue line). Both functions are normalized to the respective maximum for better comparison.

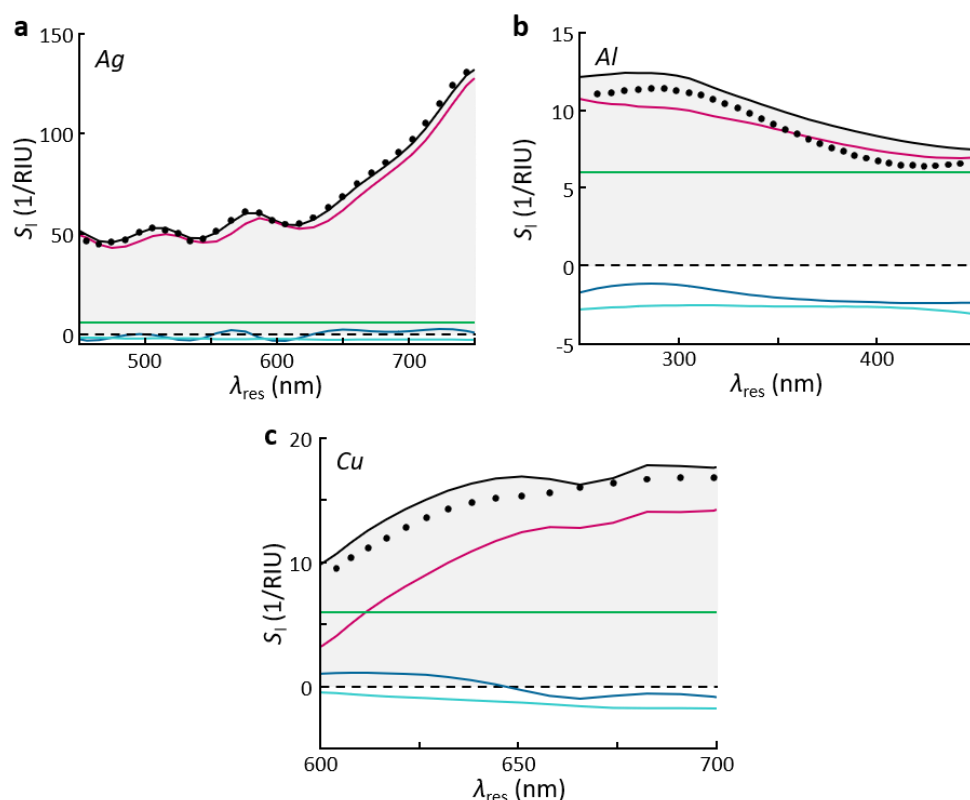


Figure B.6. Intensity bulk sensitivity S_1 for other nanoparticle materials. Theoretically expected behavior of S_1 (black line) and the different compositions of the intensity bulk sensitivity S_1 split to plasmon shift (pink line), dielectric contrast (green line), Rayleigh scattering (cyan line) and frequency-dependent plasmon damping (blue line) as a function of resonance wavelength λ_{res} for **a)** silver using tabulated optical constants reported in Johnson and Christy¹⁰, **b)** aluminum using tabulated optical constants from Palik¹⁵ and, **c)** copper using tabulated optical constants from Palik¹⁵. The black dots depict values of S_1 simulated using QSA.

B.4 Bibliography

1. Nikoobakht, B.; El-Sayed, M. A. Preparation and Growth Mechanism of Gold Nanorods (NRs) Using Seed-Mediated Growth Method. *Chem. of Mater.* **2003**, *15*, 1957-1962.
2. Ye, X.; Zheng, C.; Chen, J.; Gao, Y.; Murray, C. B. Using Binary Surfactant Mixtures To Simultaneously Improve the Dimensional Tunability and Monodispersity in the Seeded Growth of Gold Nanorods. *Nano Lett.* **2013**, *13*, 765-771.
3. Ye, X.; Jin, L.; Caglayan, H.; Chen, J.; Xing, G.; Zheng, C.; Doan-Nguyen, V.; Kang, Y.; Engheta, N.; Kagan, C. R.; Murray, C. B. Improved Size-Tunable Synthesis of Monodisperse Gold Nanorods through the Use of Aromatic Additives. *ACS Nano* **2012**, *6*, 2804-2817.
4. Rosman, C.; Prasad, J.; Neiser, A.; Henkel, A.; Edgar, J.; Sönnichsen, C. Multiplexed Plasmon Sensor for Rapid Label-Free Analyte Detection. *Nano Lett.* **2013**, *13*, 3243-3247.

5. Tian, L.; Chen, E.; Gandra, N.; Abbas, A.; Singamaneni, S. Gold Nanorods as Plasmonic Nanotransducers: Distance-Dependent Refractive Index Sensitivity. *Langmuir* **2012**, *28*, 17435-17442.
6. Kedem, O.; Tesler, A. B.; Vaskevich, A.; Rubinstein, I. Sensitivity and Optimization of Localized Surface Plasmon Resonance Transducers. *ACS Nano* **2011**, *5*, 748-760.
7. Au - Hoang, T. B.; Au - Huang, J.; Au - Mikkelsen, M. H. Colloidal Synthesis of Nanopatch Antennas for Applications in Plasmonics and Nanophotonics. *J. Vis. Exp.* **2016**, *111* (e53876), 1-7.
8. Ye, W.; Celiksoy, S.; Jakab, A.; Khmelinskaia, A.; Heermann, T.; Raso, A.; Wegner, S. V.; Rivas, G.; Schwille, P.; Ahijado-Guzmán, R.; Sönnichsen, C. Plasmonic Nanosensors Reveal a Height Dependence of MinDE Protein Oscillations on Membrane Features. *J. Am. Chem. Soc.* **2018**, *140*, 17901-17906.
9. Gans, R. Über die Form ultramikroskopischer Goldteilchen. *Annalen der Physik* **1912**, *342*, 881-900.
10. Johnson, P. B.; Christy, R. W. Optical Constants of the Noble Metals. *Phys. Rev. B* **1972**, *6*, 4370-4379.
11. Hohenester, U.; Trügler, A. MNPBEM – A Matlab toolbox for the Simulation of Plasmonic Nanoparticles. *Comp. Phys. Comm.* **2012**, *183*, 370-381.
12. Jakab, A.; Rosman, C.; Khalavka, Y.; Becker, J.; Trügler, A.; Hohenester, U.; Sönnichsen, C. Highly Sensitive Plasmonic Silver Nanorods. *ACS Nano* **2011**, *5*, 6880-6885.
13. Foerster, B.; Rutten, J.; Pham, H.; Link, S.; Sönnichsen, C. Particle Plasmons as Dipole Antennas: State Representation of Relative Observables. *J. Phys. Chem. C* **2018**, *122*, 19116-19123.
14. Jung, L. S.; Campbell, C. T.; Chinowsky, T. M.; Mar, M. N.; Yee, S. S. Quantitative Interpretation of the Response of Surface Plasmon Resonance Sensors to Adsorbed Films. *Langmuir* **1998**, *14*, 5636-5648.
15. Palik, E. D. *Handbook of optical constants of solids*. Academic Press: Orlando, 1985.

B.5 Copyright

The manuscript and supporting information of Intensity-Based Single Particle Plasmon Sensing is adapted with permission from Nano Letters.

Nano Lett. **2021**, *21*, 2053-2058. Copyright ©2021 American Chemical Society.



RightsLink®



Intensity-Based Single Particle Plasmon Sensing

Author: Sirin Celiksoy, Weixiang Ye, Karl Wandner, et al

Publication: Nano Letters

Publisher: American Chemical Society

Date: Feb 1, 2021

Copyright © 2021, American Chemical Society

PERMISSION/LICENSE IS GRANTED FOR YOUR ORDER AT NO CHARGE

This type of permission/license, instead of the standard Terms & Conditions, is sent to you because no fee is being charged for your order. Please note the following:

- Permission is granted for your request in both print and electronic formats, and translations.
- If figures and/or tables were requested, they may be adapted or used in part.
- Please print this page for your records and send a copy of it to your publisher/graduate school.
- Appropriate credit for the requested material should be given as follows: "Reprinted (adapted) with permission from (COMPLETE REFERENCE CITATION). Copyright (YEAR) American Chemical Society." Insert appropriate information in place of the capitalized words.
- One-time permission is granted only for the use specified in your request. No additional uses are granted (such as derivative works or other editions). For any other uses, please submit a new request.

[BACK](#)

[CLOSE WINDOW](#)

PLASMONIC NANOSENSORS FOR THE LABEL-FREE IMAGING OF DYNAMIC PROTEIN PATTERNS



C.1 Material and Methods

Materials. DOPC (1,2-dioleoyl-sn-glycero-3-phosphocholine), DOPG (L- α -phosphatidyl-glycerol from *E. coli*), CL (cardiolipin from *E. coli*) and *E. coli* polar extract, were acquired from Avanti Polar Lipids. Buffers, metallic salts, and all the other chemicals were purchased from Sigma-Aldrich or Merck with analytical grade and used without further purification.

Synthesis and characterization of gold nanorods. The gold nanorods used in this work were prepared by a two-step seeded-growth method. The details are described for batch #5 in reference 14 of the main text.

Protein purification. The MinD and MinE proteins were provided by the group of Petra Schwille, overexpressed and purified as described in reference 21 of the main text.

Formation of supported lipid membranes. The appropriate lipid mixture (DOPC/DOPG (70/30) molar ratio, DOPC/DOPG/CL (70/25/5) molar ratio or *E. coli* polar extract was dissolved in chloroform, dried for 15 minutes under a nitrogen stream and kept under vacuum for 2 hours to ensure total solvent removal. By hydrating the dried samples with buffer (50 mM Tris-HCl (pH 7.5), 150 mM KCl), we obtained multilamellar vesicles with a total lipid concentration of 1 mg/mL. We sonicated 250 μ L of this solution at 38°C for 15 minutes to obtain small unilamellar vesicles (SUVs). To induce vesicle fusion,

we added 2 mM CaCl₂ and immediately introduced the solution into the glass flowcell. We incubated the lipid solution at room temperature for 40 minutes to form a continuous supported lipid bilayer. After the incubation, the remaining unfused vesicles were washed first with SLB buffer (50 mM Tris-HCl (pH 7.5), 150 mM KCl) for 15 minutes and then with the Min-buffer (50 mM Tris-HCl (pH 7.5), 200 mM KCl and 5 mM MgCl₂) for another 20 minutes.

Min system reconstitution. To reconstitute the Min wave oscillations on the supported lipid bilayers, we prepared a solution containing 0.75 μM of MinD, 0.75 μM of MinE and 2.5 mM of ATP in Min-buffer. The mixture was added into our flowcell and incubated for 5 minutes before we started recording the nanosensors' scattered light.

Microscope setup. We used a homebuilt dark-field microscope setup recording gray-scale images to determine particle intensities at the illumination wavelength. The setup consisted of an upright optical Zeiss microscope equipped with a Plan-Apochromat 40 x / 1.3 objective, a light-emitting diode (Mounted LEDs, Thorlabs) as light source centered at 735 nm (M735L3), and a scientific CMOS camera (Hamamatsu orca flash V4.0) as detector. The automated data acquisition and data analysis was performed with a self-written software. The setup allowed to record a field of view of 266 μm x 266 μm with up to 10 ms temporal resolution for an indefinite time limited only by memory restrictions.

Calculation of particle Temperature. The equilibrium temperature difference to the surrounding medium of an illuminated spherical particle is given by: $\Delta T = \epsilon_{\text{abs}} \cdot I / 4\pi\kappa r$.¹ In our case, we estimate the absorption cross-section ϵ_{abs} around $3.0 \cdot 10^{-15} \text{ nm}^2$, the illumination intensity $I \approx 2.3 \cdot 10^4 \text{ W/m}^2$, the equivalent radius of a sphere with the same volume as our rods ($V_{\text{rod}} \approx 60000 \text{ nm}^3$) $r \approx 25 \text{ nm}$, and take κ of pure water. These values yield a particle temperature increase of less than 1 mK.

Data processing. To analyze the recorded images, we extracted the intensities of the (several hundred) nanoparticles in the field of view. The resulting time-traces were smoothed and down-sampled to 3 s time-resolution. We used an envelope function interpolating the maxima and minima to remove the slow drift and normalize the amplitude of each time-trace. The process and results are presented in Figure C.1. The oscillation period was computed from an autocorrelation within a one-hour window.

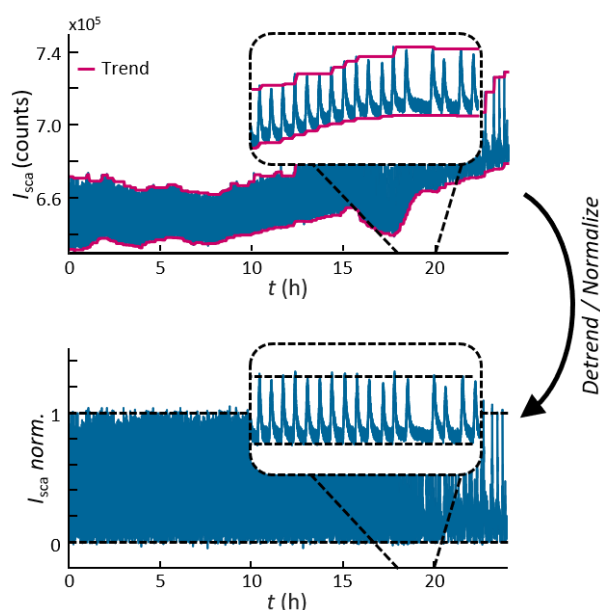


Figure C.1: Baseline correction and normalization. The blue solid line in the upper panel shows the scattering intensity (I_{sca}) of a representative gold nanoparticle as a function of time. To correct for signal drift, we determined the lower and upper envelope (pink solid line, upper panel). Using these boundary envelopes, we normalized the signal, resulting in the data shown in the lower panel. The zoomed-in areas depict the raw (upper panel) and corrected (lower panel) data for two hours.

Sound representation of the data. We generated audio-clips from representative nanoparticle time traces to illustrate the change in frequency of the recorded Min-wave signal by a sound effect. Matlab provides an audiowrite function for that purpose. We choose the standard WAVE auto coding format with a sample rate of 44100 Hz. The audio-clips are named: *MinSound_EColi.mp4*, *MinSound_DOPC_DOPG_CL.mp4* and *MinSound_DOPC_DOPG.mp4* according to the membrane, respectively (see Appendix C.3).

Visualization of the data. We visualized the Min-waves by applying a two-dimensional bilinear interpolation on the individual nanoparticles' time-traces at each time-step. The interpolation function was written by John D'Errico and is available on the MathWorks website.² The resulting images were color-coded with the distinctive Brewer colormap from Charles Roberts.³ Those images were converted to movies using Matlab's video writer in standard audio-video interleave format to the files *MinVideo_EColi.mp4*, *MinVideo_DOPC_DOPG_CL.mp4*, *MinVideo_DOPC_DOPG.mp4*, respectively, with 24 hours compressed to 16 minutes (see Appendix C.3).

The *MinVideo_EColi.mp4* video depicts Min-waves with long-range order. The long-range order vanishes after about 20 hours when the Min-cycle at different locations become increasingly de-synchronized and, at the same time, the oscillation period increases significantly. The video of the DOPC/DOPG/CL membrane shows no regular wave-patterns over the entire 24 hours, whereas in the video of the DOPC/DOPG membrane such waves emerge after about 3 hours.

C.2 Additional Figures

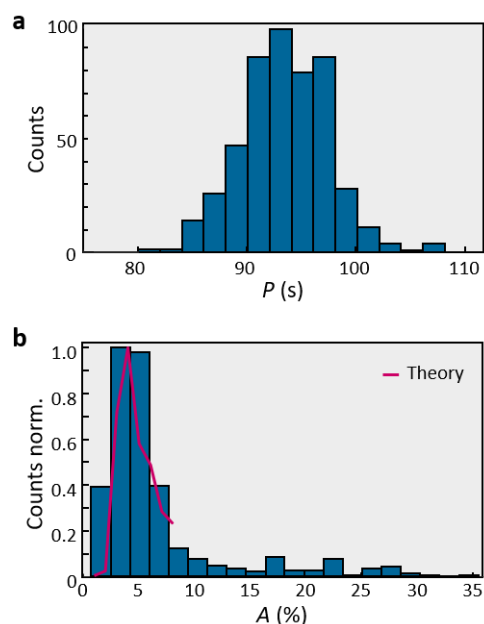


Figure C.2: Oscillation period and signal amplitude of the MinDE coverage fluctuations. Histogram showing the distribution of the period P and relative amplitude A (panel **a** and **b**, respectively) obtained from 487 gold nanoparticles in the experiment presented in Figure 4.3 and Figure 4.4 of the main text. The average period is 93.5 s with a standard deviation of 4.4 s, the average amplitude is 6.6 % with a standard deviation of 5.9 %. The solid red line in panel b depicts the simulated distribution of the oscillation amplitude using the particle size distribution, shown in reference 13, the dimensions of the membrane and Min proteins derived in reference 13, a refractive index of the Min protein layer of 1.40, and the dielectric function of gold from Johnson and Christy⁴. This simulated distribution agrees reasonably well with the measured amplitude distribution. The variation is therefore caused mainly by the variation of the nanoparticles, and not by a variation in Min protein surface coverage at different places.

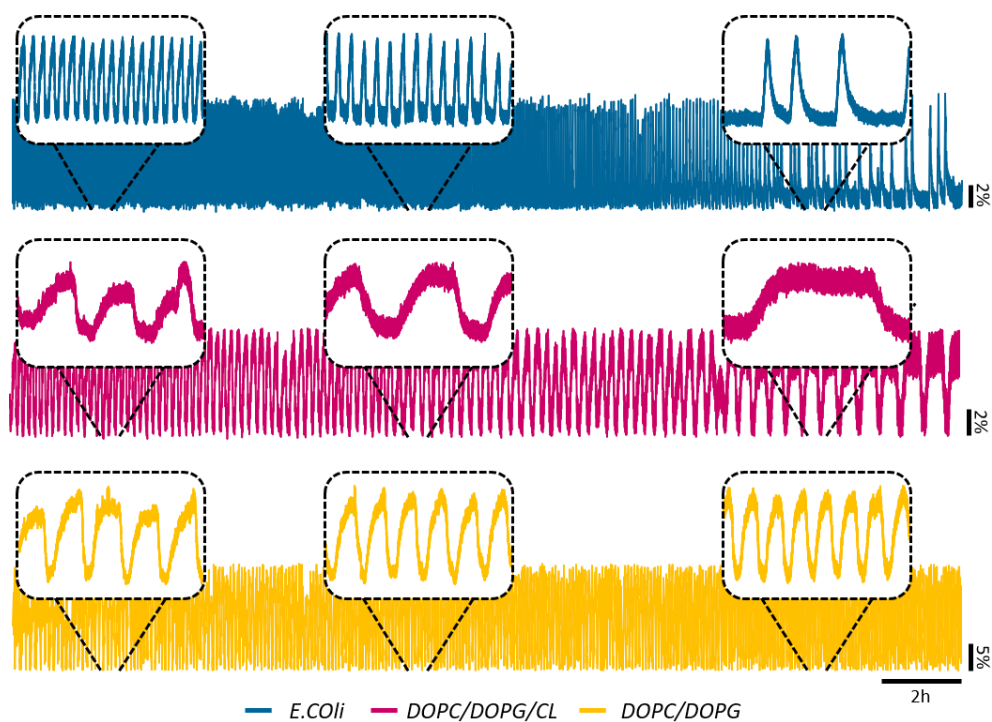


Figure C.3: Example Min coverage fluctuations for different membrane compositions. *E. coli* polar extract (blue solid line), DOPC/DOPG/CL (pink solid line) and DOPC/DOPG (yellow solid line). The insets show the oscillation behavior for 30 min intervals at 2 hours, 10 hours and 20 hours, respectively. For these 24 hours-long experiments we used a time resolution of 30 ms.

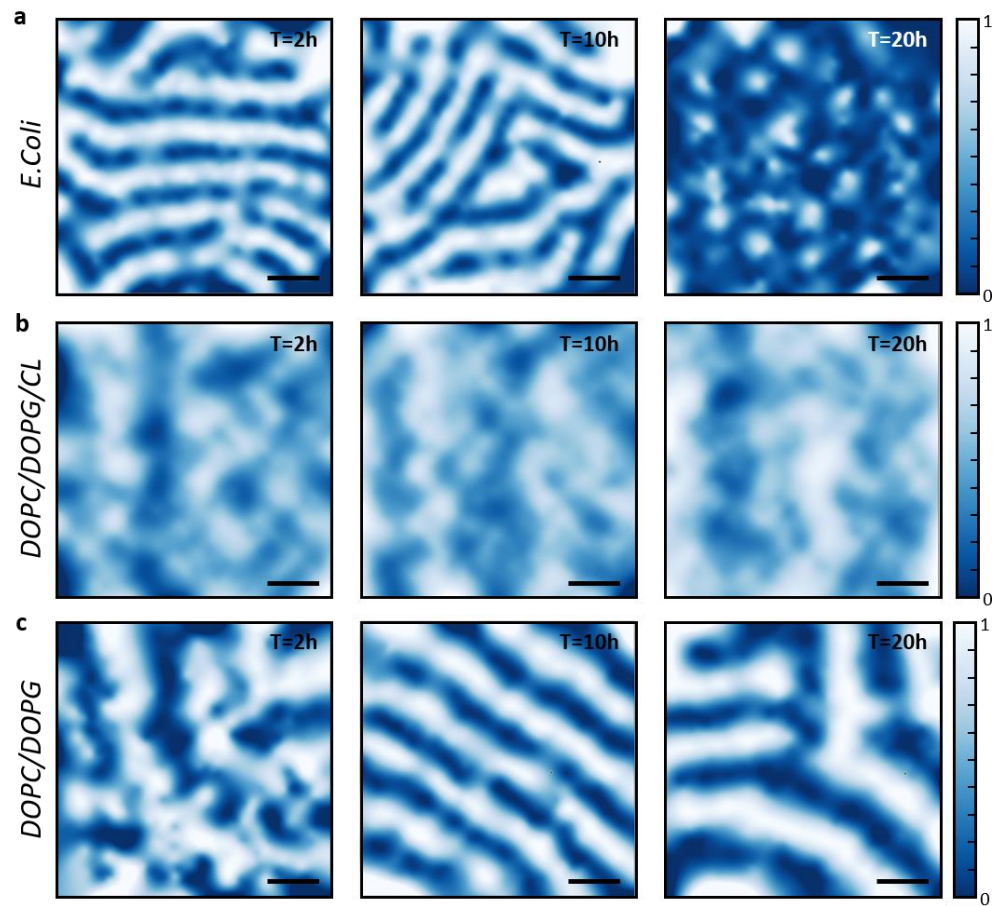


Figure C.4: Snapshots of the spatial patterns for different membrane compositions. Reconstructed images of MinDE coverage fluctuations on top of supported lipid membranes from **a)** *E. coli* polar extract, **b)** DOPC/DOPG/CL and **c)** DOPC/DOPG at the three different time points corresponding to the insets shown in Figure C.3, respectively. The scale bar is 50 μm in all images.

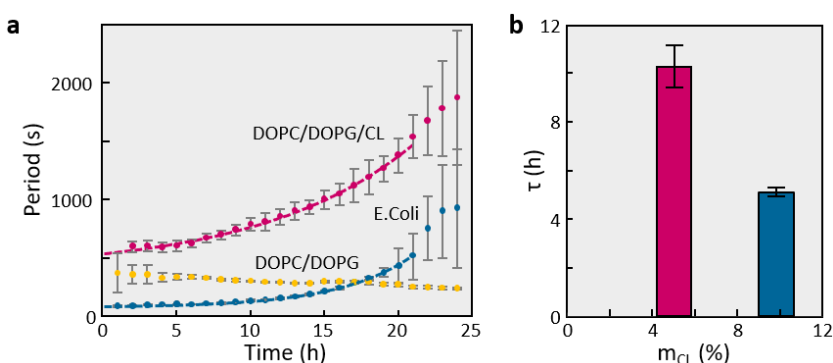


Figure C.5: Evolution of the Min protein oscillation period for different membrane compositions. **a)** The colored data points (pink, yellow and blue) show the average wave period for a time interval of one hour as a function of time. The grey bars indicate the standard deviations among the different nanosensors. A large deviation corresponds to a lack of long-range synchronization. The dotted lines correspond to the best fit of a single exponential function with a time-constant τ . **b)** The time constants τ seem to be inversely related to the amount of CL: 5% of CL resulted in a time-constant around 10 hours and 9.8% of CL to $\tau \approx 4.5$ hours.

C.3 Additional Material

Movies:

- MinVideo_EColi.mp4
- MinVideo_DOPC_DOPG_CL.mp4
- MinVideo_DOPC_DOPG.mp4

Audio Files:

- MinSound_EColi.mp4
- MinSound_DOPC_DOPG_CL.mp4
- MinSound_DOPC_DOPG.mp4

The audio files and movies are available on the internet:

<https://zenodo.org/record/3843305>

C.4 Bibliography

1. Beuwer, M. A.; Prins, M. W. J.; Zijlstra, P. Stochastic Protein Interactions Monitored by Hundreds of Single-Molecule Plasmonic Biosensors. *Nano Lett.* **2015**, *15*, 3507-3511.
2. John D'Errico (2020). Surface Fitting using gridfit (<https://www.mathworks.com/matlabcentral/fileexchange/8998-surface-fitting-using-gridfit>), MATLAB Central File Exchange. Retrieved January 8, 2020.
3. Charles (2020). cbrewer: colorbrewer schemes for Matlab (<https://www.mathworks.com/matlabcentral/fileexchange/34087-cbrewer-colorbrewer-schemes-for-matlab>), MATLAB Central File Exchange. Retrieved January 8, 2020.
4. Johnson, P. B.; Christy, R. W. Optical Constants of the Noble Metals. *Phys. Rev. B.* **1972**, *6*, 4370-4379.

C.5 Copyright

The manuscript and supporting information of Plasmonic Nanosensors for the Label-Free Imaging of Dynamic Protein Patterns is adapted with permission from Journal of Physical Chemistry Letters.

J. Phys. Chem. Lett. **2020**, *11*, 4554–4558. Copyright ©2020 American Chemical Society.



Home

Help

Email Support

Sign in

Create Account

Plasmonic Nanosensors for the Label-Free Imaging of Dynamic Protein Patterns



Author: Sirin Celiksoy, Weixiang Ye, Karl Wandner, et al

Publication: Journal of Physical Chemistry Letters

Publisher: American Chemical Society

Date: Jun 1, 2020

Copyright © 2020, American Chemical Society

PERMISSION/LICENSE IS GRANTED FOR YOUR ORDER AT NO CHARGE

This type of permission/license, instead of the standard Terms & Conditions, is sent to you because no fee is being charged for your order. Please note the following:

- Permission is granted for your request in both print and electronic formats, and translations.
- If figures and/or tables were requested, they may be adapted or used in part.
- Please print this page for your records and send a copy of it to your publisher/graduate school.
- Appropriate credit for the requested material should be given as follows: "Reprinted (adapted) with permission from (COMPLETE REFERENCE CITATION), Copyright (YEAR) American Chemical Society." Insert appropriate information in place of the capitalized words.
- One-time permission is granted only for the use specified in your request. No additional uses are granted (such as derivative works or other editions). For any other uses, please submit a new request.

[BACK](#)

[CLOSE WINDOW](#)

SINGLE OUT-OF-RESONANCE DIELECTRIC NANOPARTICLES AS MOLECULAR SENSORS



D.1 Material and Methods

Materials. Silica nanoparticles of different sizes functionalized with amino groups were purchased from micromod Partikeltechnologie GmbH. DOPC (1,2-dioleoyl-sn-glycero-3-phospho-choline) and DOPG (L- α -phosphatidylglycerol from *E. coli*) were acquired from Avanti Polar Lipids. All the other chemicals were bought from Sigma-Aldrich with analytical grade and used without further purification. The working buffer for the experiments on the Min protein system contained 50 mM Tris-HCl (pH 7.5), 200 mM KCl and 5 mM MgCl₂. The supported lipid membrane (SLB) buffer consists of 50 mM Tris-HCl (pH 7.5) and 150 mM KCl. For all the experiments, we used deionized water from a Millipore system (> 18 M Ω , MilliQ).

Synthesis of gold nanorods. Two batches of gold nanorods were synthesized according to the literature.^{1,2} We used batch number 1 to determine the intensity bulk sensitivity and to measure the intensity surface sensitivity (LbL). The batch number 2 was used to measure the local dynamics of the MinDE protein system and to determine the binding isotherm of the MinD-membrane interaction.

Batch 1: Gold nanorods were synthesized in a two-step process using the method described by Nikoobakht et al.¹ The used amounts of silver nitrate (AgNO₃), seed solution and ascorbic acid (AA) are given in Table D.1.

Batch 2: Gold nanorods were synthesized following the method described in Ye et al.² The amounts of silver nitrate (AgNO_3), seed solution, concentrated chlorohydric acid (HCl) and ascorbic acid (AA) are listed in Table D.1.

Table D.1: Details for gold nanorod synthesis.

Batch	Seeds	AgNO_3	conc. HCl	AA
1	12 μL	50 μL / 4mM	-	70 μL / 79 mM
2	60 μL	350 μL / 4mM	18 μL	25 μL / 64 mM

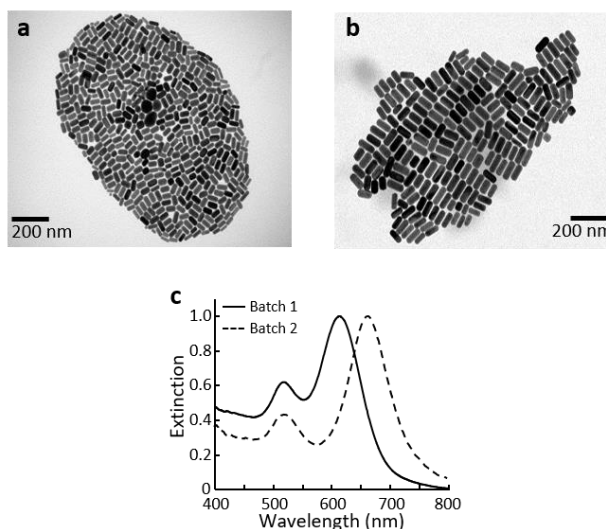


Figure D.1: TEM images and ensemble extinction spectra of gold nanosensors. **a)** TEM image of gold nanorods (batch 1), used as nanosensors for the experiments presented in Figure 5.2 and 5.3 of the main text and Figure D.3. The gold nanorods have an average length of $50.2 \text{ nm} \pm 4.4 \text{ nm}$ and an average width of $25.4 \text{ nm} \pm 4.2 \text{ nm}$. **b)** TEM image of gold nanorods used to record MinDE protein oscillations (see Figure 5.4 of the main text) with an average length of $74.8 \text{ nm} \pm 5.9 \text{ nm}$ and an average width of $33.3 \text{ nm} \pm 2.6 \text{ nm}$. **c)** Normalized ensemble extinction spectra of gold nanosensor batch 1 (solid line) with a resonance wavelength λ_{res} of 613.1 nm and gold nanosensor batch 2 (dashed line) with a resonance wavelength λ_{res} of 665.5 nm

Characterization of gold nanorods and silica nanoparticles. We characterized both gold nanorod batches using transmission electron microscopy (TEM) (FEI Tecnai G2 Spirit Twin microscope) and ensemble extinction spectroscopy (Ocean Optics USB 2000 spectrometer) (Figure D1). From the TEM images, we determined the mean nanoparticle size and standard deviation by evaluating hundreds of gold nanorods. The obtained particles' lengths are $50.2 \text{ nm} \pm 4.4 \text{ nm}$ and $73.3 \text{ nm} \pm 6.3 \text{ nm}$ and diameters are $25.4 \text{ nm} \pm 4.2 \text{ nm}$ and $33.3 \text{ nm} \pm 2.6 \text{ nm}$ for batch 1 and 2, respectively. The error corresponds to the observed size variation, *not* the error of the mean, which is very small in comparison. The polydispersity index (*PDI*), which is a common measure to characterize the molecular weight heterogeneity, is given by³: $PDI = 1 + \frac{s_n^2}{M_n^2}$. The *PDI* of our gold nanorod batches was 1.15 for batch 1 and 1.04 for batch 2. The ensemble extinction spectra results show a mean resonance wavelength of 613 nm for batch 1 and 665 nm for batch 2. We also characterized

Where M_n is the number-average molecular weight and s_n is the standard deviation of M_n .

the silica samples using TEM and ensemble extinction spectroscopy (Figure D2). From the TEM images, we determined the mean nanoparticle size and its variation (measured by the standard deviation) by evaluating hundreds of silica nanospheres. We obtained particle diameters of $118.9 \text{ nm} \pm 11.9 \text{ nm}$ for silica₁₀₀, $209.8 \text{ nm} \pm 29.6 \text{ nm}$ for silica₂₀₀ and $304.9 \text{ nm} \pm 31.8 \text{ nm}$ for silica₃₀₀. The PDI calculation for the three silica nanoparticle batches yields values of 1.09, 1.12 and 1.19, respectively. The ensemble extinction spectra of the silica nanospheres show the λ^{-4} trend as expected for out-of-resonance dielectric nanoparticles (see Figure D2d).

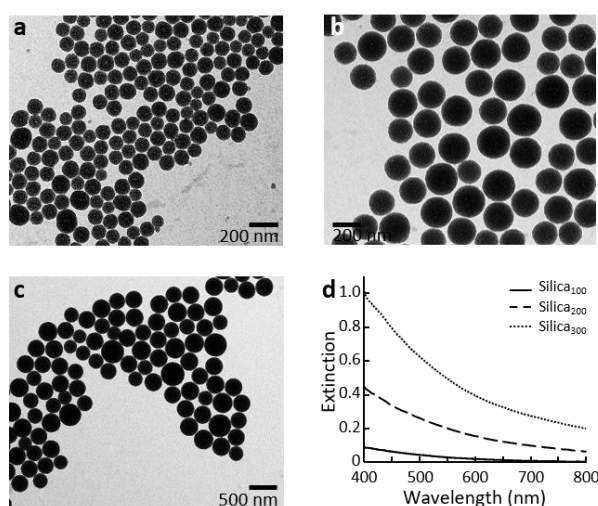


Figure D.2: TEM images and ensemble extinction spectra of silica nanoparticles. TEM images of silica nanoparticles, used for the experiments presented in Figure 5.2 and 5.3 of the main text, Figure D.3 and D.5, with average diameters of **a)** $118.9 \text{ nm} \pm 11.9 \text{ nm}$, **b)** $209.8 \text{ nm} \pm 29.6 \text{ nm}$ and **c)** $304.9 \text{ nm} \pm 31.8 \text{ nm}$. **d)** Ensemble extinction spectra of silica nanoparticles shown in (a) solid line, (b) dashed line and (c) dotted line.

Intensity bulk sensitivity S_I . To compare the intensity bulk sensitivity S_I of plasmonic and dielectric nanoparticles, we measured the response of hundreds of nanoparticles to refractive index changes of their local surrounding. To immobilize the nanoparticles on the surface of a glass substrate, we added a very dilute suspension of nanoparticles to our microfluidic flow cell followed by a solution of sodium chloride (1M). The sodium chloride destabilizes the particles and leads to their adsorption to the flow cell. When this process is done right (fast and in dilute suspensions), the nanoparticles attach to the surface before starting to aggregate with each other. After depositing the nanoparticles, we recorded their relative intensity change for increasing refractive index (here, glucose at different concentrations in water). For small refractive index changes both particle types show a linear response. We extracted from the experiments the mean proportionality factor S_I ($\Delta I_{\text{rel}} = S_I \cdot \Delta n$) for the three dielectric particle batches.

For the gold nanorods, we obtained S_I from the layer experiment below. The change in refractive index in the entire flow cell affects not only the particles but also the overall collection efficiency of the setup (due to refraction at the second water/glass interface). This issue has caused problems when interpreting the

results from bulk refractive index changes only for gold nanorods, not for the much larger and spherical dielectric particles. We think that the high scattering angles of rod-shaped plasmonic objects is the reason for this effect. Therefore, we found it more reliable to use several small layers of coatings (as in the next section) and extrapolate the result for an infinite layer. In principle, such an approach is closer to most relevant applications anyway.

Table D.2: Input values used for theoretical calculations of S_I and \mathcal{S}_I of silica nanoparticles.

	r (nm)	n_p (RIU)	n_m (RIU)
Silica₁₀₀	59.5	1.46	1.34
Silica₂₀₀	104.9	1.46	1.34
Silica₃₀₀	152.4	1.46	1.34

The experimental results are compared to theoretical predictions (Table 5.1, Main Text). We determined the theoretical predictions using equation (D7) for the silica nanoparticles and the plasmon equation (shown in the main text) for the gold nanorods. The input values used are listed in Table D2 and D3.

Table D.3: Input values used for theoretical calculations of S_I and \mathcal{S}_I of gold nanoparticles. The values are determined using the boundary element method (BEM) for the average size of the gold nanorods.

	D (nm)	AR	d_s (nm)	I (nm)	λ_{res} (nm)	S_λ (nm/RIU)	n_m (RIU)	ϵ_2	$\partial\epsilon_2 / \partial\lambda_{res}$ (1/nm)
gold	25.4	2.0	10.3	41.8	619.1	243.5	1.34	1.36	-0.01

Intensity surface sensitivity \mathcal{S}_I . To compare the intensity surface sensitivity S_I of plasmonic and dielectric nanoparticles, we determined the response of hundreds of nanoparticles to layers of adsorbates using the layer-by-layer (*LbL*) assembly method.⁵⁻⁶ After the immobilization of the nanoparticles at the bottom of a microfluidic flow cell, we deposited alternate layers of poly (styrene sulfonate) (PSS, Mw = 75000 g/mol) and poly (allyl amine hydrochloride) (PAH, Mw = 17500 g/mol) and recorded the relative intensity change ΔI_{rel} after each layer. Plasmonic nanoparticles show a linear response to small changes in adsorbate layers ($\Delta I_{rel} = \mathcal{S}_I \cdot \Delta l$), whereas, the signal change of dielectric nanoparticles is not linear. We approximated the data of dielectric nanoparticles with a quadratic function ($\Delta I_{rel} = \mathcal{S}_I \cdot \Delta l^2$). From the best fits, we determined the proportionality factor \mathcal{S}_I for all batches and compared the results to theoretical predictions. (Table 5.1, Main Text). Again, we calculated the theoretical predictions with our mathematical descriptions. For the dielectric nanoparticles we used equation (D11) and for the plasmonic nanoparticles we used the equation shown in the main text. The input values we used are listed in Table D2 and D3.

Note: In our measurements, the gold nanorods are immobilized on a glass surface, which means that only 60% of their sensing volume is available.⁴ We

account for this reduced sensitivity and adjust the experimental data of the gold nanorod batch accordingly. For the much larger and spherical dielectric spheres, this geometric substrate effect is not relevant (see inset of Figure D.3b for a comparison of sizes and geometry).

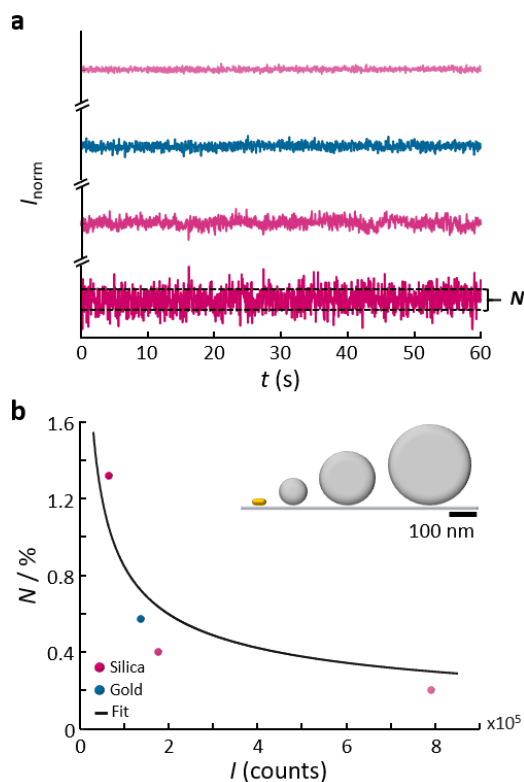


Figure D.3: Noise of silica and gold nanoparticles. **a)** Normalized scattering intensity I_{norm} as a function of time t for a representative 100 nm (dark pink line), a 200 nm (pink line), a 300 nm (bright pink line) silica nanoparticle and a gold nanorod (blue line). From those time traces, we extract the relative standard deviation, which is a measure of the noise level N . **b)** Relative noise N as a function of scattering intensity I . The colored dots show the mean value for the four particle batches used in this work. The black line is the best fit assuming photon statistics for the leading noise source ($N \sim I^{(1/2)}$). The inset depicts the size ratio of the three silica nanoparticles and the gold nanorod.

Noise Level. When comparing the sensor performance, it is important to consider not only the different signal strength but also the relative noise level. Therefore, we determined the relative noise level for all four nanosensor batches we used for the experiments shown in Figure 5.2 of the main text and Figure D.7. We immobilized all four nanoparticle batches on the surface of a microfluidic flow cell and measured an intensity time trace for one minute in water with a time resolution of 50 milliseconds (Figure S1a). For each group of nanoparticles, we determined the mean intensity I and the standard deviation for such a time trace, which defines our noise level N (Figure D.3b).

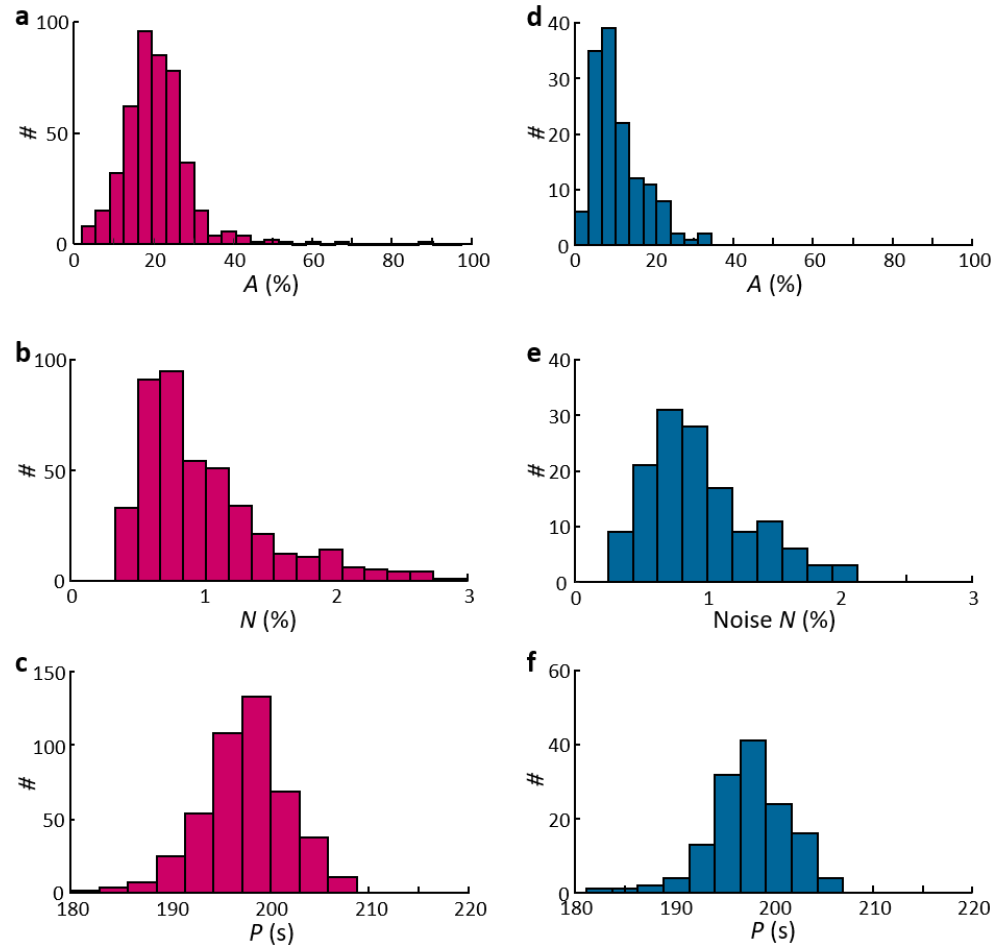


Figure D.4: Signal amplitude, noise and oscillation period for MinDE protein oscillations. We used gold nanorods (in blue) and silica nanoparticles (in pink) as nanosensors to record the protein coverage fluctuations shown in Figure 5.4. Distribution of the **a)** signal amplitude A , **b)** noise N and **c)** oscillation period P for MinDE protein surface coverage fluctuations recorded using 478 dielectric silica nanoparticles. Distribution of the **d)** signal amplitude A , **e)** noise N and **f)** oscillation period P for MinDE protein oscillations obtained from 150 plasmonic gold nanorods.

Local dynamics of the MinDE protein system. To compare the performance of plasmonic and dielectric particles simultaneously, we used the well-known dynamic Min protein system.⁷ We immobilized the gold nanorods and the silica nanoparticles (silica₂₀₀) on the surface of our microfluidic flow-cell with sodium chloride (1 M), spread a lipid membrane (DOPC/DOPG (70/30) molar ratio) according to the literature⁸ and added a solution containing 0.75 μM of MinD, 0.75 μM of MinE and 2.5 mM of ATP. After the incubation time (30 minutes at room temperature (23°C)), we started to record the nanoparticles' response to obtain the typical MinDE oscillations as presented in Figure 5.4a of the main text. From the recorded Min wave oscillations, we obtained the oscillation amplitude A , the period P and the noise level N for all the nanoparticles in the field of view (Figure D.4). The details for the analysis process are described in our previous work.⁸ The MinD and MinE proteins were overexpressed and purified in accordance with literature.⁷

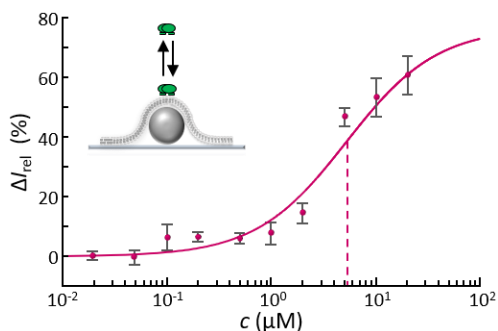


Figure D.5: Binding isotherm for the MinD-membrane interaction obtained by using silica nanoparticles as sensors. The pink dots depict the average response of 137 nanosensors for different MinD concentrations and the error bars the standard error of the mean. The dissociation constant K_D of $5.3 \mu\text{M} \pm 2.0 \mu\text{M}$ (red dashed line) is determined from the best fit of the Langmuir equation (pink solid line) to the experimental data.

Binding isotherm of the MinD-membrane interaction. We quantified the binding affinity (K_D) between the MinD protein and the supported lipid membrane (DOPC/DOPG (70/30) molar ratio) by using the dielectric silica nanoparticles (silica₂₀₀) as sensors. After the particle and membrane deposition (cf. section above), we titrated the MinD protein at different concentrations in the presence of 2.5 mM ATP and recorded the signal change after each concentration (Figure D.5). We extracted the K_D value from the best fit of the Langmuir equation to the experimental data.

Microscope setup. All experiments were performed by using a homebuilt dark-field microscope setup with a narrowband illumination. The setup is composed of a conventional Zeiss microscope equipped with a Plan-Apochromat 40 x / 1.3 objective, light emitting diodes (Mounted LEDs, Thorlabs) with wavelengths centered at 660 nm (M660L3) and 735 nm (M735L3) as light sources and a scientific CMOS camera (Hamamatsu orca flash V4.0) as detector. We used a self-written MATLAB-based software for the automated data acquisition and data analysis. The setup configuration allows us to record the complete field of view (266 μm x 266 μm) simultaneously with high temporal resolution.

D.2 Supplementary Text

Derivation of intensity bulk sensitivity S_I for dielectric nanoparticles. To explain our experimental results quantitatively, we derived a mathematical model to describe the relative intensity change at the detection wavelength λ_D of nanoparticles to local refractive index changes based on electrostatics. We define this measure as the (relative) *intensity bulk sensitivity* S_I :

$$S_I = \frac{dI/dn|_{\lambda_D}}{I(\lambda_D)} \quad (\text{D1})$$

For spherical nanoparticles with diameters much smaller than the wavelength of light, the polarizability a is given by the Clausius-Mossotti equation:

$$(D2) \quad \alpha = 3V\varepsilon_0 \frac{n_p^2 - n^2}{n_p^2 + 2n^2}$$

Here, n_p is the particle's refractive index, n is the refractive index of the surrounding medium, ε_0 is the vacuum permittivity and V is the nanoparticle's volume. The corresponding scattering cross section C_{sca} of small particles is known from literature⁹ as:

$$(D3) \quad C_{\text{sca}} = \frac{\kappa^4}{6\pi\varepsilon_0^2} |\alpha|^2$$

In equation (S3), κ is the wave vector in medium ($\kappa = 2\pi n/\lambda$). Since, the scattering intensity I of nanoparticles is proportional to their scattering cross section ($I \sim C_{\text{sca}}$), we can use this expression to derive our mathematical model. Inserting equation (D2) in equation (D3) we obtain:

$$(D4) \quad \begin{aligned} C_{\text{sca}} &= \frac{(2\pi n)^4}{6\pi\varepsilon_0^2 \cdot \lambda^4} \left| 3V\varepsilon_0 \frac{n_p^2 - n^2}{n_p^2 + 2n^2} \right|^2 \\ &= \frac{24\pi^3 V^2}{\lambda^4} \cdot n^4 \left(\frac{n_p^2 - n^2}{n_p^2 + 2n^2} \right)^2 \end{aligned}$$

When the surrounding medium changes by Δn , the scattering cross section changes by ΔC_{sca} . If we now derive equation (D4) with respect to n and apply the necessary derivation rules, we get equation (D5) as follows:

$$\begin{aligned} \frac{dC_{\text{sca}}}{dn} &= \frac{24\pi^3 V^2}{\lambda^4} \cdot \frac{d}{dn} \left[\frac{n^4 (n_p^2 - n^2)^2}{(n_p^2 + 2n^2)^2} \right] \\ &= \frac{24\pi^3 V^2}{\lambda^4} \cdot \frac{\left(\frac{d}{dn} [n^4 (n_p^2 - n^2)^2] \cdot (n_p^2 + 2n^2)^2 \right) - \left(n^4 (n_p^2 - n^2)^2 \cdot \frac{d}{dn} [(n_p^2 + 2n^2)^2] \right)}{(n_p^2 + 2n^2)^4} \\ &= \frac{24\pi^3 V^2}{\lambda^4} \cdot \frac{\left(\left(\frac{d}{dn} [n^4] \cdot (n_p^2 - n^2)^2 + n^4 \cdot \frac{d}{dn} [(n_p^2 - n^2)^2] \right) \cdot (n_p^2 + 2n^2)^2 \right) - \left(n^4 (n_p^2 - n^2)^2 \cdot \frac{d}{dn} [(n_p^2 + 2n^2)^2] \right)}{(n_p^2 + 2n^2)^4} \\ &= \frac{24\pi^3 V^2}{\lambda^4} \cdot \frac{\left(\left(4n^3 \cdot (n_p^2 - n^2)^2 + 4n^5 \cdot (n_p^2 - n^2) \right) \cdot (n_p^2 + 2n^2)^2 \right) - \left(8n^5 (n_p^2 - n^2)^2 \cdot (n_p^2 + 2n^2) \right)}{(n_p^2 + 2n^2)^4} \\ &= \frac{24\pi^3 V^2}{\lambda^4} \cdot \frac{(4n^3 n_p^6 - 4n^5 n_p^4 - 16n^7 n_p^2 + 16n^9) - (8n^5 n_p^4 - 16n^7 n_p^2 + 8n^9)}{(n_p^2 + 2n^2)^3} \\ &= \frac{24\pi^3 V^2}{\lambda^4} \cdot \frac{(4n^3 n_p^6 - 12n^5 n_p^4 + 8n^9)}{(n_p^2 + 2n^2)^3} \end{aligned}$$

$$= \frac{24\pi^3 V^2}{\lambda^4} \cdot 4n^3 \frac{(n_p^6 - 3n^2 n_p^4 + 2n^6)}{(n_p^2 + 2n^2)^3} \quad (\text{D5})$$

Normalizing equation (D5) with equation (D4) the intensity bulk sensitivity S_I is given by:

$$\begin{aligned} S_I &= \frac{dI/dn|_{\lambda_D}}{I(\lambda_D)} = \frac{dC_{sca}/dn|_{\lambda_D}}{C_{sca}(\lambda_D)} \\ &= \frac{\frac{24\pi^3 V^2}{\lambda^4} \cdot 4n^3 \frac{(n_p^6 - 3n^2 n_p^4 + 2n^6)}{(n_p^2 + 2n^2)^3}}{\frac{24\pi^3 V^2}{\lambda^4} \cdot n^4 \left(\frac{n_p^2 - n^2}{n_p^2 + 2n^2} \right)^2} \\ &= \frac{4(n_p^6 - 3n^2 n_p^4 + 2n^6)}{n(n_p^2 + 2n^2)(n_p^2 - n^2)^2} \\ &= 4 \cdot \frac{(-n_p^4 + 2n^2 n_p^2 + 2n^4)(n^2 - n_p^2)}{n(n_p^2 + 2n^2)(n^2 - n_p^2)^2} \\ &= 4 \cdot \frac{n_p^2(n^2 - n_p^2) + n^2(n_p^2 + 2n^2)}{n(n_p^2 + 2n^2)(n^2 - n_p^2)} \\ &= 4 \cdot \left(\frac{n_p^2(n^2 - n_p^2)}{n(n_p^2 + 2n^2)(n^2 - n_p^2)} + \frac{n^2(n_p^2 + 2n^2)}{n(n_p^2 + 2n^2)(n^2 - n_p^2)} \right) \\ &= 4 \cdot \left(\frac{n_p^2}{n_p^2 n + 2n^3} + \frac{n}{(n^2 - n_p^2)} \right) \\ &= \frac{4n_p^2}{n_p^2 n + 2n^2} + \frac{2}{n + n_p} + \frac{2}{n - n_p} \end{aligned} \quad (\text{D6})$$

Note: There is a singularity point if the refractive index of the medium matches the particle's refractive index ($n = n_p$). Since, the first (in green) and the second (in magenta) term of equation (D6) are much smaller in comparison to the third (in blue) term (Figure D6a), we simplify the intensity bulk sensitivity S_I to:

$$S_I = \frac{2}{n - n_p} \quad (\text{D7})$$

To verify the mathematical description for the intensity bulk sensitivity S_I , we simulated the scattering cross section at a fixed wavelength (here, $\lambda_D = 660$ nm) for silica nanoparticles with 10 nm diameter in different refractive index media (from $n = 1.3$ RIU to $n = 1.6$ RIU). These simulations were calculated using the Clausius Mossotti equation¹⁰ within the quasi-static approximation (QSA) for spherical particles. We used tabulated values for the optical constant of silica.¹¹ We determined the relative response and compared the results to values

calculated using equation (D7). The comparison is presented in Figure D6a. Theoretical calculations (solid line) and simulated data (dots) agree reasonably well.

Derivation of intensity surface sensitivity \mathcal{S}_I for dielectric nanoparticles.

To describe the change of the scattering intensity ΔI at a given wavelength λ_D induced by an adsorbate layer for dielectric nanoparticles, we define a quantity ‘*intensity surface sensitivity* \mathcal{S}_I ’ (‘S with cedilla, pronounced *sb* as in shoe) that is proportional to our signal change in the following way:

$$(D8) \quad \mathcal{S}_I = \lim_{l \rightarrow 0} \frac{dI/dl|_{\lambda_D}}{I(\lambda_D)}$$

Using equation (D2) and (D3) and substituting the particle’s volume V ($V = (4/3)\pi r^3$ for spherical shaped nanoparticles), we obtain for the scattering cross section C_{sca} equation (D9).

$$(D9) \quad C_{sca}(l) = \frac{128\pi^5}{3\lambda^4} \cdot n^4 \cdot \left| \frac{n_p^2 - n^2}{n_p^2 + 2n^2} \right|^2 \cdot (r + l)^6$$

Changing the layer thickness by Δl , changes the scattering cross section by ΔC_{sca} as follows:

$$(D10) \quad \frac{dC_{sca}}{dl} = \frac{128\pi^5}{3\lambda^4} \cdot n^4 \cdot \left| \frac{n_p^2 - n^2}{n_p^2 + 2n^2} \right|^2 \cdot 6 \cdot (r + l)^5$$

Inserting equation (D9) and (D10) into our expression for \mathcal{S}_I , we obtain the intensity surface sensitivity \mathcal{S}_I as:

$$(D11) \quad \begin{aligned} \mathcal{S}_I &= \lim_{l \rightarrow 0} \frac{dI/dl|_{\lambda_D}}{I(\lambda_D)} = \lim_{l \rightarrow 0} \frac{dC_{sca}/dl|_{\lambda_D}}{C_{sca}(\lambda_D)} \\ &= \lim_{l \rightarrow 0} \frac{\frac{128\pi^5}{3\lambda^4} n^4 \cdot \left| \frac{n_p^2 - n^2}{n_p^2 + 2n^2} \right|^2 \cdot 6 \cdot (r+l)^5}{C_{sca}(l) = \frac{128\pi^5}{3\lambda^4} n^4 \cdot \left| \frac{n_p^2 - n^2}{n_p^2 + 2n^2} \right|^2 \cdot (r+l)^6} \\ &= \lim_{l \rightarrow 0} \frac{6 \cdot (r+l)^5}{(r+l)^6} = \frac{6}{r} \end{aligned}$$

To verify the mathematical description for the *intensity surface sensitivity* \mathcal{S}_I , we again simulated the scattering cross section at a fixed wavelength (here, $\lambda_D = 660$ nm) for silica nanoparticles with different diameters (from $r = 5$ nm to $r = 100$ nm) and for a small adsorbate layer with a thickness of $\Delta l = 0.1$ nm and a refractive index of $n_{layer} = 1.45$. From the simulations we determined the relative response induced by the adsorbate layer and compared the results to theoretical calculations using equation (D11). The results are presented in Figure D.6b. Theoretical calculations (solid line) and simulated data (dots) agree reasonably well.

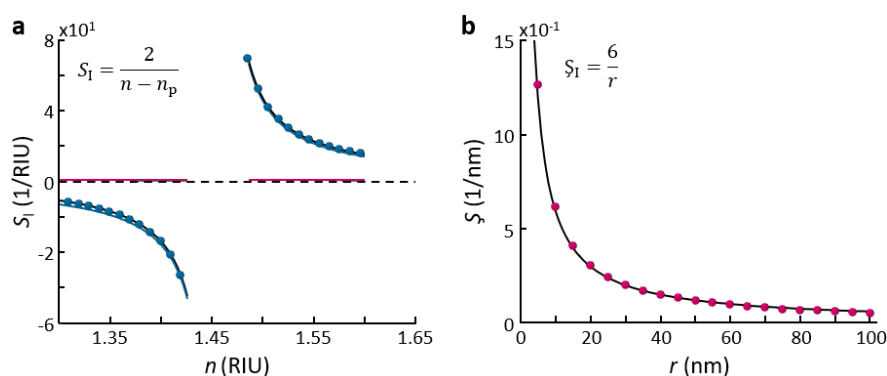


Figure D.6: Mathematical model for the intensity bulk sensitivity S_I and the intensity surface sensitivity S_I . **a)** Different contributions of S_I (black line), namely: Term1 (green line), Term2 (pink line) and Term3 (blue line) as a function of mediums' refractive index n . The inset shows the total equation of S_I . The data points (blue dots) are values of S_I simulated using the quasi-static approximation (QSA). **b)** Intensity surface sensitivity S_I as a function of radius r calculated with the mathematical description (black line) and simulated data using QSA (pink dots).

D.3 Additional Figures

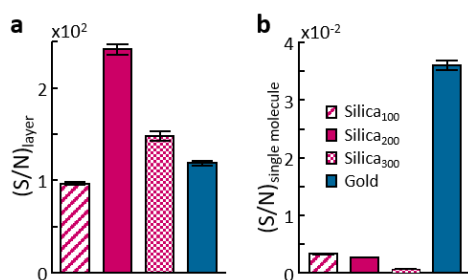


Figure D.7: Signal-to-Noise Ratio 5 nm adsorption layer. **a)** Comparison of signal-to-noise ratios $(S/N)_{\text{layer}}$ for the adsorption of a 5nm layer on gold nanorods (blue) and silica nanoparticles (pink) (legend in panel (b)). **b)** The signal-to-noise ratio for single molecules $(S/N)_{\text{single molecule}}$, calculated by normalizing $(S/N)_{\text{layer}}$ to the sensor's surface area.

D.4 Bibliography

1. Nikoobakht, B.; El-Sayed, M. A. Preparation and Growth Mechanism of Gold Nanorods (NRs) Using Seed-Mediated Growth Method. *Chemistry of Materials* **2003**, *15*, 1957-1962.
2. Ye, X.; Zheng, C.; Chen, J.; Gao, Y.; Murray, C. B. Using Binary Surfactant Mixtures To Simultaneously Improve the Dimensional Tunability and Monodispersity in the Seeded Growth of Gold Nanorods. *Nano Letters* **2013**, *13*, 765-771.
3. Rane, S. S.; Choi, P., Polydispersity Index: How Accurately Does It Measure the Breadth of the Molecular Weight Distribution? *Chemistry of Materials* **2005**, *17*, 926-926.
4. Celiksoy, S.; Ye, W.; Wandner, K.; Kaefer, K.; Sönnichsen, C Intensity-based single particle plasmon sensing. *unpublished*.

5. Kedem, O.; Tesler, A. B.; Vaskevich, A.; Rubinstein, I. Sensitivity and Optimization of Localized Surface Plasmon Resonance Transducers. *ACS Nano* **2011**, *5*, 748-760.
6. Au - Hoang, T. B.; Au - Huang, J.; Au - Mikkelsen, M. H. Colloidal Synthesis of Nanopatch Antennas for Applications in Plasmonics and Nanophotonics. *JoVE* **2016**, (111), e53876.
7. Loose, M.; Fischer-Friedrich, E.; Ries, J.; Kruse, K.; Schwille, P. Spatial Regulators for Bacterial Cell Division Self-Organize into Surface Waves in Vitro. *Science* **2008**, *320*, 789-92.
8. Ye, W.; Celiksoy, S.; Jakab, A.; Khmelinskaia, A.; Heermann, T.; Raso, A.; Wegner, S. V.; Rivas, G.; Schwille, P.; Ahijado-Guzmán, R.; Sönnichsen, C. Plasmonic Nanosensors Reveal a Height Dependence of MinDE Protein Oscillations on Membrane Features. *Journal of the American Chemical Society* **2018**, *140*, 17901-17906.
9. Bohren, C. F. H., Donald R. Absorption and Scattering by a Sphere. *In Absorption and Scattering of Light by Small Particles* **1998**, 82-129.
10. Jackson, J. D., *Classical electrodynamics*. Wiley: New York, 1999.
11. Palik, E. D., *Handbook of optical constants of solids*. Academic Press: Orlando, 1985.
12. Johnson, P. B.; Christy, R. W. Optical Constants of the Noble Metals. *Phys. Rev. B* **1972**, *6*, 4370-4379.

D.5 Copyright

The manuscript and supporting information of Single Out-of-Resonance Dielectric Nanoparticles as Molecular Sensors is adapted with permission from ACS sensors.

Article ASAP (Letter), DOI: 10.1021/acssensors.0c02629. Copyright ©2021 American Chemical Society.



RightsLink®



Home



Help



Email Support



Sign In



Create Account



Single Out-of-Resonance Dielectric Nanoparticles as Molecular Sensors

Author: Sirin Celiksoy, Weixiang Ye, Rubén Ahijado-Guzmán, et al

Publication: ACS Sensors

Publisher: American Chemical Society

Date: Feb 1, 2021

Copyright © 2021, American Chemical Society

PERMISSION/LICENSE IS GRANTED FOR YOUR ORDER AT NO CHARGE

This type of permission/license, instead of the standard Terms & Conditions, is sent to you because no fee is being charged for your order. Please note the following:

- Permission is granted for your request in both print and electronic formats, and translations.
- If figures and/or tables were requested, they may be adapted or used in part.
- Please print this page for your records and send a copy of it to your publisher/graduate school.
- Appropriate credit for the requested material should be given as follows: "Reprinted (adapted) with permission from (COMPLETE REFERENCE CITATION). Copyright (YEAR) American Chemical Society." Insert appropriate information in place of the capitalized words.
- One-time permission is granted only for the use specified in your request. No additional uses are granted (such as derivative works or other editions). For any other uses, please submit a new request.

[BACK](#)

[CLOSE WINDOW](#)

ACKNOWLEDGEMENT

CURRICULUM VITAE

